

**SYNTHESIS OF COATED IRON OXIDE NANOPARTICLES AS AN  
ADDITIVE FOR NITRILE BUTADIENE RUBBER (NBR) FILM**

**ONG HUN TIAR**

**DISSERTATION SUBMITTED IN FULFILMENT  
OF THE REQUIREMENT FOR THE DEGREE OF MASTER OF  
PHILOSOPHY**

**INSTITUTE OF GRADUATE STUDIES**

**UNIVERSITY OF MALAYA**

**KUALA LUMPUR**

**2015**

**UNIVERSITY OF MALAYA**

## ORIGINAL LITERARY WORK DECLARATION

Name of Candidate: ONG HUN TIAR

Registration/Matric No: HGA130012

Name of Degree: Master of Philosophy

Title of Thesis ("this Work"): Synthesis of coated iron oxide nanoparticles as an additive for nitrile butadiene (NBR) film

Field of Study: Nanotechnology (Material Engineering)

I do solemnly and sincerely declare that:

- (1) I am the sole author/writer of this Work;
- (2) This Work is original;
- (3) Any use of any work in which copyright exists was done by way of fair dealing and for permitted purposes and any excerpt or extract from, or reference to or reproduction of any copyright work has been disclosed expressly and sufficiently and the title of the Work and its authorship have been acknowledged in this Work;
- (4) I do not have any actual knowledge nor do I ought reasonably to know that the making of this work constitutes an infringement of any copyright work;
- (5) I hereby assign all and every rights in the copyright to this Work to the University of Malaya ("UM"), who henceforth shall be owner of the copyright in this Work and that any reproduction or use in any form or by any means whatsoever is prohibited without the written consent of UM having been first had and obtained;
- (6) I am fully aware that if in the course of making this Work I have infringed any copyright whether intentionally or otherwise, I may be subject to legal action or any other action as may be determined by UM.

Candidate's Signature

Date:

Subscribed and solemnly declared before,

Witness's Signature

Date:

Name:

Designation:

## ABSTRACT

Food, pharmaceutical processing and healthcare industries are highly concern about industrial hygiene awareness, thus personal protective equipment (PPE) is compulsory to be used in these industries. NBR gloves are one of the most important PPE but they are possible to tear off and contaminate these products during manufacturing and packaging process. High tendency of torn NBR glove remaining in food or products was due to white or light flesh-coloured glove which was not easy to be detected by naked eyes. With such limitation, iron oxide nanoparticles (IONP) were selected as additive for NBR film to improve the detectability by mean of its magnetic properties. However, IONP has a tendency to agglomerate easily, and thus it is hard to obtain a uniform and well dispersed particle IONP in NBR latex matrix. Hence in this project, IONP was synthesized via precipitation method, coated with fatty acid and compounded with NBR latex to produce a detectable NBR films. The properties of IONPs and coated IONPs were investigated by X-ray Diffractometry (XRD), Raman spectroscopy, Fourier Transform Infrared Spectroscopy (FTIR), zeta sizer, Transmission Electron Microscope (TEM), and Vibrating Sample Magnetometer (VSM), Thermal Gravimetric Analyzer (TGA) and sedimentation observation. The properties of C-IONP/NBR film were studied by Universal Testing Machine (UTM), TGA, VSM, FTIR and Scanning Electron Microscopy (SEM). The result shows that, IONP synthesis optimization under reverse precipitation,  $\text{FeSO}_4 \cdot 7\text{H}_2\text{O}$  as precursor, pour-once method and aging time 1.5 hrs was able to produce small particle size, minimal agglomeration and superior magnetization saturation IONP. Furthermore, 0.6 of oleic acid to IONP ratio and 60 mins ultra-sonication time as coated IONP (C-IONP) was dispersed well in NBR latex. Subsequently, it was found out that 5 phr of C-IONP was excellent to incorporate with NBR latex as it improved slightly in tensile property and induced sufficient magnetic detectability to magnetic detector.

## ABSTRAKS

Kebersihan merupakan salah satu faktor penting di dalam industri pemprosesan bahan makanan, farmasi, dan produk penjagaan kesihatan. Oleh itu, pemakaian peralatan perlindungan peribadi (PPE) seperti sarung tangan getah nitrile butadiene (NBR) adalah diwajibkan di dalam industri tersebut. Walaubagaimanapun, terdapat keberangkalian tinggi untuk sarung tangan NBR terkoyak semasa pemprosesan dan pembungkusan seterusnya memberikan kesan pencemaran kepada produk yang dihasilkan. Tambahan pula warna putih sarung tangan NBR menyukarkan pengesanan sepihan kayaknya dilakukan secara manual. Disebabkan oleh permasalahan ini, nanopartikel oksida besi (IONP) telah dipilih sebagai bahan tambahan kepada sarung tangan NBR untuk meningkatkan keberkesanan sifat magnetnya dan sekaligus membolehkan ia mudah untuk dikesan. Walau bagaimanapun, IONP senang tergumpal dan sukar diserakkan dengan seragam dalam matriks NBR. Oleh itu, dalam projek ini, IONP yang telah dihasilkan melalui kaedah pemendakan, disalut dengan asid lemak iaitu asid oleik sebelum dicampurkan dengan NBR untuk penghasilan sarung tangan bermagnet. Sifat-sifat IONP dan penyalut IONP (C-IONP) telah dikaji oleh Sinar-X (XRD), spektroskopi Raman, Fourier Mengubah Inframerah Spektroskopi (FTIR), zeta sizer, Transmisi Elektron Mikroskop (TEM) dan Bergetar Sampel Magnetometer (VSM), Analyzer Gravimetrik Haba (TGA) dan pemerhatian pemendakan. Akhir sekali, sifat-sifat sarung tangan C-IONP/NBR telah dikaji dengan Ujian Mesin Universal (UTM), TGA, VSM, FTIR dan Mengimbas Mikroskop Elektron (SEM). Hasil kajian menunjukkan bahawa IONP melalui keadeah penghasilan pemendakan berbalik,  $\text{FeSO}_4 \cdot 7\text{H}_2\text{O}$  sebagai pelopor, kaedah penuaan sekali dan masa 1.5 jam dapat menghasilkan IONP yang bersaiz partikel nano, kurang penumpuan dan sifat pemagnetan yang tinggi. Tambahan pula, asid oleik dengan 0.6 nisbah asid oleik kepada IONP dan 60 minit masa ultra-sonikasi didapati menghasilkan penyebaran yang baik dalam getah NBR. Selain itu, didapati

bahawa 5 phr C-IONP merupakan bahan tambahan terbaik kerana ia meningkatkan sedikit pada sifat tegangan dan mengenalkan sifat magnet yang mencukupi untuk sarung tangan NBR.

University of Malaya

## ACKNOWLEDGEMENTS

This thesis would not have possible without the efforts and support of people at the nanotechnology and catalysis research centre (NANOCAT) and my surrounding friends.

First of all, I would like to express my deepest gratitude to my supervisors Prof Dr Sharifah Bee Abd Hamid and Dr Nurhidayatullaili Muhd Zulkapli for their source of guidance, assistance and concern throughout my research project. Their wide knowledge and valuable comments have provided a good basis for my project and thesis. Furthermore, I would like to thank to their willingness to spend their valueless time and help in guiding me through the whole project. I deeply express my thanks to them in helping me in editing the contents and wording of this thesis.

Besides that, I would like to express a special thanks to all staffs in NANOCAT, Physic department and chemistry department of UM for their continuous guidance and assistance during my sample preparation and testing. They are Mr. Sapuan, Miss Farah and Mr Amir Shah. Most importantly, I would like to greatly acknowledge my colleagues, Dr Orathai Boondamneon (Dr Ann), Dr Roshasnorlyza Hazan and my dearest friend Tai Mun Foong. I deeply appreciated their precious ideas and support throughout my entire master study.

I gratefully acknowledge Hartalega Sdn Bhd for their financial support that has helped me in this study, and MyMaster scholarship for sponsoring my tuition fee. Finally, I would like to take this opportunity to express my gratitude to my beloved parents through their encouragement and support me to continue studying. Last but not least, I would like to apologize to others whose contribution that I may have overlooked.

## TABLE OF CONTENTS

ORIGINAL LITERARY WORK DECLARATION .....	ii
ABSTRACT .....	iii
ACKNOWLEDGEMENTS .....	vi
TABLE OF CONTENTS .....	vii
LIST OF FIGURES .....	x
LIST OF TABLES .....	xiii
LIST OF ABBREVIATIONS .....	xv
LIST OF SYMBOLS .....	xvii
CHAPTER 1 .....	1
INTRODUCTION .....	1
1.1 Research Background.....	1
1.2 Problem statement.....	4
1.3 Hypothesis.....	5
1.4 Objectives.....	5
1.5 Scope of present work.....	6
1.6 Organization of Thesis .....	6
CHAPTER 2 .....	8
LITERATURE REVIEW.....	8
2.1 Iron Oxide Nanoparticles (IONP) .....	8
2.1.1 Synthesis of IONP .....	8
2.1.1.1 Precipitation .....	8
2.1.1.2 Hydrothermal .....	10
2.1.1.3 Thermal decomposition.....	10
2.1.1.4 Microemulsion .....	11
2.1.2 Properties of IONP .....	12
2.1.2.1 IONP Phases .....	12
2.1.2.2 Magnetism of IONP .....	14
2.1.2.3 Dependence of particle size on magnetization.....	16
2.1.2.4 Limitation of uncoated IONP .....	17
2.2 Coated IONP .....	18
2.2.1 Polymer coated IONP .....	19
2.2.1.1 Polyethylene glycol (PEG).....	19
2.2.1.2 Polyvinyl alcohol (PVA).....	20
2.2.1.2 Chitosan .....	21

2.2.2 Inorganic material coated IONP .....	22
2.2.2.1 Silica (SiO <sub>2</sub> ) .....	22
2.2.2.2 Titanium dioxide (TiO <sub>2</sub> ) .....	23
2.2.3 Limitation of inorganic material and polymer coating.....	23
2.2.4 Fatty acid coated IONP .....	24
2.2.4.1 Unsaturated fatty acid (Oleic acid) .....	24
2.2.4.2 Saturated fatty acid (Palmitic acid, Stearic acid, Myristic acid and Capric acid).....	25
2.3 Polymer composites .....	28
2.3.1 Magnetic polymer composites.....	29
2.3.2 Magnetic rubber composites .....	30
2.3.2.1 Magnetic natural rubber composites .....	30
2.3.2.2 Magnetic synthetic rubber composites.....	31
2.3.3 Nano polymer composites .....	32
2.3.3.1 Nano rubber composites .....	34
CHAPTER 3 .....	36
MATERIALS AND METHODOLOGY .....	36
3.1 Introduction .....	36
3.2 Materials.....	36
3.3 Experimental Method.....	38
3.3.1 Synthesis of IONP .....	38
3.3.2 Synthesis of coated IONP (C-IONP).....	39
3.3.3 Characterization of IONP .....	39
3.3.3.1 X-ray diffraction (XRD) .....	39
3.3.3.2 Zetasizer .....	40
3.3.3.3 High Resolution Transmission Electron Microscope (HRTEM).....	41
3.3.3.4 Vibrating Sample Magnetometer (VSM).....	41
3.3.3.5 Fourier Transform Infrared Spectroscopy (FTIR) .....	42
3.3.3.6 Raman spectroscopy .....	42
3.3.3.7 Thermal Gravimetric Analyzer (TGA) .....	43
3.3.4 Compounding of C-IONP with NBR latex .....	43
3.3.5 Dipping process of NBR film.....	44
3.3.6 Characterization of NBR composite film .....	47
3.3.6.1 Universal Testing Machine (Instron 3345) .....	47
3.3.6.2 Field Emission Scanning Electron Microscopy (FESEM) .....	48
CHAPTER 4 .....	49
RESULTS AND DISCUSSION .....	49



4.1 Synthesis of IONP .....	49
4.1.1 XRD analysis .....	49
4.1.2 Raman spectroscopy analysis .....	53
4.1.3 FTIR analysis .....	57
4.1.4 Zeta sizer analysis .....	59
4.1.5 HRTEM analysis .....	63
4.1.6 VSM analysis .....	70
4.2 Synthesis of coated IONP (C-IONP) .....	74
4.2.1 Particle size and zeta potential analysis .....	74
4.2.2 TGA analysis .....	79
4.2.3 FTIR analysis .....	82
4.2.4 Sedimentation test .....	85
4.2.5 VSM analysis .....	88
4.3 C-IONP/NBR film composite .....	92
4.3.1 Compounding analysis .....	92
4.3.1.1 Composition analysis of NBR/C-IONP compounding (TGA analysis) .....	92
4.3.1.2 NBR/C-IONP interaction analysis (FTIR).....	95
4.3.2 Magnetic properties of NBR/IONP composites .....	96
4.3.2.1 VSM analysis of NBR/C-IONP composites .....	96
4.3.3 Mechanical properties of NBR/C-IONP composites .....	99
4.3.3.1 Tensile properties of NBR/C-IONP composites .....	99
4.3.3.2 Fracture surface analysis of NBR/C-IONP composites .....	101
CHAPTER 5 .....	105
CONCLUSION AND SCOPE OF FUTURE WORK .....	105
5.1 Conclusions .....	105
5.2 Suggestion of future work .....	107
REFERENCES.....	108
List of publications and papers presented .....	121
7.1 Journal publication .....	121
7.1.1 Malaysian Journal of Chemistry.....	121
7.1.2 Journal of Magnetism and Magnetic Materials .....	121
7.1.3 Journal of Composite Science and Technology .....	122
7.2 Paper Presented .....	123
7.2.1 NANO-SciTech 2014 & IC-NET 2014 .....	123
7.2.2 18 <sup>th</sup> MICC 2014.....	124

## LIST OF FIGURES

	<b>Pages</b>
2.1 Crystal structure of (a) hematite and (b) magnetite	13
2.2 Alignment of individual atomic magnetic moments in IONP	14
2.3 Magnetic domains in bulk iron oxide	14
2.4 Hysteresis loop of magnetization curve	15
2.5 TEM micrograph of agglomerated IONP	17
2.6 Proposed scheme of binding between IONP and PEG	19
2.7 Molecular structure of PVA	20
2.8 Schematic diagram of chitosan coated IONP	21
2.9 Silica coated IONP	22
2.10 Layer by layer $\text{TiO}_2/\text{SiO}_2$ coated IONP	23
2.11 Chemical structure of Oleic acid	24
2.12 Stabilization of IONP via the grafted Oleic acid	25
2.13 Chemical structure of Palmitic acid	26
2.14 Chemical structure of Stearic acid	26
2.15 Chemical structure of Capric acid	26
2.16 Chemical structure of Myristic acid	26
2.17 Schematic hydrogen bonding in between NBR and silica	28
2.18 Magnetically induced shape-memory effect of thermoplastic composite	29
3.1 Variables of synthesis method of IONP	37
3.2 Flow chart of compounding process	43
3.3 Former plate of latex film	44
3.4 Flow chart of dipping process	44
3.5 Overall flow chart of IONP synthesis and incorporation into NBR	45

	compound	
3.6	The shape of NBR composite film for tensile test	47
4.1	XRD analysis on IONP via (a) synthesis approach, (b) precursor selection, (c) addition method and (d) aging time	52
4.2	Raman spectra of IONP via (a) synthesis approach, (b) precursor selection, (c) addition method and (d) aging time	55
4.3	Formation path way of magnetite via precipitation method	55
4.4	FTIR spectra of IONP via (a) synthesis approach, (b) precursor selection, (c) addition method and (d) aging time	58
4.5	Hydrodynamic size distribution of IONP for the: (a) Synthesis approach (i) reverse precipitation (ii) normal precipitation (b) Precursor selection (i) $\text{FeSO}_4 \cdot 7\text{H}_2\text{O}$ (ii) $\text{FeCl}_2 \cdot 4\text{H}_2\text{O}$ (c) Addition method (i) pour once (ii) dropwise (d) Aging time (i) 1 hr (ii) 1.25 hrs (iii) 1.5 hrs (iv) 1.75 hrs (v) 2 hrs	62
4.6	HRTEM image of IONP a) Synthesis approach (i) reverse precipitation at $15000\times$ magnification (ii) PSD of reverse precipitation with inset at $120000\times$ magnification (iii) normal precipitation at $15000\times$ magnification (iv) PSD of normal precipitation with inset at $120000\times$ magnification b) Precursor selection (i) $\text{FeSO}_4 \cdot 7\text{H}_2\text{O}$ at $15000\times$ magnification (ii) PSD of $\text{FeSO}_4 \cdot 7\text{H}_2\text{O}$ with inset at $120000\times$ magnification (iii) $\text{FeCl}_2 \cdot 4\text{H}_2\text{O}$ at $15000\times$ magnification (iv) PSD of $\text{FeCl}_2 \cdot 4\text{H}_2\text{O}$ with inset at $120000\times$ magnification c) Addition method (i) pour once at $15000\times$ magnification (ii) PSD of pour once with inset at $120000\times$ magnification (iii) dropwise at $15000\times$ magnification (iv) PSD of drop wise with inset at $120000\times$ magnification d) Aging time (i) 1 hr at $15000\times$ magnification (ii) PSD of 1hr with inset at $120000\times$ magnification (iii) 1.5 hrs at $15000\times$ magnification (iv) PSD of 1.5 hrs with inset at $120000\times$ magnification (v) 2 hrs at $15000\times$ magnification (vi) PSD of 2 hrs with inset at $120000\times$ magnification	68
4.7	Magnetization curve of IONP via (a) synthesis approach, (b) precursor selection, (c) addition method and (d) aging time	72
4.8	Hydrodynamic size distribution of C-IONP for the: (a) Variouscoating agent (i) oleic acid (ii) capric acid (iii) myristic acid (iv) palmitic acid (v) stearic acid (b) Oleic acid loading (i) 0.2 OA (ii) 0.4 OA (iii) 0.6 OA (iv) 0.8 OA (v) 1.0 OA (c) Ultra-sonication time (i) 15 mins (ii) 30 mins (iii) 60 mins (iv) 90 mins (v) 120 mins	77
4.9	Interaction in between oleic acid chain	77

4.10	Interaction between IONP and oleic acid	78
4.11	TGA analysis of C-IONP	81
4.12	Interaction in between saturated fatty acid chain	81
4.13	FTIR spectra of C-IONP	84
4.14	Single and double layer of oleic acid C-IONP	87
4.15	Schematic diagram of single and double layer C-IONP in NBR latex	87
4.16	Magnetization curve of C-IONP	90
4.17	TGA curves of NBR and C-IONP/NBR film composites	93
4.18	FTIR spectra of (a) NBR and (b) NBR 5	95
4.19	Magnetization curves of NBR and C-IONP/NBR composites	97
4.20	(a) Stress-strain behavior of NBR and C-IONP/NBR film composite (b) Tensile strength of different C-IONP loading (c) Elastic modulus of different C-IONP loading (d) Tensile stress at 500 % elongation of different C-IONP loading	99
4.21	FESEM micrographs (a)NBR (b)NBR 5 (c)NBR 10 (d)NBR 15 (e)NBR 20 at (i) 2000× magnification and (ii) 20000× magnification	103
4.22	Salt crosslinking of Zinc oleate with NBR matrix	103

## LIST OF TABLES

	<b>Pages</b>
2.1 Advantages and disadvantages of IONP synthesis methods	11
2.2 Physical and magnetic properties of IONP	12
2.3 Chemical formulation of fatty acids	24
2.4 Nano polymer composite with their properties enhancement	32
2.5 Nano rubber composite with their properties enhancement	34
3.1 Chemical list	37
4.1 Crystallite size and phase composition of IONP with different synthesis parameter	51
4.2 Raman peaks of IONP with different synthesis parameter	54
4.3 FTIR peaks of IONP with different synthesis parameter	57
4.4 Average hydrodynamic size, polydispersity index and zeta potential of IONP	61
4.5 Particle size and shape of IONP with different synthesis parameter	66
4.6 Magnetic properties of IONP with different synthesis parameter	71
4.7 Hydrodynamic size, polydispersity index and zeta potential of C-IONP	75
4.8 Residue, percentage of coating agent and coating agent to IONP ratio of C-IONP	80
4.9 FTIR major peaks assignment of C-IONP	83
4.10 Interaction of carboxylate groups and IONP sites as well as presence of C=O band in C-IONP	83
4.11 Sedimentation test observation on C-IONP in different medium	86
4.12 Magnetic properties of C-IONP	89
4.13 Mass loss, degradation rate and residue of NBR and C-IONP/NBR film composites	93

4.14	Temperature at different mass loss of NBR and C-IONP/NBR film composites	93
4.15	FTIR major peaks assignment of NBR and C-IONP/NBR film composite	94
4.16	Magnetic properties of NBR and C-IONP/NBR composites	96
4.17	Mechanical properties of NBR and C-IONP/NBR film composites	99
4.18	Agglomerated C-IONP in NBR and C-IONP/NBR film composites	101

University of Malaya

## LIST OF ABBREVIATIONS

AA	Acrylic acid
CB	Carbon black
C-IONP	Coated Iron oxide nanoparticles
DI	Deionized water
EMI	Electromagnetic Interference
ENR	Epoxidized natural rubber
FESEM	Field emission scanning electron microscope
FTIR	Fourier transform infrared spectroscopy
HRTEM	High resolution transmission electron microscope
IONP	Iron oxide nanoparticles
MAA	Methacrylic acid
MONPs	Metal oxide nanoparticles
MPS	Mercaptopropyltrimethoxysilane
MRI	Magnetic resonance imaging
NBR	Nitrile butadiene rubber
NR	Natural rubber
OA	Oleic acid
PDI	Polydispersity index
PEI	Poly(ethylene imine)
PEG	Polyethylene glycol
PFCA	Perfluorocarboxylic acid
PFCs	Perfluorinated compounds
PNIPAM	Poly(N-isopropylacryamide)
PPE	Personal protective equipment

PVA	Polyvinyl alcohol
SMP	Shape memory polymers
TEOS	Tetraethyl orthosilicate
TGA	Thermal gravimetric analyser
TPNR	Thermoplastic natural rubber
UTM	Universal testing machine
VSM	Vibrating sample magnetometer
XRD	X-ray Diffractometry
ZDBC	Zinc Dibutyldithiocarbamate



## LIST OF SYMBOLS

emu/g	Electromagnetic unit/gram
Hz	Hertz
G	Gauss
H <sub>c</sub>	Coercivity
kV	Kilo volt
M <sub>r</sub>	Remanance
M <sub>s</sub>	Magnetization saturation
rpm	Rotation per minute
T <sub>c</sub>	Curie temperature
A	Alpha
γ	Gamma
nm	Nanometer
g	Gram

## CHAPTER 1

### INTRODUCTION

#### 1.1 Research Background

The total world rubber glove demand was estimated to be 32.4 billion pieces in year 2014 and total rubber glove used for food processing and handling is approximately 5 - 10 % (Malaysian Rubber Board, 2014). It is equivalent to 1.62 – 3.24 billion pieces a year. These gloves are commonly made by from latex, vinyl, nitrile or polyethylene co-polymer, with vinyl and polyethylene gloves being the cheaper options. Nitrile butadiene rubber (NBR) gloves being outstanding in terms of durability and elasticity, provides comfort and dexterity (Drabek, Boucek, & Buffington, 2013). During the course of manufacturing or packaging, small pieces of the glove may become torn off or separated from the glove and become contaminant to the food and pharmaceutical products. In fact, white or light flesh-coloured glove is non-detectable by naked eyes which can probably increase risks on food contamination. It is a serious issue which it can probably lead to food poisoning in certain extend. Even though precaution has been taken, food contamination will remain unsolved, as visual detection is not reliable. Research on rubber nano-composites can be both fundamental and applied, and has attracted growing attentions to increase the mechanical and detection of the rubber glove. Numerous studies have been carried out since late 1960s, started with the incorporation of barium ferrite particles into NBR and extruded into solid shapes for flexible magnets application (Kroenke, 1969). Then, it initiated the idea of incorporating magnetic properties materials into NBR. For instance, magnetic properties of nitrile butadiene rubber (NBR) were induced by incorporating yttrium, iron and strontium ferrite with NBR (De Ricci & Phalip, 1999). Besides that, another invention of magnetic detectable latex was designed by incorporating chromium oxide with NBR

latex (Lucas et al. 2009). Besides that, superparamagnetic nanoparticles are currently used as contrast agent in magnetic resonance imaging (MRI) (German et al., 2013; Jha et al., 2013). They are originally ferromagnetic substances which have lost their permanent magnetism due to their small size. The magnetization of such nanoparticles follows an external magnetic field without any hysteresis and they are better known as —superparamagnetic due to their large magnetic susceptibility. These nanoparticles consist of a coated iron oxide core (magnetite, maghemite or other insoluble ferrites) characterized by a large magnetic moment in the presence of a static external magnetic field.

Generally, magnetite ( $\text{Fe}_3\text{O}_4$ ), maghemite ( $\gamma\text{-Fe}_2\text{O}_3$ ) and hematite ( $\alpha\text{-Fe}_2\text{O}_3$ ) are three main phase of iron oxides that fall under the category of SPIONs. Hematite is the oldest known of the iron oxides and is widespreadly present in rocks and soils. It is also known as ferric oxide, iron sesquioxide, red ochre, specularite, specular iron ore, kidney ore, or martite. Hematite is blood-red in color if finely divided, and black or grey if coarsely crystalline. It is extremely stable at ambient conditions, and often is the end product of the transformation of other iron oxides. Magnetite is also known as black iron oxide, magnetic iron ore, loadstone, ferrous ferrite, or Hercules stone. It exhibits the strongest magnetism of any transition metal oxide (Cornell & Schwertmann, 2006). Another common iron oxide that can be easily found is goethite ( $\alpha\text{-FeOOH}$ ) in yellow colour. It is the most wide spread iron oxides in natural environments as it is known as the most stable iron oxides at ambient temperature. Furthermore, two other rare iron oxides are lepidocrocite ( $\gamma\text{-FeOOH}$ ) and ferrihydrite ( $\text{Fe}_5\text{HO}_8 \cdot 4\text{H}_2\text{O}$ ).  $\gamma\text{-FeOOH}$  was found in orange colour and it exists in rocks, soils, biota and rust due to oxidation product of  $\text{Fe}^{2+}$ .  $\text{Fe}_5\text{HO}_8 \cdot 4\text{H}_2\text{O}$  on the other hand is reddish-brown which resulted from rapid hydrolysis of  $\text{Fe}^{3+}$  solutions. It was used as precursor of goethite and/ or hematite as its tendency to form them even at ambient temperature.

The precipitation technique is the simplest and most efficient chemical pathway to obtain iron oxide particles. Iron oxides ( $\text{FeOOH}$ ,  $\text{Fe}_3\text{O}_4$  or  $\gamma\text{-Fe}_2\text{O}_3$ ) are usually prepared by addition of alkali to iron salt solutions and continual ageing of the suspensions. The main advantage of the precipitation process is that a large amount of nanoparticles can be synthesized. However, the control of particle size distribution is limited, because only kinetic factors are controlling the growth of the crystal (Mohapatra & Anand, 2010). In the precipitation process, two stages are involved i.e., a short burst of nucleation occurs when the concentration of the species reaches critical super saturation, and then, there is a slow growth of the nuclei by diffusion of the solutes to the surface of the crystal. To produce monodisperse iron oxide nanoparticles, these two stages should be separated; i.e., nucleation should be avoided during the period of growth (Tartaj et al., 2006). A wide variety of factors can be adjusted in the synthesis of iron oxide nanoparticles to control size, magnetic characteristics, or surface properties. The size and shape of the nanoparticles can be tailored with relative success by adjusting pH, ionic strength, temperature, nature of the salts (perchlorates, chlorides, sulfates, and nitrates), or the  $\text{Fe(II)/Fe(III)}$  concentration ratio. A great variety of polymers with hydroxyl, carboxylate, carboxyl, styrene or vinyl alcohol groups have been used in magnetic nanoparticles production. Coating or encapsulation of particles with polymers is the oldest and simplest method of magnetic particles preparation. Other methods include e. g. suspension, dispersion or emulsion polymerization (Utkan et al., 2011). The most common polymers used to stabilize bare magnetic nanoparticles are starch and dextran and its derivatives, polyethylene glycol, alginate, polyvinyl alcohol (PVA), chitosan, polylactide, poly (ethylene imine) (PEI), and dendrimers (García-Jimeno & Estelrich, 2013). Stabilization can be achieved by several approaches, including *in-situ* coatings and post synthesis coatings (Laurent et al., 2008). Nanoparticles are coated

during synthesis for *in-situ* coatings, while post-synthesis coating method consists of grafting the polymer onto the magnetic particles once synthesized.

## 1.2 Problem statement

As discussed, traceability of NBR torn glove is the main issue especially in food processing industry. In order to trace NBR torn glove, the idea of incorporation of IONP into NBR latex was suggested. The idea of using IONP leads to other problems such as optimization of IONP synthesis, incompatibility of IONP with NBR latex and the impact of adding IONP to NBR latex. The drawback of IONP is low magnetization saturation ( $M_s$ ), leading to higher loading of IONP required to incorporate with NBR latex. Consequently, high agglomeration of IONP in NBR latex and high cost of NBR composites as a result from the high loading of IONP needed to produce a metal detectable glove. Therefore,  $M_s$  of IONP must be increased by improving the formation of magnetite, at the same time reduce the phase transformation of magnetite to other phases. To solve this problem, several synthesis parameters can be carried out to achieve high  $M_s$  of IONP. Numerous parameters such as flow rate (Moharir, Gogate, & Rathod, 2012), molar ratio of iron salts (Petcharoen & Sirivat, 2012), concentration and type of base (Mascolo, Pei, & Ring, 2013), and stirring rate (Ibarra-Sánchez, Fuentes-Ramírez, Roca, del Puerto Morales, & Cabrera-Lara, 2013) were studied to increase  $M_s$  to the desired value. Besides, IONP tend to agglomerate due to larger surface area in contact to each other. IONP in solid form is normally unstable and easily attracted to each other because of Van de Waals and magnetic dipolar forces of IONP. Hence, surface modification of IONP or coating agent was introduced to reduce the agglomeration. Several studies have been done to cater to this difficulty by using polymer (Dorniani et al., 2014), inorganic materials (Kokate et al., 2015) and fatty acid (Erler et al., 2013). Moreover, compatibility between NBR latex and IONP is another obstacle that is facing. It is recorded that, none of the previous works motivated and

focused on the incompatibility issues of IONP within the NBR latex. Thus, here the fatty acid coating agent was introduced to improve the compatibility in between IONP and NBR latex with consideration that a better compatibility of composites component could be obtained due to the present of lipophilic and hydrophilic group of fatty acid molecules. Further investigation was carried out in this research to find out the most suitable fatty acid which acts as coating agent for IONP with good compatibility to NBR latex. The coated IONP would be further incorporated into NBR composites with the expectation of better interaction of composites component through the formation of covalent bonds between  $R-NH_2$  (NBR) and  $COOH$  (fatty acid). Indeed, this interaction consequently brought a better dispersion and homogeneity of C-IONP within NBR matrix which consequently increase the magnetic as well as the mechanical properties of the composites system. Therefore, NBR torn glove can be detected by incorporation of C-IONP into it.

### **1.3 Hypothesis**

In this research, NBR torn glove can be detected by incorporation of IONP into NBR latex to form NBR glove composite. The magnetic properties of NBR glove composite can be optimized by manipulating phr of IONP loading amount into NBR latex. The magnetic properties of IONP can be optimized by controlling its phase, size and shape. In order to disperse IONP into NBR latex, oleic acid can be used as surface modification of IONP.

### **1.4 Objectives**

The objectives of this present research work are:

1. To synthesize the Coated Iron Oxide Nanoparticles (C-IONP) as additive to NBR latex.
2. To characterize the magnetic properties of NBR film containing the C-IONP.

### **1.5 Scope of present work**

The aim of the present work is to fabricate and characterize the feasibility of incorporating IONP into NBR latex to induce magnetic properties for IONP/NBR composites. Present work deals with the synthesis of IONP, post-modification of IONP and incorporation of modified IONP with NBR latex. Several researchers have worked on the synthesis of IONP, *in-situ* and post-modification of IONP and incorporation of IONP with NBR (rubber). However, no work has been reported on incorporation of coated IONP which can be compatible well with NBR latex. Therefore, it pioneers the technology of NBR composite in glove manufacturer. The composite fabricated in this work is metal detectable for food processing and pharmaceutical industries which can be detected using metal detection equipment in efforts to inspect for foreign non-food metal objects. It is a new product that is applicable to these industries by improving food hygiene while reducing the cost and waste of food.

### **1.6 Organization of Thesis**

This thesis has been structured into 5 respective chapters.

Chapter 1- Introduction, part started with the brief scenario of research projects followed by the problem associated with production and properties of nitrile butadiene gloves. From that, the ideas of metal detectable and coated metal oxide has been derived which consequently be the main objectives and focused of this research work

Chapter 2- Literature review of various aspects of magnetic nanoparticles (synthesis and properties), coated IONP (polymer, inorganic materials and fatty acid) as well as polymer composite (magnetic polymer, magnetic rubber and nano polymer). Some data on the magnetic and mechanical properties of NBR composites is well reviewed for a comparison to the current project.

Chapter 3- Explains about materials and methodology of synthesis or development of IONP, C-IONP and NBR/IONP composites. The characterization method used to optimize the physical, chemical and morphological properties of all samples is provided.

Chapter 4- Details data analysis on IONPs, C-IONPs and NBR/IONP composites with regards to magnetic and mechanical properties is given in details supported with the related and current reference

Chapter 5- Summarizes the overall conclusions and recommendation for future research proposal of this study.

University of Malaya



## CHAPTER 2

### LITERATURE REVIEW

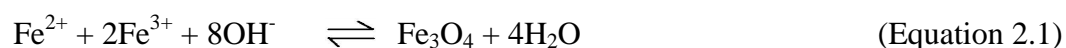
#### 2.1 Iron Oxide Nanoparticles (IONP)

##### 2.1.1 Synthesis of IONP

Nowadays, magnetic properties are important parameter to study the physical properties of materials. Magnetic properties are usually measured by the magnetic strength and direction of magnetism. It is also called magnetic dipole moment. Magnetic dipole moment is generated by electron's spin attributed to electric charge in motion (Abragam & Bleaney, 2012). It can be described in four types of magnetic form which are paramagnetism, diamagnetism, ferromagnetism and anti-ferromagnetism (Kittel & McEuen, 1976). Paramagnetic material consists of unpaired electrons that can spin in any direction. It allows them to attract to magnetic field. Diamagnetic material on the other hand has paired electrons at d orbitals which cause the magnetic field to cancel out and sometimes it is repelled by magnetic field. Pure ferromagnetic material ideally has domain consists of parallel electro spin alignment when magnetic field is exerted. Meanwhile, antiferromagnetic material is inversed to ferromagnetic material. Several synthesis method of Iron oxide nanoparticle (IONP) as one of magnetic nanoparticle has studied such as co-precipitation, hydrothermal reaction, thermal decomposition and microemulsion.

##### 2.1.1.1 Precipitation

This method is the simplest and facile way to synthesis IONP for the mass production because it is involved the co-precipitation of both magnetite ( $\text{Fe}_3\text{O}_4$ ) and maghemite ( $\gamma\text{Fe}_2\text{O}_3$ ).  $\text{Fe}^{2+}$  and  $\text{Fe}^{3+}$  salts prepared in aqueous base solution (Equation 2.1).

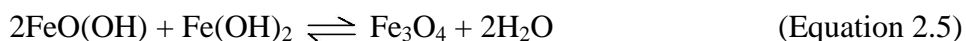


However, there are still disadvantages of this method, including difficulties of controlling mono-phase of magnetite with narrow size distribution, shape and morphology. Several parameters can be varied such as temperature, stirring rate, flow rate, precursor concentration and pH to minimize the size and maximize the magnetic properties of IONP. According to Valenzuela et al. (2009), mean diameter of 10 nm IONP and narrow size distribution were synthesised by  $\text{Fe}^{2+}/\text{Fe}^{3+}$  in aqueous solution (molar ratio 1:2) precipitated by  $\text{NH}_4\text{OH}$  solution at stirring rate of 10,000 rpm. Besides, Karaagac, Kockar, and Tanrisever (2011) reported that 9 nm as well as superparamagnetic of IONP can be synthesised by increasing synthesis temperature from 20 to 80 °C.

The next limitation of this method count on particle size distribution due to the only kinetic factors are influencing the grow rate of crystal. Two stages are occurred during co-precipitation process. In the first stage, nucleation starts to form until the critical supersaturation. Next, slow propagation growth of nuclei is due to solutes slowly diffuse on crystal surface. In order to have low polydispersity index or monodisperse IONP, nucleation in first stage should be separated from second stage of nuclei growth (Tartaj et al, 2006)

However, this limitation can reduce by controlling the stirring rate and base molarity. According to Mahmoudi et al. (2008), the stirring rate in the range of 7200 to 9000 rpm with 1.1 M of base solution would improve the saturation magnetization. Greater percentage of magnetite can obtain by increasing the molarity of base solution. It can be explained Equation 2.2 to 2.5.





In fact, by increasing the molarity of base solution, reaction in Equation (2.2) and (2.4) tends to shift to the right which leading to the final formation of magnetite. Meanwhile, increasing stirring rate did not favour in magnetite formation. Greater stirring rate leads to bubble formation that can oxidize magnetite to other phase.

#### **2.1.1.2 Hydrothermal**

Hydrothermal method usually conducted in reactors or autoclaves with pressure and temperature of 138 MPa and 200 °C, respectively to hydrolyse and dehydrate metal salts. The main parameters that determine the size and magnetic properties of IONP are solvent composition or concentration, temperature and reaction time. These parameters can be adjusted to achieve high nucleation rates while reducing growth rate. Researchers found that by varying the solvent composition reaction or concentration, it contributes to average diameter sizes between 15 to 30 nm as well as single crystals with high purity (Daou et al., 2006; Ge et al., 2009; Mizutani et al., 2008). Besides, high synthesis temperature in presence of coating agent leads to size-controlled monodisperse IONP (S. Sun & Zeng, 2002). At elevated temperature, IONP tends to have high dehydration rates due to reactant diffuse rapidly in water. On the other hand, it found that the reaction time or residence time has higher influence to the average particle size than feed concentration. In this method, by reducing the reaction time can produce monodisperse particles. Hydrothermal can be easily scaling up but cannot produce in situ surface modification IONP as it requires additional post-processing steps.

#### **2.1.1.3 Thermal decomposition**

High thermal decomposition attribute to low polydispersity and size control by using metal-organics as precursor such as  $\text{Fe}(\text{C}_5\text{H}_7\text{O}_2)_3$  and  $\text{Fe}(\text{CO})_5$  by using organic solvents and surfactants. IONP was synthesised by adding  $\text{Fe}(\text{CO})_5$  into solvent (octyl ether) and

surfactant (oleic acid) at 100 °C before heated and refluxed for 2 hours. Small particle size with narrow size distribution 5 to 19 nm IONP obtained in presence of residue oxygen (Woo et al., 2004). Hyeon et al. (2001) reported that highly crystalline and monodisperse maghemite were synthesized by this method. Another research has been conducted with  $\text{Fe}(\text{C}_5\text{H}_7\text{O}_2)_3$  as precursor and solvent (oleylamine) as well as surfactant (oleic acid and 1,2-hexadecanediol). IONP was synthesised by dissolving in mixture of  $\text{C}_6\text{H}_{14}$ ,  $\text{C}_{18}\text{H}_{34}\text{O}_2$  and  $\text{C}_{18}\text{H}_{37}\text{N}$ , then precipitated with ethanol (S. Sun & Zeng, 2002). The use of  $\text{Fe}_3\text{Cl}$  hexahydrate and sodium oleate as precursor to form iron-oleate complex was introduced by Park et al. (2004). Iron-oleate mixed with 1-octadecane heated to 320 °C and continued by 30 mins aging to obtain higher yield of IONP (95 %).

#### **2.1.1.4 Microemulsion**

Microemulsion is the most efficient method to control the size of IONP. In this method, water and oil used as a surfactant to stabilize the interface of synthesized IONP. Water/oil medium provides unique microenvironment; inhibit the growth and narrow size the distribution range of IONP. The average size of IONP is strongly affected by ratio of water to surfactant. Apart from this, concentration of reactants (especially surfactant) and flexibility of surfactant film are playing a vital role to control the particle size. According to Lopez-Quintela (2003), the shape and size of IONP is controlled by curvature free energy, elastic constant and surfactant film curvatures. The elasticity of film is determined by surfactants, thermodynamic conditions and additives. Vidal-Vidal, Rivas, and López-Quintela (2006) proposed oleylamine and it acts as precipitating agent and capping agent to synthesis small size, monodisperse, good crystallization, spherical and high magnetization IONP. Monolayer shell IONP is easier to be synthesised by this method. Zhi et al. (2006) on the other hand suggested in-situ preparation of chitosan coated IONP by microemulsion. The particle size range is between 10 to 80 nm, depending on chitosan molecular weight. It also exhibits stable magnetization as the

IONP after stirring in deionised water has almost the same compare to the original IONP. Liu et al. (2004) found that IONP can be synthesised as small as 10 nm with quasi-sphere shape. They reported that the IONP have perfect superparamagnetism high Curie temperature ( $T_c$ ) value at 587 °C. Table 2.1 summarizes advantages and disadvantages of IONP synthesis methods summary.

Table 2.1: Advantages and disadvantages of IONP synthesis methods

Synthesis methods	Advantages	Disadvantages
Co-precipitation	-Facile and easily to synthesis -High yield and fast synthesis -Synthesis at low temperature	-Easily to oxidised and agglomerated -Difficult to control the particle size
Hydrothermal	-Narrow size distribution and good control -Single crystal and high purity	-Required high temperature and pressure -Long reaction times
Thermal decomposition	-Low polydispersity and size controllable -High yield	-Required high temperature -Water stable suspension is required
Microemulsion	-Easily to control particle size -Able to synthesis monolayer coated IONP	-Low yield and large amount of solvent is needed.

## 2.1.2 Properties of IONP

### 2.1.2.1 IONP Phases

IONP appears in various forms which is giving different type of magnetic properties. Three common types of IONP are magnetite ( $\text{Fe}_3\text{O}_4$  or  $\text{FeO} \cdot \text{Fe}_2\text{O}_3$ ), maghemite ( $\gamma\text{-Fe}_2\text{O}_3$ ) and hematite ( $\alpha\text{-Fe}_2\text{O}_3$ ).  $\text{Fe}_3\text{O}_4$  has the best magnetic properties following by  $\gamma\text{-Fe}_2\text{O}_3$  and  $\alpha\text{-Fe}_2\text{O}_3$  (Lowrie, 1990). Their physical and magnetic properties are illustrated in Table 2.2.

Table 2.2: Physical and magnetic properties of IONP (Teja &amp; Koh, 2009)

Properties	Magnetite	Maghemite	Hematite
Molecular formula	$\text{Fe}_3\text{O}_4$	$\gamma\text{-Fe}_2\text{O}_3$	$\alpha\text{-Fe}_2\text{O}_3$
Density ( $\text{g cm}^{-3}$ )	5.18	4.87	5.26
Melting point ( $^{\circ}\text{C}$ )	1583-1597	-	1350
Hardness	5.5	5	6.5
Type of magnetism	Ferromagnetic	Ferrimagnetic	Weak ferromagnetic or antiferromagnetic
Curie temperature (K)	850	820-986	956
$M_s$ at 300K ( $\text{emu g}^{-1}$ )	92-100	60 - 80	0.3
Standard free energy of formation $\Delta G_f^{\circ}$ ( $\text{kJ mol}^{-1}$ )	-1012.6	-711.1	-742.7
Crystallographic system	Cubic	Cubic or tetrahedral	Rhombohedral, hexagonal
Structural type	Inverse spinel	Defect spinel	Corundum
Space group	Fd3m	$P4_332$ (cubic); $P4_12_12$ (tetragonal)	$R3c$ (hexagonal)
Lattice parameter (nm)	$a = 0.8396$	$a = 0.83474$ (cubic); $a = 0.8347$ ; $c = 2.501$ (tetragonal)	$A = 0.5034$ , $c = 1.375$ (hexagonal) $a_{\text{Rh}} = 0.5427$ , $\alpha = 55.3^{\circ}$ (rhombohedral)

Magnetite exists in black colour meanwhile maghemite is slightly turning to brownish.

Hematite on the other hand exists in red brownish colour. Magnetite exhibits the strongest magnetism with cubic close-packed arrangement. Similarly, maghemite has cubic close-packed arrangement but slightly lower magnetism to magnetite. Conversely, hematite has very weak magnetism with hexagonal close-packed arrangement. Figure 2.1 illustrated crystal structures of magnetite and hematite.

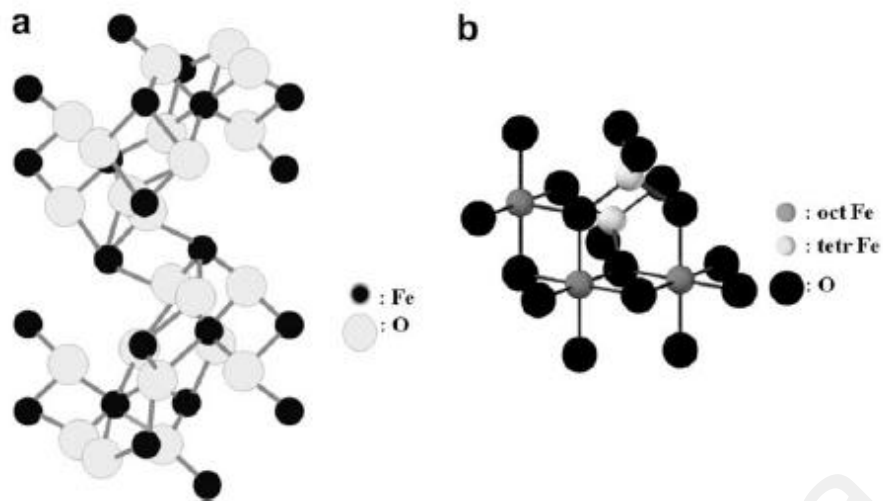


Figure 2.1: Crystal structure of (a) hematite and (b) magnetite (Teja & Koh, 2009)

### 2.1.2.2 Magnetism of IONP

Iron atom has four unpaired electrons in 3d orbitals which contribute to magnetic properties. Different types of magnetic alignment are shown in Figure 2.2. Individual atomic magnetic moments are not aligned orderly in paramagnetic state and they have zero magnetization saturation. Once magnetic field is exerted, some of the atomic magnetic moments will align and obtain magnetization moment. Ferromagnetic IONP has certain magnetization moment as the individual atomic magnetic are align to each other without applying external field. Antiferromagnetic on the contrary obtains no net magnetization moment due to the same magnitude of antiparallel magnetic moments (Adachi & Ino, 1999). Ferrimagnetic has lower net magnetization moment compare to ferromagnetic attribute to different magnitude antiparallel atomic magnetic moments as illustrated in Figure 2.2.

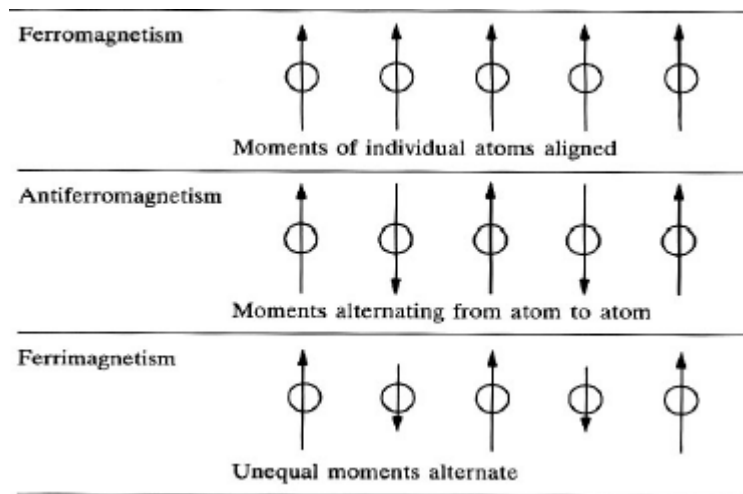


Figure 2.2: Alignment of individual atomic magnetic moments in IONP (Harris, 2002)

Bulk IONP has lower magnetization moment than its value when all atomic magnetic moments are uniformly aligned because it consists of domains. Figure 2.3 shows that different magnetization vector in each domain of bulk iron oxide cancel out partial magnetization moments among each other, resulting in low vector sum magnetization moments.

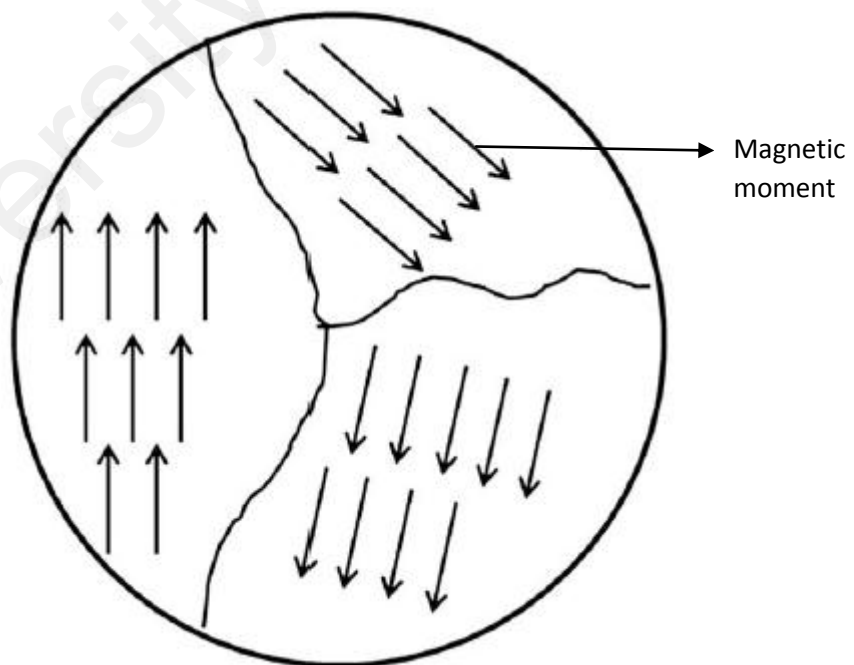


Figure 2.3: Magnetic domains in bulk iron oxide (Teja & Koh, 2009)



Magnetization moment will increase accordingly to external field applied until reaching its saturation. Figure 2.4 illustrates hysteresis loop of magnetization curve where remanance, ( $M_r$ ) and coercive field, ( $H_c$ ) existed. This phenomenon occurred due to domains not returning to their original orientations when applied field is reduced. Having said that, superparamagnetic IONP does not exhibit hysteresis loop and magnetization curve intersects at the zero point (Kechrakos & Trohidou, 1998). IONP of less than 20 nm usually are superparamagnetic. Superparamagnetic magnetites are smaller than 6 nm while superparamagnetic maghemites are smaller than 10 nm at room temperature (Teja & Koh, 2009; W. Zhang et al., 2011).

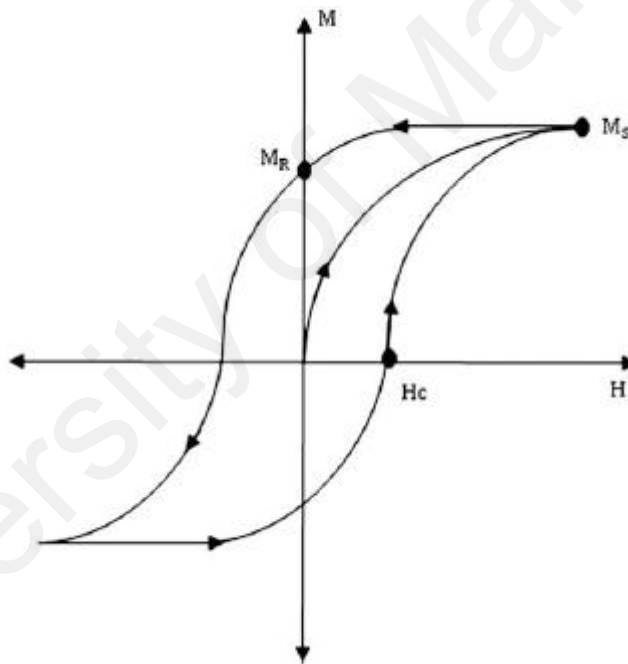


Figure 2.4 Hysteresis loop of magnetization curve (Teja & Koh, 2009)

### 2.1.2.3 Dependence of particle size on magnetization

Particle size of IONP is strongly dependent on parameters in various synthesis methods. These parameters also affected the crystallite size of IONP. In other words, particle size and crystallite size are interrelated to each other. According to Kim et al. (2010), the particle size was increased from 3 to 6 nm whilst crystallite size was increased from 1.3 to 3 nm once precipitating concentration increased. Demortiere et al. (2011) also found

that particle size increased from 2.5 to 14 nm by Transmission Electron Microscope (TEM), and crystallite size increased from 3.1 nm to 12.8 nm by X-Ray Diffractometer (XRD) induced increase in the magnetization saturation at -268 °C from 29 to 77 emug<sup>-1</sup>. B. Wang et al. (2013) reported that particle size 5.5 nm and 6.5 nm of uncoated IONP have 61.9 emug<sup>-1</sup> and 66.6 emug<sup>-1</sup> of magnetization saturation respectively. Slightly different magnetization saturation is attributed to finite size effect and large surface area to volume ratio, crystallization imperfection of IONP, spin canting effect at grain boundary. Final pH value and reaction temperature were investigated in term of its particle size (B. Wang et al., 2013).

#### **2.1.2.4 Limitation of uncoated IONP**

Although uncoated IONP can be synthesised via many methods to control their size, uncoated IONP are facing some obstacles especially agglomeration due to their intrinsic magnetic properties. Consequently, uncoated IONP are usually obtained with bigger particle size as compared to coated IONP. Kazemzadeh et al. (2012) predicted that agglomeration is caused by high surface energy of uncoated IONP and coating on IONP successfully separated nucleation and growth stages. Diethylene glycol coating was added to avoid hydrogen bonding between IONP and water molecule.

Besides uncoated IONP are sensitive to oxidation due to high temperature condition. Magnetite phase are easily changing to maghemite, and further changing to hematite when temperature is increased. Y.-S. Li, Church, and Woodhead (2012) mentioned that magnetite changes to maghemite at 109 °C while maghemite turns to red colour become hematite above 500 °C. In fact, magnetic properties of IONP are decreased with temperature increased. Silica coated IONP on the other hand reduces oxidation as well as agglomeration (Mahmed, 2013).

Apart from the colloidal stability of IONP in water, there is another difficulty because IONP gets sedimented easily after agglomeration. Iso-electric point of IONP is between pH 8.1 to 8.3 (Sun et al., 2006). They tend to form micro-scale aggregation because of weak surface charges. In order to encounter this problem, Polyvinyl alcohol-co-vinyl acetate-co-itaconic acid P(VA-Vac-It) was introduced by Sun et al. (2007). It acted as dispersing agent to form stable IONP colloids in water, and it remained stable in suspension more than 6 months with no significant sedimentation and flocculation.

## 2.2 Coated IONP

Coated IONP has been investigated to avoid problems such as agglomeration, colloidal and oxidation instability faced by uncoated IONP. Agglomeration between IONP is attributed to van der Waals forces and magnetic dipolar forces between two particles. Van der Waals forces result in short range isotropic attraction whilst magnetic dipolar forces induce anisotropic interactions (Figure 2.5). .

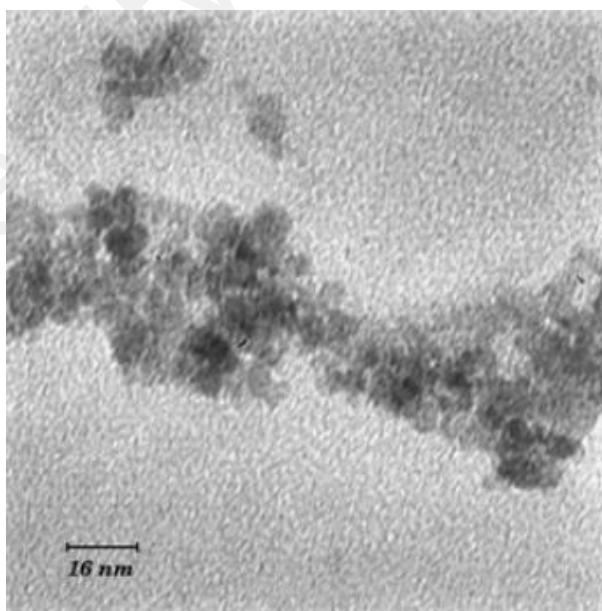


Figure 2.5: TEM micrograph of agglomerated IONP (Eivari & Rahdar, 2013)

Coating agent such as silica, dextran, Polyethylene glycol (PEG) and PVA are good to prevent agglomeration because they balance between attractive force and repulsive

force. Several advantages have been found by improving IONP with coating agent. For example, Hee Kim et al. (2005) synthesized ferrofluids which consist of superparamagnetic IONP and chitosan. Ferrofluids are used as the enhancement of Magnetic Resonance Imaging contrasts. Besides, silica coated IONP has good separation between each particles with an impended oxidation process (Mahmed, 2013; Men et al., 2012). Indeed, silica reduces magnetic dipole force of , and improves colloidal stability. Moreover, dextran can completely prevent inter-particle magnetic interaction by coating on IONP (Sreeja & Joy, 2011). It can be further confirmed by the absence of magnetic hysteresis at room temperature.

## **2.2.1 Polymer coated IONP**

### **2.2.1.1 Polyethylene glycol (PEG)**

PEG is hydrophilic, water soluble and biocompatible polymer which it was widely used to improve biocompatibility of IONP dispersion and blood circulation times. PEG coated on IONP reduces surface charge and extend the circulation time in blood (Ruiz et al., 2013). Hence, it was used in *in vivo* imaging system. PEGs were commercially available at molecular weights from 300 to  $1 \times 10^7$  gmol<sup>-1</sup>. Research on different type of PEG molecular weight coated IONP has been carried out by Barrera et al. (2012). Results showed that graft molecular weight above 1000 gmol<sup>-1</sup> were able to stable in wide range of pH and ionic strength owing to steric repulsion of PEG long chain (Barrera et al., 2012). Subsequently, this research works also report a positive effect on colloidal stability of IONP in water medium. According to Garc ía-Jimeno and Estelrich (2013), IONP coated PEG ferrofluid had extraordinary high physical stability as it maintained the same magnetic and colloidal properties even after more than two years due to the formation of dipole cation binding. Figure 2.6 indicates dipole-cation binding between the ether group of PEG and positive charge of IONP.

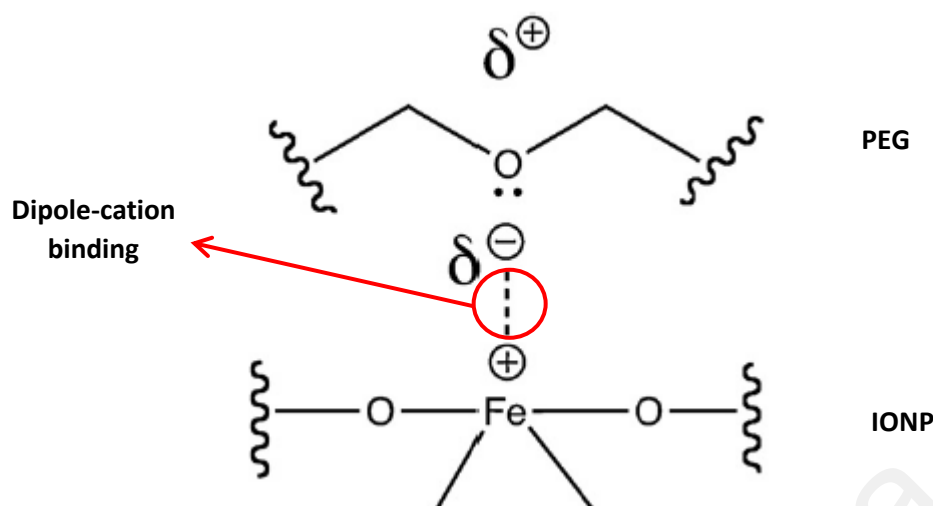


Figure 2.6: Proposed scheme of binding between IONP and PEG (García-Jimeno & Estelrich, 2013)

#### 2.2.1.2 Polyvinyl alcohol (PVA)

PVA was chosen as one of the coating agents for IONP because of its hydrophilicity and biocompatible polymer. PVA was synthesised by hydrolysis of poly(vinyl acetate) (Figure 2.7). PVA was used to cap with  $\text{CoFe}_2\text{O}_4$  in order to improve its stability and cytocompatibility (Salunkhe et al., 2013). Besides, Lee, Isobe, and Senna (1996) managed to synthesis ultrafine PVA coated IONP which has an average size of 4 nm and stable in colloidal dispersion. Furthermore, Xu and Teja (2008) claimed that PVA gave rise to narrow size distribution of IONP and narrow size distributions are obtained with increasing PVA concentration. This is due to the PVA chains that prevent and limit the growth of IONP particle. However size of PVA coated IONP were increased with temperature, residence time and morphology changes in some cases.

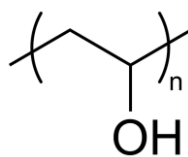


Figure 2.7: Molecular structure of PVA

### 2.2.1.2 Chitosan

Chitosan is the second most common natural polysaccharide after cellulose on earth. It is an alkaline, nontoxic, hydrophilic, biocompatible and biodegradable polymer. Chitosan is produced commercially by deacetylation of chitin, and the degree of deacetylation can be determined by NMR spectroscopy. IONP can be well dispersed in chitosan to make ferrofluid (Hee Kim et al., 2005). Kalkan et al. (2012) synthesized chitosan coated IONP with high magnetic property by reversed phase suspension. Thickness layer of chitosan shell was less than 5 nm and its isoelectric point was found at pH 6.86. The synthesized IONP appeared close to superparamagnetic property with little remanance and coercivity. In advance, chitosan coated octadecyl functionalized IONP was synthesised to extract trace analytes from environmental water (Zhang et al., 2010). Anionic pollutants and perfluorinated compounds (PFCs) are captured by octadecyl group due to large surface area of chitosan coated octadecyl functionalized IONP (Figure 2.8). Positive charged chitosan contributes to PFCs enrichment, and at the same time enhanced dispersibility IONP in aqueous solution.

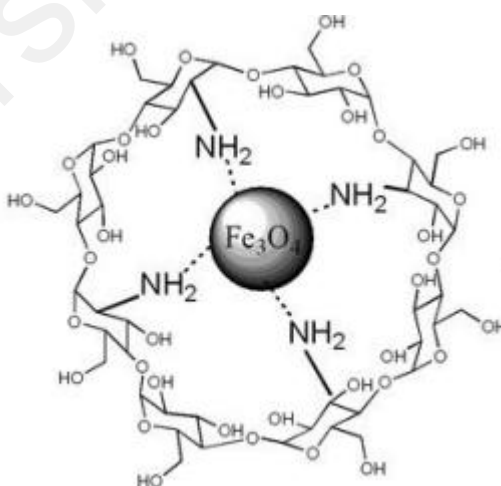


Figure 2.8: Schematic diagram of chitosan coated IONP (Y. Wang, Li, Zhou, & Jia, 2009)

## 2.2.2 Inorganic material coated IONP

### 2.2.2.1 Silica (SiO<sub>2</sub>)

Recently, silica (SiO<sub>2</sub>) is selected as coating material of IONP due to its unique properties. SiO<sub>2</sub> is neutral and it improves coulomb repulsion of IONP. It is not only preventing IONP from aggregation, it provides chemically inert layer for those nanoparticle used in biological system and increase protection from toxicity (Deng et al., 2005). Lien and Wu (2008) prepared Poly(N-isopropylacrylamide) (PNIPAM) grafted SiO<sub>2</sub> coated IONP by microemulsion and free radical polymerization. PNIPAM was a smart polymer attribute to its fast responsive with changing environment such as temperature, pH, ionic strength and magnetic field. However, magnetization saturation of SiO<sub>2</sub> coated IONP was low owing to diamagnetic of silica shells encapsulated IONP (Lien & Wu, 2008). Mahmed (2013) on the other hand suggested oxidation of IONP can be partly prevented by coating amorphous SiO<sub>2</sub>. SiO<sub>2</sub> coated IONP is less oxidized as it has low temperature magnetic measurements and fits Mossbauer spectra. 3-mercaptopropyltrimethoxysilane (MPS) modified SiO<sub>2</sub> coated IONP was Hee Kim et al. (2005) synthesised by molecularly imprinting technique. It was used to trap atrazine on corn and river water samples in order to solve shortcomings of traditional solid phase extraction (Men et al., 2012). Atrazine is one of the herbicides in cereal plants for instance sorghum, corn and sugar-cane. Figure 2.9 shows reaction of IONP and tetraethyl orthosilicate (TEOS) to form SiO<sub>2</sub> coated IONP.

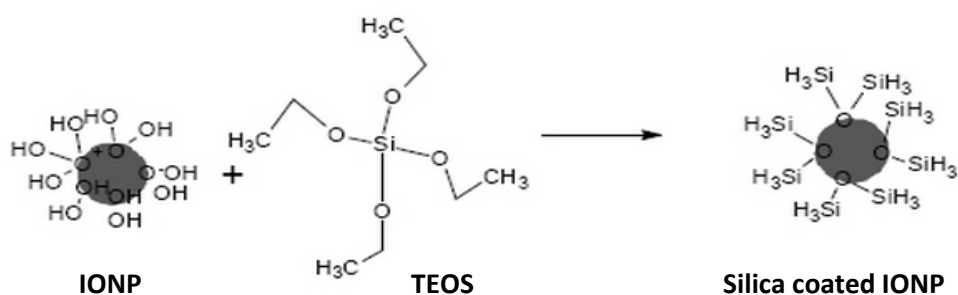


Figure 2.9: Silica coated IONP (Ünak, 2008)

#### 2.2.2.2 Titanium dioxide ( $\text{TiO}_2$ )

Research works have been carried out by incorporating  $\text{TiO}_2$  onto various substrates such as sand, glass beads glass reactor wall, and silica gel (Beydoun et al., 2002). A magnetic photocatalyst which was synthesised by magnetite core and  $\text{TiO}_2$  shell was used as water treatment. Inorganic coating is good in prevention of magnetite core from further oxidation (De Matteis et al., 2012). Hence,  $\text{TiO}_2$  coating may prevent magnetite to further oxidise to maghemite, subsequently reduce the magnetic properties. Beydoun et al. (2002) synthesized stable magnetic photocatalyst by introducing  $\text{SiO}_2$  layer in between  $\text{TiO}_2$  and IONP. This method eliminated photo-dissolution of IONP phase. Besides  $\text{SiO}_2$  interlayer also contribute to a better water stability and relaxivity of the suspension (De Matteis et al., 2014). Having said that,  $\text{SiO}_2$  interlayer layer decreased magnetic properties of IONP and it tended to shield away partial of magnetic strength. Figure 2.10 displays  $\text{TiO}_2$  coated IONP with  $\text{SiO}_2$  interlayer.



Figure 2.10: Layer by layer  $\text{TiO}_2/\text{SiO}_2$  coated IONP (Greene et al., 2014)

#### 2.2.3 Limitation of inorganic material and polymer coating

Inorganic material and polymer coating have successfully enhanced colloidal stability and reduced oxidation rate as well as aggregation of IONP. In fact, it might not be suitable to incorporate with NBR latex. There are two groups in NBR latex which are acrylonitrile group and butadiene group. Typically NBR latex consists less than 35% of acrylonitrile content and it is usually in the range between 20% and 30% (Lipinski &



Tang, 2011). Lower acrylonitrile content NBR latex is prone to increase flexibility of glove at low temperature. During the compounding process of NBR latex, hydrogen bond formed in between acrylonitrile group and polar groups. However, low acrylonitrile content in NBR latex reduces compatibility with polar polymers and inorganic materials. Thus, macromolecule coating agent is introduced to act as intermediate between IONP and NBR latex.

#### 2.2.4 Fatty acid coated IONP

Fatty acid has both hydrophobic and hydrophilic group in which it is suitable to mix with NBR latex. Oleic acid, palmitic acid, stearic acid, capric acid and myristic acid were selected as coating agent in this research and their chemical formula were summarize in Table 2.3.

Table 2.3: Chemical formulation of fatty acids

Fatty acid	Chemical formula
Oleic acid	$\text{CH}_3(\text{CH}_2)_7\text{CH}=\text{CH}(\text{CH}_2)_7\text{COOH}$
Palmitic acid	$\text{CH}_3(\text{CH}_2)_{14}\text{COOH}$
Stearic acid	$\text{CH}_3(\text{CH}_2)_{16}\text{COOH}$
Capric acid	$\text{CH}_3(\text{CH}_2)_8\text{COOH}$
Myristic acid	$\text{CH}_3(\text{CH}_2)_{12}\text{COOH}$

##### 2.2.4.1 Unsaturated fatty acid (Oleic acid)

Oleic acid is an unsaturated fatty acid which is naturally existed in animal and vegetable fats and oils (Figure 2.11). It is commercially available and classified as mono-unsaturated omega-9.

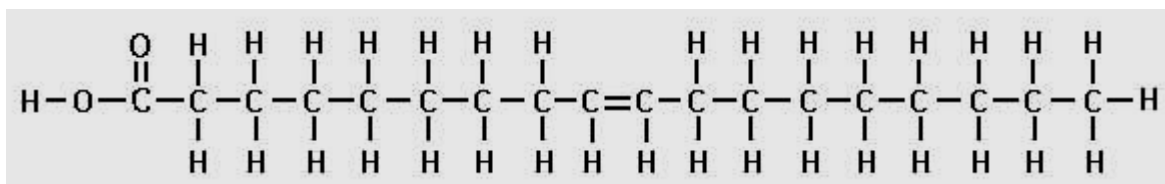


Figure 2.11: Chemical structure of Oleic acid

Due to strong affinity between carboxyl groups of oleic acid and iron cations of IONP, oleic acids are able to attach on IONP with long hydrocarbon chains facing on the other side. Long hydrocarbon chains enhance the stability of IONP as long hydrocarbon chains are able to wrap up IONP and further prevent aggregation (Figure 2.12) (Rafiee et al., 2014).

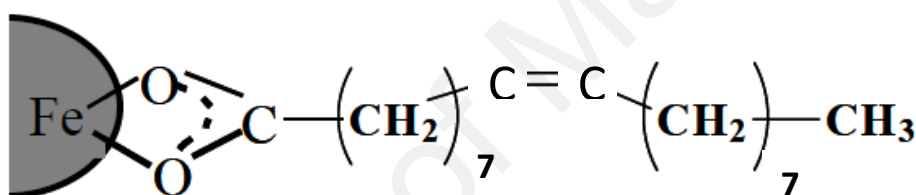


Figure 2.12: Stabilization of IONP via the grafted Oleic acid (Harris, 2002)

There is a possibility to incorporate Oleic acid with NBR latex owing to its hydrophilic carboxyl group and hydrophobic hydrocarbon groups. According to Liang et al. (2014), Oleic acid coated IONP was used to separate oil-water multiphase and treat oily wastewater. Maximum demulsification efficiency, ~98% was observed and it can be recycled up to 6 cycles.

#### 2.2.4.2 Saturated fatty acid (Palmitic acid, Stearic acid, Myristic acid and Capric acid)

Palmitic acid is the most common saturated fatty acid found in animals, plants and microorganism. It is used in processed food due to its low cost, and it is one of the components that can be found in palm trees. Due to its low cost, palmitic acid and its sodium salt was found widely used in foodstuffs. It consists of 16 carbon atoms in

molecule as shown in Figure 2.13. Stearic acid (octadecanoic acid) on the other hand is a saturated fatty acid with 18 carbon atoms in molecule (Figure 2.14). It is used as the main ingredient to produce detergents, soaps and cosmetics including shampoos and shaving cream products. Besides, it comes along with castor oil to prepare softeners in textile sizing. Apart from that, capric acid (decanoic acid) can be found in coconut oil and palm kernel oil. Capric acid is a unique fatty acid among them as it is the only one that is used in pharmaceuticals application. It has 10 carbon atoms in molecule as illustrated in Figure 2.15. Capric acid forms a salt or ester with drug will increase its lipophilicity and its affinity for fatty tissue. As a consequence, it will be able to deliver or distribute drug in fatty tissue faster. Lastly, myristic acid (tetradecanoic acid) which is commonly added co-translationally to the penultimate, nitrogen-terminus, glycine in receptor-associated kinases to confer the membrane localisation of the enzyme attributed to its high hydrophobicity nature. It consists of 14 carbon atoms in molecule as shown in Figure 2.16.

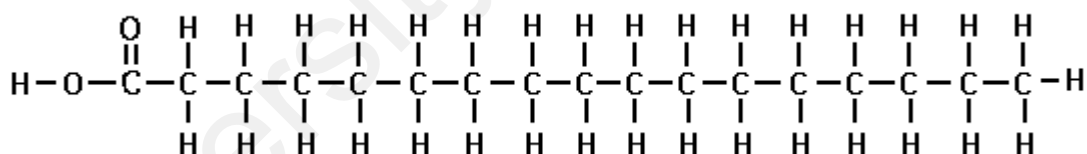


Figure 2.13: Chemical structure of Palmitic acid

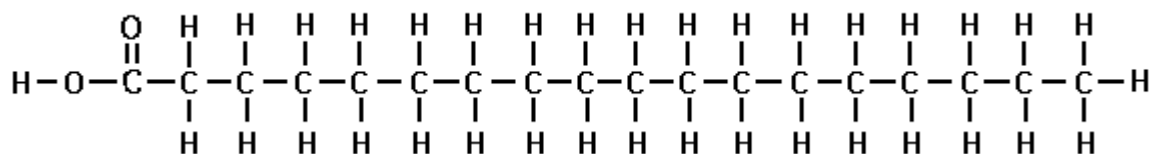


Figure 2.14: Chemical structure of Stearic acid

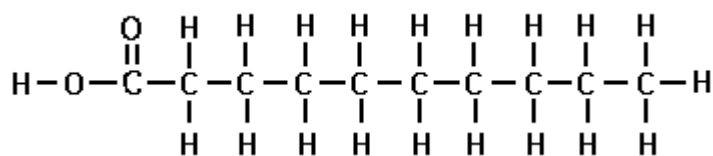


Figure 2.15: Chemical structure of Capric acid

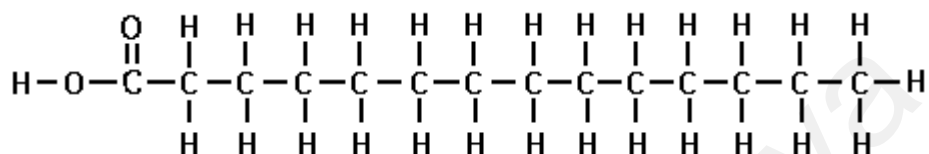


Figure 2.16: Chemical structure of Myristic acid

Saturated fatty acids with 10 to 15 carbon atoms in molecule are able to form stable colloidal stability in water compare to longer fatty acid which is more than 15 carbon atoms in molecule. Stearic acid and palmitic acid have more than 15 carbon atoms in molecule and its length is not able to cushion the colloidal particles against coagulation (Khalafalla & Reimers, 1980). However, stearic acid capped IONP was able to form smaller particle size (3 nm) compare to oleic acid capped IONP (5 nm) synthesized by thermal decomposition method (Teng & Yang, 2004). In this method, monodisperse IONP were synthesized by using iron carbonyl,  $\text{Fe}(\text{CO})_5$  in octyl ether. According to Jana, Chen, and Peng (2004) monodisperse nanocrystals achieved before Ostwald ripening stage when stearic acid was used as coating agent. Relative long chain of stearic acid (18 carbons per molecule) allows nearly monodisperse IONP with small size aggregates. In contrary, saturated fatty acids appear to have lower dispersion efficiency than oleic acid. This situation can be explained by high viscosity of saturated fatty acid results in larger specific surface of the saturated fatty acid coated IONP (Avdeev et al., 2009). Many researches have conducted to investigate dispersibility of

fatty acid coated IONP in water, but none of the study of fatty acid coated IONP in NBR latex was conducted.

### 2.3 Polymer composites

Carbon black has been well known to incorporate with rubber due to reinforcement properties of carbon black which can improve the mechanical properties of rubber/carbon black composite. Similarly, silica acts as reinforcement filler to NBR rubber by forming hydrogen bond in between acrylonitrile group of NBR and hydroxyl group of silica as shown in Figure 2.17 (Suzuki, Ito, & Ono, 2005). Agglomerates in the composites were suppressed by hydrogen bonding in between NBR and silica. Meanwhile, Yuan et al. (2000) reported that addition of Zinc oxide (ZnO)/ methacrylic acid (MAA) and Zinc oxide/ acrylic acid (AA) into NBR has a close relationship with the reinforcement of NBR. Indeed, ZnO/ MAA and ZnO/ AA generated salt crosslinks in NBR. Crosslink density in NBR was increased with increasing of ZnO/ MAA and ZnO/ AA. Meanwhile, they led to lower elongation at break.

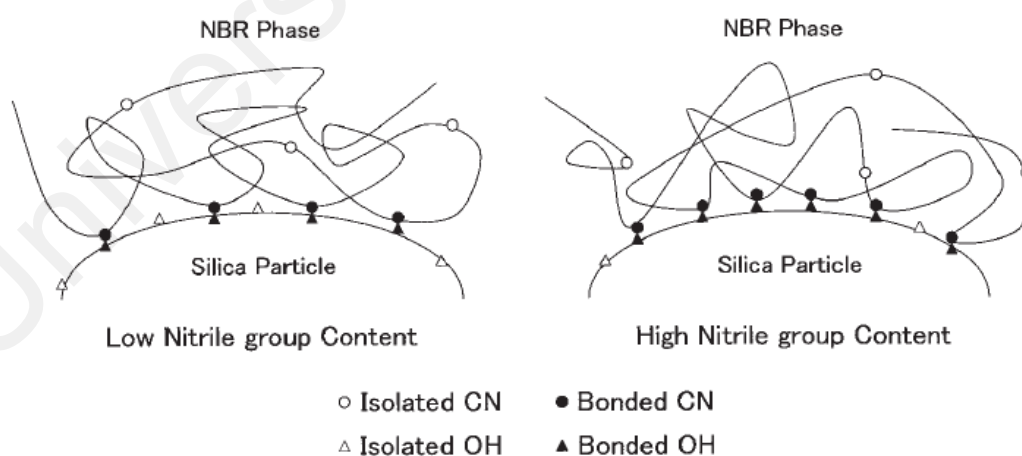


Figure 2.17: Schematic hydrogen bonding in between NBR and silica (Suzuki et al., 2005)

### 2.3.1 Magnetic polymer composites

Metal oxide particles were selected to add into polymer to enhance the electrical and thermal conductivity. Similarly, they played a vital role in application such as computer chip attributed to their small geometric dimensions changes and power output improvement. Weidenfeller et al. (2004) reported that thermal conductivity of polypropylene/ IONP and polyamide/ IONP increased from 0.22 to 0.93 Wm<sup>-1</sup>K<sup>-1</sup> for filler content of 44 vol% of IONP. Electrical resistivity on the other hand reduced from an insulator to 10 kΩm. Thermal and electrical conductivity was affected by the amount and particle size of IONP. Ramajo et al. (2009) investigated the dielectric and magnetic properties of IONP/ epoxy resin composites. The permittivity of IONP/ epoxy composite was highly relying on the filler concentration. Yang et al.(2008) was using block copolymer of [styrene-b-ethylene/ butylene-b-styrene] (SEBS) to incorporate with IONP. Increasing of IONP doping improve dielectric permittivity of SEBS/ IONP composite which has the same agreement with Ramajo et al. (2009). However magnetic permeability of SEBS composites was substantially given an impact by the IONP size within the block copolymer. This can be explained by thermal energy fluctuations from surrounding nanoparticles. Interestingly, shape memory polymers (SMP) were invented by using IONP and polymers (Behl et al., 2007). SMP has wide range of temperatures for shape recovery and high recoverable strain up to 400% (Razzaq et al., 2007). Shape recovery of SMP was determined by magnetization saturation of IONP and crystallization behaviour of selected polymer. An example of SMP which consists of IONP in silica matrix and polyetherurethanes is illustrated in Figure 2.18. Corkscrew-like spiral of initial shape of this thermoplastic composite was induced by magnetic field and turned out flattened after 22 seconds.

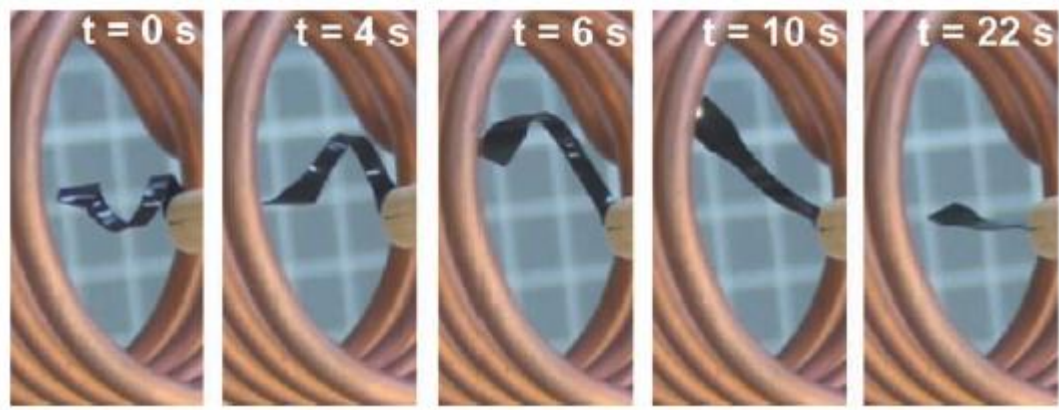


Figure 2.18: Magnetically induced shape-memory effect of thermoplastic composite  
(Behl, Razzaq, & Lendlein, 2010)

### 2.3.2 Magnetic rubber composites

#### 2.3.2.1 Magnetic natural rubber composites

Natural rubber is an unsaturated rubber and it has excellent mechanical strength, resilience and high elongation at break. Several types of filler are introduced into rubber to enhance their properties such mechanical strength, flexibility, density, magnetic and electrical properties (Kong et al., 2010; Tan & Abu Bakar, 2013; Zaborski & Masłowski, 2011). Ferrite with its promising magnetic properties, high stability and inexpensive is one type of fillers that is used in rubber composites. Makled et al. (2005) synthesized high coercivity barium ferrite ( $\text{BaFe}_{12}\text{O}_{19}$ ) powders by co-precipitation method and they are mixed into natural rubber with different loading level up to 120 phr. Throughout the research, they found that saturation magnetization was proportional to the addition of  $\text{BaFe}_{12}\text{O}_{19}$  meanwhile tensile strength was affected by volume fraction and size of ferrite particles. Besides, epoxidized natural rubber (ENR)/ IONP was *in situ* synthesized with an average particle size of IONP 3 to 6 nm deduced from TEM. Tan et al. (Tan & Abu Bakar, 2013) suggested that no chemical bonding exist between ENR and IONP due to no substantial peak wavenumber changing in FTIR spectra. The

electrical conductivity increased, and is aligned with the incorporation of IONP attributed to charge carrier migration of IONP.

### **2.3.2.2 Magnetic synthetic rubber composites**

Recently, IONP has been chosen to incorporate with nitrile butadiene rubber (NBR). Al - Ghamdi et al. (2012) successfully fabricated Electromagnetic Interference (EMI) shielding that is useful in microwave band. Electromagnetic radiation was listed as the third largest pollutant due to fast growth of microwave business and communication technology. IONP filled NBR with higher IONP content has better EMI shielding effect owing to high electrical conductivity and fast spin relaxation of IONP in NBR rubber. Kong et al. (2010) on the other hand studied microwave absorbing properties of Thermoplastic Natural Rubber (TPNR)/ IONP composite. Microwave absorbing properties were highly depending on filler concentration and sample thickness. Al - Juaid et al. (2011) agreed that IONP reinforced NBR by improving the overall performance. In addition, IONP filled NBR indicated excellent thermistor characteristic with good thermistor constant, thermistor sensitivity and stability factor in the range of temperature 25 to 100 °C. It was required to perform high quality industrial scale production of negative temperature coefficient of resistor thermistor. NBR consists of butadiene group which is flexible in nature, and this advantage brings the invention of flexible magnet. It was invented by Kroenke (1969) whereby barium ferrite was mixed with NBR to form flexible magnet. Lucas et al. (2009) suggested chromium oxide and magnetite was dispersed in NBR latex. The result showed that chromium oxide and magnetite are able to disperse uniformly in NBR latex, so that chromium oxide and magnetite are uniformly distributed in latex layer of glove. There is no sign of instability when chromium oxide and magnetite were introduced into the NBR latex formulation. Lucas et al. (2009) claimed that the size of chromium oxide was in the range of 0.3  $\mu\text{m}$  -15.00  $\mu\text{m}$ , while size of magnetite was not mentioned. Another



example of NBR latex composite which was patterned by (De Ricci & Phalip, 1999). Yttrium ferrite, iron ferrite and strontium ferrite embraced magnetic properties, and they were distributed uniformly in layer to form detectable polymeric protective glove. De Ricci et al. (1999) claimed that the polymer protective glove had maximum slope in hysteresis cycle more than  $5 \times 10^{-2} \text{ emug}^{-1}$ , coercive field about  $10^3 \text{ G}$  as well as particle size of ferrite in between 0.1 and 200  $\mu\text{m}$ . It was formed by at least one interior layer with ferrites distributed uniformly and the opposite sides without ferrites polymer layers. Further improvement can be achieved such as nano-size ferrites and higher magnetization saturation of ferrites are synthesised in order to reduce the final cost of glove and improve glove detectability effectiveness respectively.

### **2.3.3 Nano polymer composites**

Metal oxide nanoparticles (MONPs) have unique properties in terms of sorption behaviours, chemical reduction, magnetic activity and ligand sequestration among others. Due to their extraordinary properties, advantage has been taken in multitude of application including separation, sensing, catalyst biomedical application and environmental remediation (Sarkar et al., 2012). In fact, MONPs are prone to aggregation attributed to high surface area to volume ratio. Polymer was introduced to reduce aggregation, and at the same time it may leads to the properties enhancement of the composite. Some examples of MONPs incorporate with polymer matrix are summarized in Table 2.4.

Table 2.4: Nano polymer composite with their properties enhancement

Filler	Polymer matrix	Size of filler	Properties enhanced	References
Iron oxide (Fe <sub>3</sub> O <sub>4</sub> )	poly( $\epsilon$ -caprolactone) (PCL) and poly(cyclohexyl methacrylate) (PCHMA)	10 nm	i) Reduce elongation at break ii) Induce magnetic properties of composite	(Thevenot et al., 2013)
Titanium dioxide (TiO <sub>2</sub> )	Polystyrene	40 nm in length, 10 nm in width	i) Improve optical and electrical properties	(Rong et al., 2005)
	Polyaniline	25 and 50 nm	i) Enhance dielectric and conductivity	(Mo et al., 2008)
Zinc oxide (ZnO)	Polyaniline	30 – 50 nm	i) Improve electrical conductivity ii) Enhance porosity and surface activities of composite	(Khan & Khalid, 2010)
Silica (SiO <sub>2</sub> )	Epoxy	400 nm	i) Increase T <sub>g</sub> but decrease damping behavior	(Kang et al., 2001)
	Polyurethane	7 nm	i) Increase shear and storage modulus as well as tensile strength ii) Decrease T <sub>g</sub>	(Vega-Baudit et al., 2006)
	Polypropylene	50 – 100 nm	i) Larger thermal degradation stability ii) Larger elastic modulus	(Palza, Vergara, & Zapata, 2011)
Manganese oxide (MnO <sub>2</sub> )	Polystyrene-divinylbenzene	5 -190 nm	i) Greatly enhance absorption selectivity of material for target pollutant and its absorption capacity	(Lv et al., 2011)
Cerium oxide (CeO <sub>2</sub> )	Methyl methacrylate (MMA)	50 – 150 nm	i) High stability in between cerium and MMA	(Zgheib et al., 2012)
	Epoxy	< 100 nm	i) Enhanced up to 6.3% of tensile modulus ii) Tensile strength and elongation at break decreased with increasing CeO <sub>2</sub> loading iii) UV absorption was improved with small amount of CeO <sub>2</sub> in epoxy	(Dao et al., 2011)

### **2.3.3.1 Nano rubber composites**

Reinforcement of filler in natural rubber (NR) has become familiar and has been commercially applied in industries. It not only enhances desired properties, indeed it reduces material costs and improves NR processing cost too. Carbon black (CB) is the most common type of filler which is used to reinforce NR whereby it improves mechanical properties significantly. In order to introduce other properties into rubber, we investigated several types of filler incorporated with different rubber matrix which has been done by other researchers (Table 2.5).

University of Malaya

Table 2.5: Nano rubber composite with their properties enhancement

Filler	Rubber matrix	Size of filler	Properties enhanced	References
Iron oxide (Fe <sub>3</sub> O <sub>4</sub> )	EPM or NBR	-	i) Improve mechanical properties of composite ii) Improve magnetic properties and reinforce magnetorheological effect of composite	(Zaborski & Masłowski, 2011)
Palygorskite (PA)-cerium oxide (CeO <sub>2</sub> )	Natural rubber (NR) and styrene butadiene rubber (SBR)	5 nm	i) Strong rubber/filler interaction improves mechanical properties ii) Filler behave as an curing agent and facilitate curing reaction iii) Slightly improve thermal decomposition of the composite	(Zhao et al., 2012)
Manganese oxide (MnO <sub>2</sub> )	Acrylonitrile butadiene rubber (NBR)	-	i) Substantial increase in conductivity and decreasing activation energy o NBR. ii) Tensile strength and hardness increase with higher filler loading due to stronger interfacial bonding in between NBR and MnO <sub>2</sub>	(El-Nemr, Balboul, & Ali, 2014a)
Silica (SiO <sub>2</sub> )	Natural rubber (NR)	200 nm	i) Improve mechanical, dynamic and thermal aging properties ii) Enhancement in degree of filler dispersion, rubber-filler interaction and crosslink density of vulcanizates	(Prasertsri & Rattanasom, 2011)
Zinc oxide (ZnO)	Ethylene propylene diene monomer (EPDM)	30 – 80 nm	i) Improve thermal conductivity and slightly improve at dynamic mechanical properties due to strong filler-filler interaction ii) In-situ modification with silane improve dynamic properties by enhancing interfacial interaction	(Z. Wang et al., 2011)
Titanium dioxide (TiO <sub>2</sub> )	Natural rubber (NR)	20 -50 nm	i) Improve antimicrobial properties of composite ii) Slightly improve mechanical properties of composite	(Bindu & Thomas, 2013)
	Silicon rubber	-	i) Obstruct tree propagation in silicon rubber Increase magnitude of partial discharges	(Musa et al., 2013)

## CHAPTER 3

### MATERIALS AND METHODOLOGY

#### 3.1 Introduction

In this chapter the experimental setup used to produce nanoparticles, coated nanoparticles and fabrication of nanocomposites are presented in brief. Consequently, characterization techniques of each set up are explained in details. The results must be reproducible, and they are dependent on the experimental procedures and materials employed during the course of study. Syntheses of uncoated IONP and coated IONP as well as incorporation of IONP with NBR latex were reported. Each of these experimental steps has their own standard procedure and characterization method to accumulate data, subsequently investigate their properties. Various kinds of parameters including precipitation methods, precursor selections, flow rate, aging time, coating agent, coating agent to IONP ratio and ultra-sonication time are varied in order to achieve the optimum results. For the NBR nanocomposites fabrication method, different IONP loading on NBR latex was carried out to investigate the mechanical, morphological and magnetic properties of the composite. All the results recorded in this dissertation are reproducible within the given experimental limitation. In present work, maximum care is taken in conducting the experiments and collecting data and whenever necessary, some experiments were repeated. The following materials and methods are adopted in the present investigation.

#### 3.2 Materials

Chemicals used in this project are listed in Table 3.1. These chemicals were purchased from Merck Millipore, Sigma Aldrich and R&M Chemical. NBR latex and its compounding chemicals were provided by Hartalega Bhd. In this work, de-ionized

water (DI) (182 MΩ-cm at 25°C) was used to prepare all solutions and rinse all materials and glassware.

Table 3.1: Chemical list

Chemicals	Molecular Formula	Supplier	Purity (%)
<b>Precursors</b>			
Iron (II) sulphate heptahydrate,	FeSO <sub>4</sub> .7H <sub>2</sub> O	Merck	99.5
Iron (II) chloride tetrahydrate	FeCl <sub>2</sub> .4H <sub>2</sub> O	Merck	99.0
Ammonium hydroxide	NH <sub>4</sub> OH	Millipore Sigma Aldrich	30
<b>Fatty acids</b>			
Oleic acid	C <sub>18</sub> H <sub>34</sub> O <sub>2</sub>	R&M Chemical	90
Stearic acid	C <sub>18</sub> H <sub>36</sub> O <sub>2</sub>	Sigma Aldrich	99
Capric acid	C <sub>10</sub> H <sub>20</sub> O <sub>2</sub>	Sigma Aldrich	98
Myristic acid	C <sub>14</sub> H <sub>28</sub> O <sub>2</sub>	Sigma Aldrich	99 -100
Palmitic acid	C <sub>16</sub> H <sub>32</sub> O <sub>2</sub>	R&M Chemical	98
<b>Compounding chemicals</b>			
Nitrile butadiene rubber latex (NBR latex)	(C <sub>4</sub> H <sub>6</sub> ) <sub>n</sub> (C <sub>3</sub> H <sub>3</sub> N) <sub>m</sub>	Hartalega	-
Sodium Dodecyl Benzene Sulphonate (SDBS)	C <sub>12</sub> H <sub>25</sub> C <sub>6</sub> H <sub>4</sub> SO <sub>3</sub> Na	Hartalega	-
Zinc Dibutyldithiocarbamate (ZDBC)	[(C <sub>4</sub> H <sub>9</sub> ) <sub>2</sub> NCS <sub>2</sub> ] <sub>2</sub> Zn	Hartalega	-
Sulphur	S	Hartalega	-
Zinc oxide	ZnO	Hartalega	-
Titanium dioxide	TiO <sub>2</sub>	Hartalega	-

Table 3.1 (Continued): Chemical list

Chemicals	Molecular Formula	Supplier	Purity (%)
<b>Compounding chemicals</b>			
Aquawax	-	Hartalega	-
Calcium nitrate	$\text{Ca}(\text{NO}_3)_2$	Hartalega	-
Teric acid	-	Hartalega	-
Perfluorocarboxylic acid (PFCA)	$\text{CF}_3(\text{CF}_2)_6\text{COOH}$	Hartalega	-

### 3.3 Experimental Method

#### 3.3.1 Synthesis of IONP

0.2M of  $\text{FeSO}_4 \cdot 7\text{H}_2\text{O}$  solution was prepared by dissolving 3.03816 g of  $\text{FeSO}_4 \cdot 7\text{H}_2\text{O}$  salt into 50 ml of DI water. It was stirred for 10 min at 200 rpm to ensure that all salts are fully dissolved. On the other hand, 200 ml of DI water was prepared in 1 L of volumetric flask. Subsequently, 486.5 ml of 30% of  $\text{NH}_4\text{OH}$  was poured in the volumetric flask followed by adding DI water until 1 L. 100 ml of 6.5 M  $\text{NH}_4\text{OH}$  was measured prior to precipitation process.

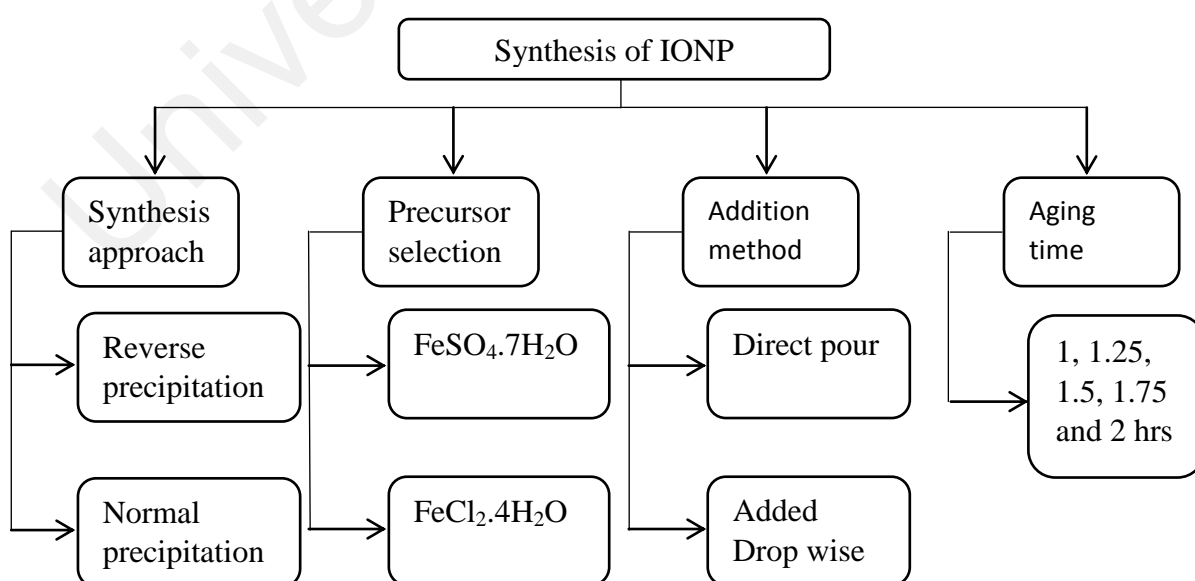


Figure 3.1: Variables of synthesis method of IONP

### 3.3.2 Synthesis of coated IONP (C-IONP)

Synthesized IONP was washed with 150 ml of DI water once to remove excess chemical remaining in the solution, while at the same time maintaining some of  $\text{NH}_4\text{OH}$  in it. Five fatty acids including oleic acid, palmitic acid, stearic acid, myristic acid and capric acid were selected as coating agent. The weight ratio of fatty acid to IONP was varied as 0.2, 0.4, 0.6, 0.8 and 1.0. Coated IONP was ultra-sonicated at 15, 30, 60, 90 and 120 mins. After that, compatibility test was conducted to confirm that coated IONP are able to disperse well in NBR latex. 1.3 g of coated IONP was weighed and mixed with NBR latex by stirring manually to ensure coated IONP were homogeneously distributed in NBR latex. The mixture was transferred to vial and sediment of coated IONP was observed and recorded at time intervals of 30 mins, 1 hr and 24 hrs.

### 3.3.3 Characterization of IONP

Composition, surface charge, morphology, sizes, magnetic properties, phases and weight percentage of IONP were analysed by X-ray diffraction (XRD), Zeta Sizer, High Resolution Transmission Electron Microscope (HRTEM), Vibrating Sample Magnetometer (VSM), Fourier Transform Infrared Spectroscopy (FTIR), Raman spectroscopy and Thermal Gravimetric Analyzer (TGA).

#### 3.3.3.1 X-ray diffraction (XRD)

XRD is one of the non-destructive testings for characterizing crystalline materials. Crystallite phase of IONP was determined by using  $\text{Cu K}\alpha$  radiation (XRD,  $\lambda = 1.5406 \text{ \AA}$ , Bruker AXS D8 Advance diffractometer). It provides information on structures, phase, preferred orientations and other structural parameters such as average grain size, crystallinity, strain and crystal defects. Approximately 1 g of the sample was measured and placed into sample holder. Before starting to run the test, step size was set at  $0.02^\circ$  with  $0.02^\circ/\text{s}$  scanning rate in between  $2^\circ$  and  $80^\circ$  diffraction angle ( $2\theta$ ). From the result,



crystallite size can be determined by using Scherrer equation (Equation 3.1). Phase composition of IONP was determined by Reitveld Refinement program.

$$\tau = \frac{K\lambda}{\beta \cos \theta} \quad (\text{Equation 3.1})$$

where:

- $\tau$  is the mean size of the crystalline domains;
- $K$  is a dimensionless shape factor, with a value close to unity. It has a typical value about 0.9 but varies with the actual shape of crystallite;
- $\lambda$  is the X-ray wavelength;
- $\beta$  is the line broadening at half the maximum intensity (FWHM);
- $\theta$  is the Bragg angle.

### 3.3.3.2 Zetasizer

Malvern Zetasizer Nano ZS was selected to investigate zeta potential, particle size distribution and polydispersity of IONP. It was a high performance two angle particle and molecule size analyser for the enhanced detection of aggregates and measurement of small or dilute samples as well as samples at very low or very high concentration using dynamic light scattering. This technique measured the diffusion of particles moving under Brownian motion, subsequently converted it into size and size distribution using Stokes-Einstein relationship. Approximately 0.001g of IONP was prepared and dispersed in 5 ml of DI water. Besides 0.2 ml of 3M ammonium hydroxide was dropped and the solution is around pH 10. The solution was ultra-sonicated for 1 hour in order to ensure IONP was well dispersed in deionized water. Zetasizer instrument was turned on for 30 mins in order to stabilise the laser. Next, the dispersed solution was injected into disposable polystyrene (DTS0012) and folded capillary cell (DTS1060), measuring hydrodynamic size and zeta potential, respectively. Then, the

required cell was inserted into the instrument and allowed for the temperature to stabilise. Finally, slurry charge and particle size distribution measurement were analysed, and results were collected.

#### **3.3.3.3 High Resolution Transmission Electron Microscope (HRTEM)**

HRTEM analysis was performed by JEM-2100F instrument with accelerating voltage 200 kV. It has become a major support in the list of characterization techniques for materials scientists attributed to its capability of producing both image and diffraction information from a single sample. Furthermore, materials characterization could be determined via radiation produced by beam electrons accelerated on the sample. It offers high magnification up to 1.6 times magnification which is able to observe extremely small and tiny lattice-fringe spacing. Prior to HRTEM characterization, samples were prepared by dropping dispersed IONP on copper grids of 300 mesh. The sample prepared was left overnight. After that, sample prepared on copper grid was placed into HRTEM sample holder before inserting into the HRTEM. Image of IONP was selected and taken at 50000, 100000 and 500000 times magnification. Size and lattice-fringe spacing was measured by image-J. Particle size distribution can be plotted after 100 IONP particles were measured and lattice-fringe spacing was used to support XRD information.

#### **3.3.3.4 Vibrating Sample Magnetometer (VSM)**

VSM was invented by Simon Foner (a scientist of the MIT) in 1956, and it has been widely used to determine magnetic properties of large variety materials: diamagnetic, paramagnetic, ferromagnetic and antiferromagnetic. Vibrating Sample Magnetometer (Lakeshore – VSM 7407) was used to study magnetic properties of IONP. Roughly 0.03g of IONP was prepared in the sample holder and placed at centre in a pair of pickup coils between the poles of an electromagnet. The sample was mounted with a sample rod in a transducer assembly and it passes via the centre of driving coil. The

transducer was driven by power amplifier which itself is driven by an oscillator at frequency of 71 Hz. The sample vibrated along the z-axis perpendicular to the magnetizing field and it induced signal that indicated the magnetic properties itself. Continuously hysteresis and magnetic field from 10000 G to -10000 G and from -10000 G to 10000 G was applied to identify magnetization saturation ( $M_s$ ), coercivity ( $H_c$ ) and remanence ( $M_r$ ) of IONP.

#### **3.3.3.5 Fourier Transform Infrared Spectroscopy (FTIR)**

The FTIR spectrum showed the molecular absorption and transmission (specific frequency of energy) which is useful to determine IONP's functional group, other attached molecule's functional group and the functional group linked in between IONP with the molecules. Before putting the sample in sample holder, the sample holder was cleaned by acetone. About 0.3 mg of IONP was mixed with 4 mg of KBr and moulded to form pellet. Pellet was placed in the FTIR and IR radiation was passed through it. Some of the IR radiation was absorbed by sample and some of it was passed via transmission. Resolution of FTIR was set at  $4\text{ cm}^{-1}$  with 16 scans in the wavelength range  $400\text{ cm}^{-1}$  to  $4000\text{ cm}^{-1}$ . FTIR spectrum was collected with labelled peaks.

#### **3.3.3.6 Raman spectroscopy**

Raman Spectroscopy (Renishaw in Via Reflex with high performance CCD camera and LEILA microscope is used in this study. It is one of the vibrational spectroscopy techniques widely used to provide information on chemical structures and physical forms. It was used to determine substance (phase) from the characteristic spectral patterns and quantitatively or semiquantitatively amount of substance in IONP with high lateral resolution. Approximately 0.05g of sample was placed into the sample holder, subsequently inserted into Raman spectrometer. Sample degradation and fluorescence might be happened in the process of testing. It will give a big impact on highly sensitive material like IONP. Hence, 1 percent of 0.2 mW laser power with 180

seconds exposure time was chosen to analyse IONP. Argon gas laser (514 nm) was selected in this research as  $1800\text{ mm}^{-1}$  spectral due to its resolution is sufficient to plot a good spectra. Scattered radiation was collected by focusing laser beam via  $\times 50$  objective and the laser spot on sample was approximately  $0.836\text{ }\mu\text{m}$  with 514 nm excitation. The obtained Raman spectra was analysed and different phases of IONP was determined.

### **3.3.3.7 Thermal Gravimetric Analyzer (TGA)**

TGA is a technique that measures the change in weight of sample when it is heated, cooled or held at constant temperature. It was used to characterize materials with regard to their composition Sample of about 4 mg – 5 mg was examined by TGA (Mettler Toledo, TGA/SDTA-851 $^{\circ}$ ) by putting it into 100  $\mu\text{l}$  of open alumina crucible. The experimental temperature was set from ambient to  $800\text{ }^{\circ}\text{C}$  at heating rate of  $10\text{ }^{\circ}\text{C}/\text{min}$  under nitrogen gas with flow rate of 50 ml/min. Then, it was cooled to room temperature. This technique was used to identify the composition ratio of coating agent: IONP, NBR latex: IONP and NBR latex: coating agent: IONP.

### **3.3.4 Compounding of C-IONP with NBR latex**

Firstly, mixing tank was cleaned thoroughly by using brushes and detergent to ensure that no contamination during compounding process. 700 g of 43% total solid content (TSC) of NBR latex was filtered and transferred to the mixing tank. It was stirred for 30 minutes with 50 rpm stirring speed. After that, pH of the latex was adjusted at pH 9.6 to 9.7. The TSC of latex was continuously checked to be maintained at 43 %. Next, 18.06 g of Sodium Dodecyl Benzene Sulphonate (SDBS) was slowly added into the latex and continued by stirring process for an hour. Once again, pH of the compound latex was measured and it was adjusted to pH 9.6 to 9.7. In the meantime, 3.61 g of Dibutyldithiocarbamate (ZDBC), 7.02 g of sulphur, 6.52 g of Zinc oxide (ZnO) and 9.03 g of Titanium dioxide ( $\text{TiO}_2$ ) were weighed. All of these chemicals were slowly

added into the latex compound and stirred for another 1 hour. Then, stirring speed was slow down to 30 rpm and left overnight. TSC of compounded latex was checked and diluted by DI water to 23%. At this stage, 5, 10, 15 and 20 phr of coated IONP as well as 12.04 g of aqua wax was added slowly into the compounded latex. It was stirred for 1 hour and recorded of TSC and pH. Figure 3.2 shows the overall flow process of latex compounding.

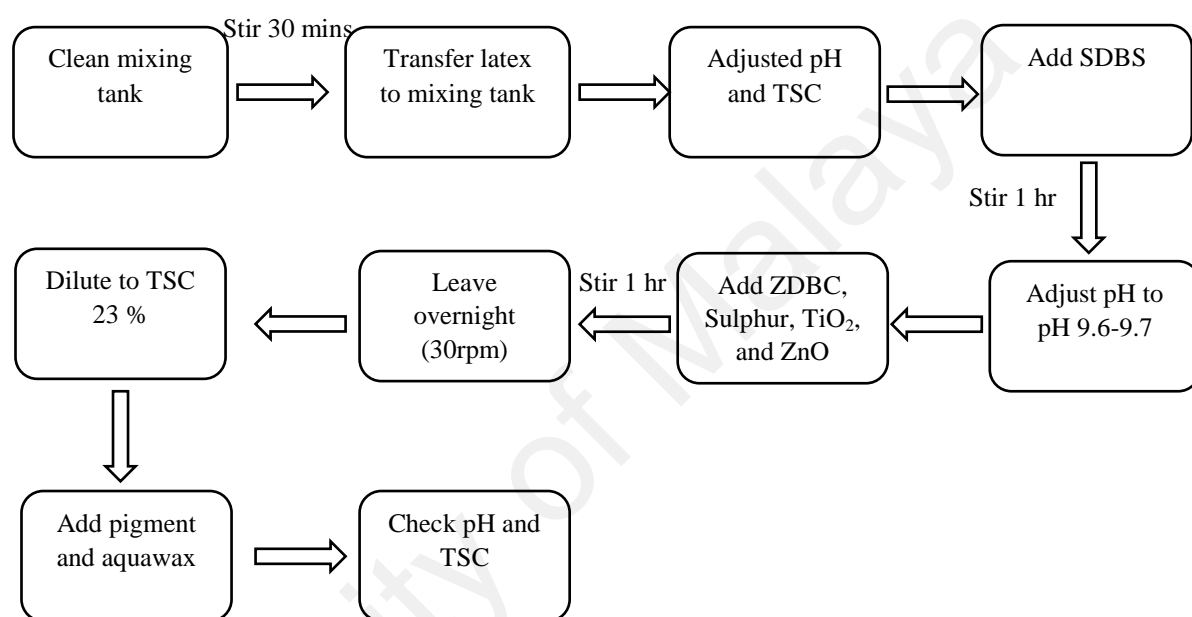


Figure 3.2: Flow chart of compounding process

### 3.3.5 Dipping process of NBR film

Coagulant is used to accelerate coagulation of latex on the surface of former plate. It was prepared through the addition of 485.68 g calcium nitrate (CN), 25 g of perfluorocarboxylic acid (PFCA) and 2 g of teric acid into 1487.32 g of water at 60 °C. Compounded latex was filtered and poured into a dipping tank. Prior to that, former plates were thoroughly cleaned with brushes and rinsed with copious amount of water in order to prevent latex remaining on them which can lead to defects on final films. Former plates were dried in an oven at 100 °C for 5 minutes. After that, the dried former plates were dipped until it exceeded the line (Figure 3.3), followed by drying for another 5 minutes at the same temperature. Once the former was taken out form oven, it

was cooled down at room temperature for 30 seconds before they are dipped again into latex compound. Dwell time was set as 8, 4, 8 seconds for dipping in, stop, and dipping out, respectively. The former were cured at 125 °C for 20 mins, followed by leaching with DI water at 40 °C for 30 seconds. Next, the former were dried at 125 °C for 10 minutes. Finally, the former was cooled down at room temperature and latex film was stripped out from the formers. Overall dipping process is illustrated in Figure 3.4. The overall flow chart from IONP synthesis to NBR composite film was illustrated in Figure 3.5.

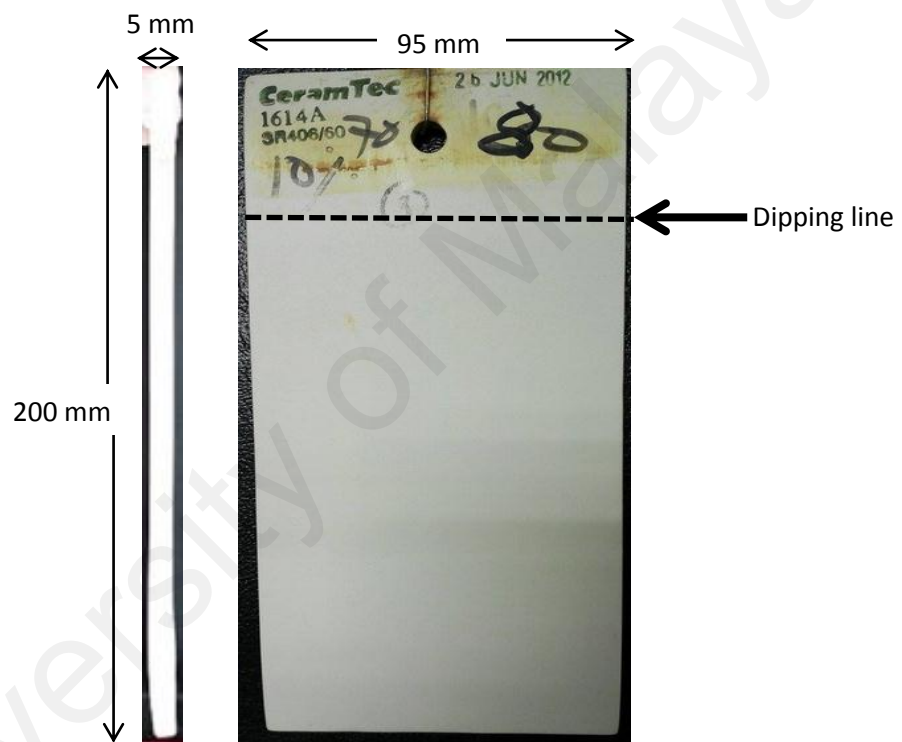


Figure 3.3: Former plate of latex film

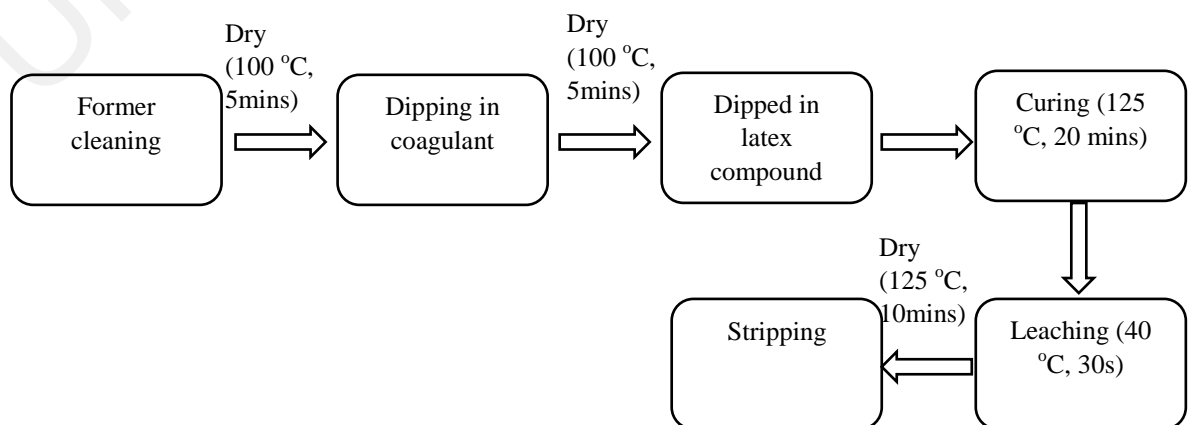


Figure 3.4: Flow chart of dipping process

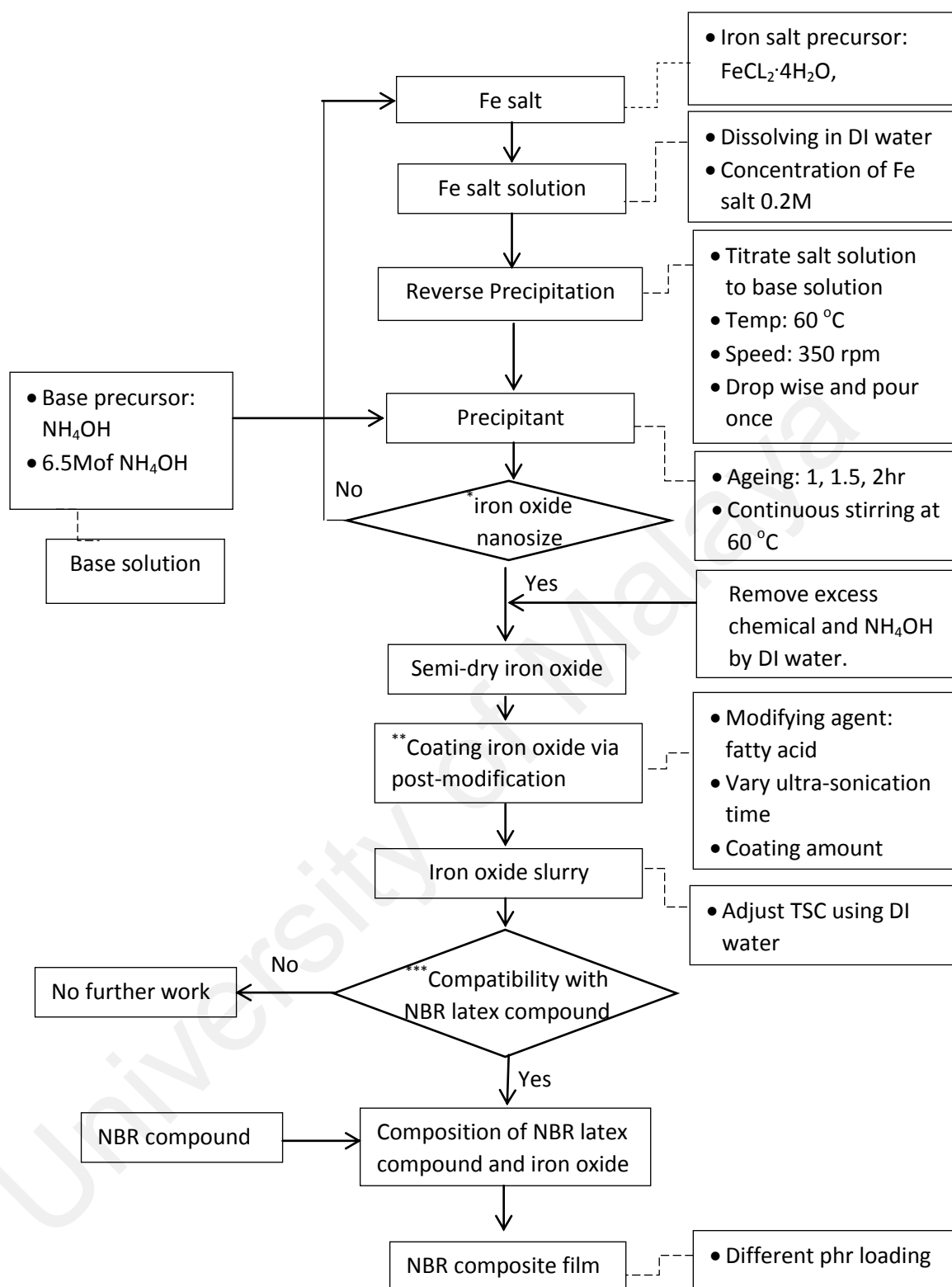


Figure 3.5: Overall flow chart of IONP synthesis and incorporation into NBR compound

### 3.3.6 Characterization of NBR composite film

Mechanical and magnetic properties, morphology (fracture surface), weight percentage as well as thermal stability were analysed by Universal Testing Machine, Vibrating Sample Magnetometer (VSM), Scanning Electron Microscope (SEM), Fourier Transform Infrared Spectroscopy (FTIR), Raman spectroscopy and Thermal Gravimetric Analyzer (TGA). VSM, FTIR and TGA have been discussed in Sections 3.3.3.5, 3.3.3.6, and 3.3.3.8 respectively. In these sections, IONP was substituted by NBR composite film.

#### 3.3.6.1 Universal Testing Machine (Instron 3345)

##### 3.3.6.1.1 Tensile Test (ASTM D 412)

The tensile strength and modulus of NBR composite film was measured by Universal Testing Machine. Specimens were cut in the shape of dumbbell (Figure 3.6) and their lengthwise direction was parallel to the flow direction of latex after dwelling. The thickness was measured prior to testing. The specimens were gripped at gauge length 50 mm and being pulled at constant cross head speed of 500 mm/min. In each case, five specimens were tested as well as the average value of tensile stress (TS), strain, elongation at break and modulus were tabulated. Calculation of tensile stress, strain, elongation at break and modulus were shown in Equation 3.2 – 3.5.

$$\text{Tensile stress} = \frac{\text{load at break}}{(\text{original width})(\text{original thickness})} \quad (\text{Equation 3.2})$$

$$\text{Strain} = \frac{\text{elongation at rupture}}{\text{initial gage length}} \quad (\text{Equation 3.3})$$

$$\text{Elongation at break} = \text{Strain} \times 100 \quad (\text{Equation 3.4})$$

$$\text{Modulus} = \frac{\text{stress}}{\text{strain}} \quad (\text{Equation 3.5})$$



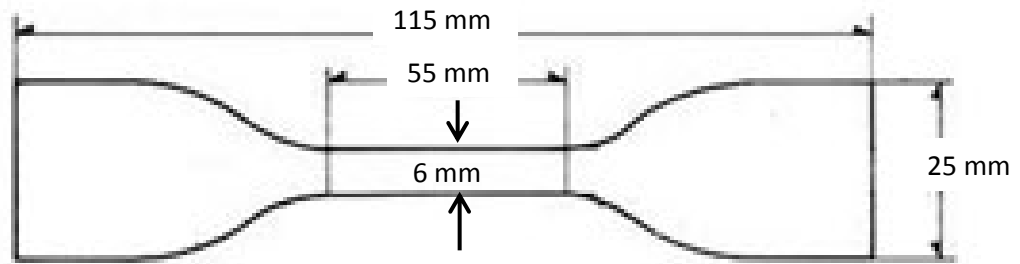


Figure 3.6: The shape of NBR composite film for tensile test

### 3.3.6.2 Field Emission Scanning Electron Microscopy (FESEM)

Morphology of the composites was investigated by using scanning electron microscope (HITACHI SU 8030). The samples were mounted onto sample holder using double sided electrically conducting carbon adhesive tapes to prevent surface charge on the specimens when exposed to the electron beam. The fracture surfaces of NBR composite film obtained from tensile testing were sputter with platinum prior to their morphological observation. The FESEM micrographs were obtained under conventional secondary electron imaging conditions with acceleration voltage of 5 kV.

## CHAPTER 4

### RESULTS AND DISCUSSION

#### 4.1 Synthesis of IONP

IONP was synthesized by precipitation method, which consists of several parameters including synthesis approach, precursor selection, addition method and aging time. These parameters are useful to determine the phase, particle size as well as magnetic properties of IONP as additive in NBR matrix.

##### 4.1.1 XRD analysis

XRD pattern of IONP with different synthesis parameter were shown in Figure 4.1 with their phase composition and crystallite size presented in Table 4.1. In general, four different parameters including synthesis approach, precursor selection, addition method and aging time were studied on synthesis of IONP. Generally, all XRD spectrum confirmed that magnetite and maghemite were formed with references of JCPD card (19-0629) and JCPD card (39-1346). It can be observed that magnetite and maghemite coexisted in IONP which can be attributed to unstable  $\text{Fe}^{2+}$  cations in inverse-spinel magnetite octahedral site which easily oxidised into  $\text{Fe}^{3+}$ . This is applicable to both synthesis methods since open environment conditions have been applied to synthesize the IONP (room temperature and humidity) (Kim et al., 2001). Meanwhile, goethite was an intermediate of ferrous hydroxide and it also recorded due to present of  $\text{O}_2$  during synthesis process (Mandel et al., 2011).

In synthesis approach parameters, IONP synthesized by reverse precipitation method consists 79.2 % content of magnetite phase than IONP synthesized by normal precipitation (74.3 %). It has been reported that, magnetite has the highest magnetization saturation which consequently brought to the higher magnetite phase,

and better magnetic properties of IONP (Laurenzi, 2008). Maghemite of reverse precipitation is lower due to less on conversion of magnetite to maghemite phase. In reverse precipitation, magnetite was formed once iron salt solution was added into  $\text{NH}_4\text{OH}$  with the reduction of pH from 13 to 11. Meanwhile, pH of normal precipitation method was increased from the value 3.7 to 11. On the other hand, magnetite had a tendency to form in reverse precipitation method especially in the pH medium of 8.5 (Baumgartner et al., 2013). Other than that, the crystallite size of IONP of reverse precipitation (28.2 nm) is smaller than IONP of normal precipitation (34.3 nm). It can be explained by growth rate of IONP for the normal precipitation approach is higher than IONP of reverse precipitation. This statement has been supported by other studies that claimed crystallite and particle size reduction were caused by limited position of  $\text{NH}_4\text{OH}$  during titration addition into the iron salt solution (Kazemzadeh et al., 2012; Mizukoshi et al., 2009).

Furthermore, for the precursor selection analysis,  $\text{FeSO}_4 \cdot 7\text{H}_2\text{O}$  and  $\text{FeCl}_2 \cdot 4\text{H}_2\text{O}$  were chosen as iron precursor due to their wide usage in synthesis of IONP. In Table 4.1, it was observed that magnetite of  $\text{FeSO}_4 \cdot 7\text{H}_2\text{O}$  sample (79.2 %) was higher than  $\text{FeCl}_2 \cdot 4\text{H}_2\text{O}$  sample (73.8 %). Meanwhile, maghemite and hematite of  $\text{FeSO}_4 \cdot 7\text{H}_2\text{O}$  sample was lower than  $\text{FeCl}_2 \cdot 4\text{H}_2\text{O}$  sample. Content of goethite of  $\text{FeSO}_4 \cdot 7\text{H}_2\text{O}$  sample on the other hand was 4.2 % lower than  $\text{FeCl}_2 \cdot 4\text{H}_2\text{O}$  sample. This situation explained that  $\text{FeSO}_4 \cdot 7\text{H}_2\text{O}$  sample has better magnetic properties than  $\text{FeCl}_2 \cdot 4\text{H}_2\text{O}$  sample. Crystallite size of  $\text{FeSO}_4 \cdot 7\text{H}_2\text{O}$  sample (28.2 nm) is near to  $\text{FeCl}_2 \cdot 4\text{H}_2\text{O}$  sample (29.8 nm). Thus, it can be said that crystallite size is hard to determine the selection of IONP in this parameter. According to Maldonado et al. (2014), small difference recorded on the crystallite size has no obvious impact on magnetic properties. Therefore, it is concluded that precursor selection did not contribute to any significant effect on the magnetic properties of the synthesized IONPs.

Pour once and drop wise of precipitating agent techniques have been selected as the other interested parameters in this study. In general, pour once method led to prominently formation of high magnetite phase (79 %) as compared to dropwise method (42.8 %). Contrary to maghemite, it found that hematite and goethite has greater tendency to growth for the pour once method (Table 4.1). Peak intensity of pour once method was vividly higher than drop wise method as presented in Figure 4.1(c). As discussed, magnetite contributed the highest magnetic properties compare to others. Therefore, IONP synthesized by pour once method was better than IONP synthesized by drop wise method. In fact, drop wise method contributed significantly smaller crystallite size (13.2 nm) which was 15 nm smaller than pour once method. This is attributed to the slower addition rate of precipitation during the oxidation process. IONPs with greater crystalline size is generally produced by the pour once method which brought to the better magnetic properties (Demortiere et al. (2011)).

For aging time parameter, it was observed that IONP with 1.5 aging time has the highest percentage of magnetite and maghemite which are 82 and 16 %, respectively as compared to IONP synthesis through other aging time. Consequently, the greatest peak intensity is obtained from the IONPs synthesized with 1.5 hours aging time. Besides that, percentage of hematite was consistently increased from 0.8 to 9.9 % as aging time was increased gradually from 1 to 2 hrs. It can be said that increment of aging time would probably lead to oxidation of magnetite to maghemite and hematite. Percentage of goethite on the other hand was reduced from 2.1 to 0.2 % with the increasing aging time. It can be predicted that magnetic properties was improved once aging time was increased from 1 to 1.5 hours but tend to reduced when aging time further increased from 1.5 to 2 hrs. At this range of aging time, IONPs the oxidation process of magnetite and maghemite would bring to formation of hematite. There is not much change in crystallite size when the aging time was increased from 1 to 2 hrs as shown in Table 4.1.

Table 4.1: Crystallite size and phase composition of IONP with different synthesis parameter

	Magnetite (%)	Maghemite (%)	Hematite (%)	Goethite (%)	Crystallite size (nm)
<b><i>Synthesis approach</i></b>					
Reverse precipitation	79.2	15.9	2.8	2.1	28.2
Normal precipitation	74.3	24.3	0.2	1.2	34.3
<b><i>Precursor selection</i></b>					
FeSO <sub>4</sub> 7H <sub>2</sub> O	79.2	15.9	2.8	2.1	28.2
FeCl <sub>2</sub> 4H <sub>2</sub> O	73.8	18.4	1.4	6.3	29.8
<b><i>Addition method</i></b>					
Pour once	79.2	15.9	2.8	2.1	28.2
Dropwise	42.8	36.5	17.2	3.5	13.2
<b><i>Aging time</i></b>					
1.0 hr	79.2	15.9	2.8	2.1	28.2
1.25 hrs	81.1	15.7	0.9	2.3	25.7
1.5 hrs	82.0	16.0	1.3	0.7	26.0
1.75 hrs	80.5	14.3	5	0.2	23.8
2.0 hrs	78.4	11.5	9.9	0.2	26.3

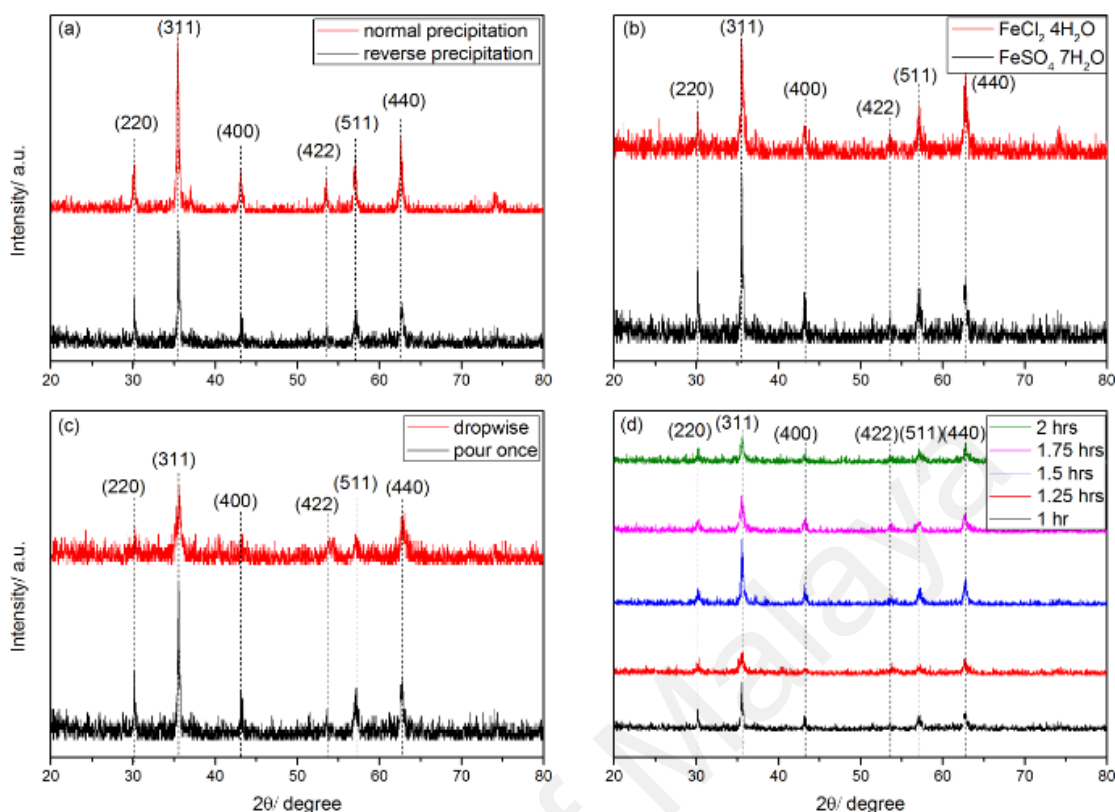


Figure 4.1: XRD analysis on IONP via (a) synthesis approach, (b) precursor selection, (c) addition method and (d) aging time

#### 4.1.2 Raman spectroscopy analysis

Theoretically, values of standard IONP phases for the Raman spectroscopy analysis were tabulated in Table 4.2 in order to compare with synthesized IONP. Depicted in Figure 4.2 is a Raman spectrum of IONP where different phases are shown in different peaks. Basically, 4 phases of IONP are existed namely: magnetite, maghemite, hematite and goethite. Most of the peaks after  $1100\text{ cm}^{-1}$  are not meant for IONP phase identification was reported by Chourpa et al. (2005). A big hump at  $1400\text{ cm}^{-1}$  can be seen in Figure 4.2 was mostly caused by IONP prepared in purified water (Chourpa et al., 2005). It was noticed that magnetite, maghemite and goethite were coexisted in all selected parameters.

No hematite phase was observed in reverse precipitation synthesis approach instead of the normal precipitation synthesis approach. In precursor selection parameter, no hematite can be detected by Raman spectroscopy. Both spectra were identical to each other and it was hard to identify which precursor was better in Raman characterization. Thus, other characterizations techniques were carried out.

In addition method parameter, three peaks were recorded in Raman spectra synthesized by dropwise method which were 670, 300 and 400  $\text{cm}^{-1}$ , representing of magnetite, hematite and goethite. Besides that, only single peak of magnetite was determined and none of the maghemite was identified due to conversion of maghemite to hematite. Comparatively, IONP synthesized by pour once method consisted of magnetite, maghemite and goethite. Due to lack of magnetite and maghemite in IONP synthesized by dropwise method, it is predicted that it will decrease magnetization saturation substantially.

During Raman characterization of different aging time samples, no hematite phase was recorded in series of spectrum. This might due to low percentage of hematite presence below the detection limit of Raman spectroscopy. It can be seen that in Figure 4.2, shoulder peak for IONP synthesized by 1.75 hrs aging time was higher than the other types IONP synthesized by 1, 1.25, 1.5 and 2 hrs aging time. This indicates percentage of magnetite increased with the goethite and ferrous hydroxide as shown in Figure 4.3. However, IONP synthesized at 1.75 hrs aging time might not achieve the highest magnetization saturation ( $M_s$ ) attributed to slightly increase of hematite phase as deduced in XRD analysis. It will be further discussed in the magnetic properties analysis. It can be observed as well that Raman peak at 389  $\text{cm}^{-1}$  was shifted to 381  $\text{cm}^{-1}$  for 1 hr to 1.5 hrs aging time, and diminished from IONP synthesized at 1 to 2 hrs aging time. This phenomenon supported on the transformation of goethite to magnetite with increase in aging time from 1 to 2 hrs. Hence, Raman analysis demonstrated that

increasing aging time on the synthesis of IONP was able to improve magnetite phase of IONP.

Table 4.2: Raman peaks of IONP with different synthesis parameter

	Magnetite (cm <sup>-1</sup> )	Maghemite (cm <sup>-1</sup> )	Hematite (cm <sup>-1</sup> )	Geothite (cm <sup>-1</sup> )
Theory (Slavov et al., 2010)	193, 668	350, 500, 700	225, 299, 412	400
<b><i>Synthesis approach</i></b>				
Reverse precipitation	190, 670	350, 500, 708	NA	400
Normal precipitation	190, 670	350, 500, 716	225	400
<b><i>Precursor selection</i></b>				
FeSO <sub>4</sub> 7H <sub>2</sub> O	190, 670	350, 500, 708	NA	400
FeCl <sub>2</sub> 4H <sub>2</sub> O	190, 670	350, 500, 708	NA	400
<b><i>Addition method</i></b>				
Pour once	190, 670	350, 500, 708	NA	400
Dropwise	670	NA	300	400
<b><i>Aging time</i></b>				
1.0 hr	189, 667	340, 499, 705	NA	389
1.25 hrs	675	498, 704	NA	387
1.5 hrs	192, 665	343, 500, 712	NA	381
1.75 hrs	674	342, 498, 709	NA	NA
2.0 hrs	189, 674	340, 503, 706	NA	NA

\* NA = Not available



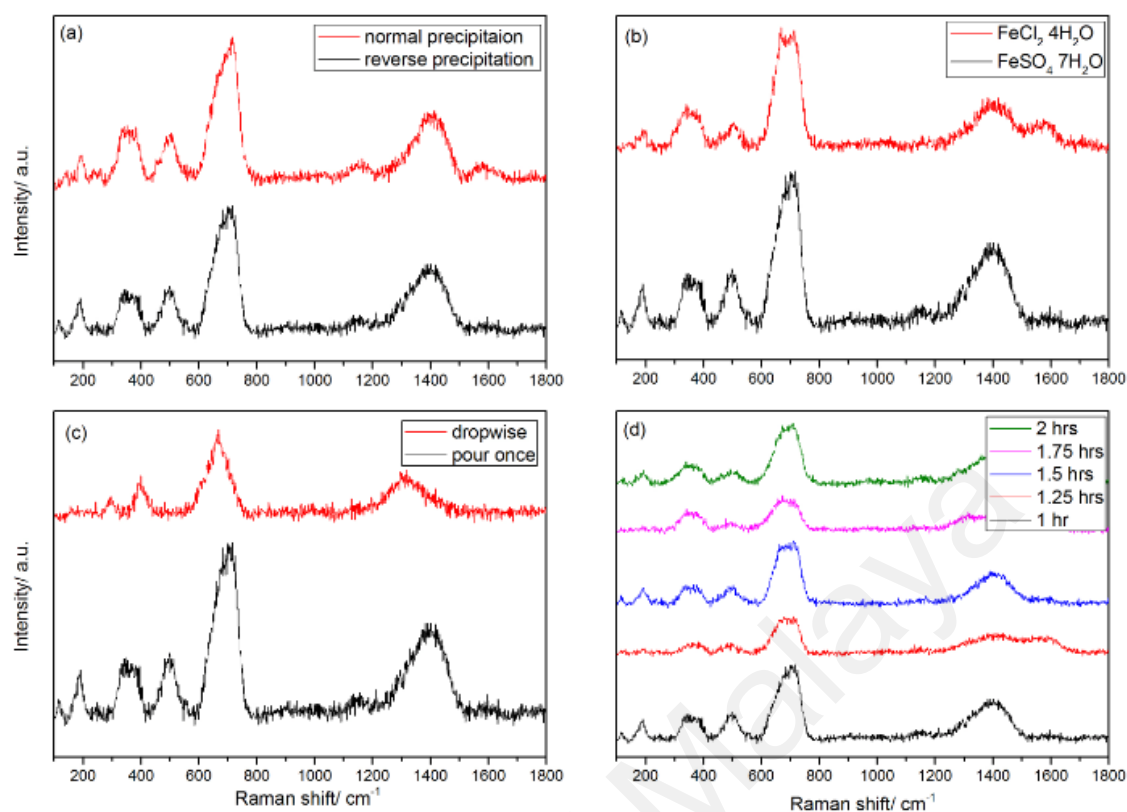


Figure 4.2: Raman spectra of IONP via (a) synthesis approach, (b) precursor selection, (c) addition method and (d) aging time

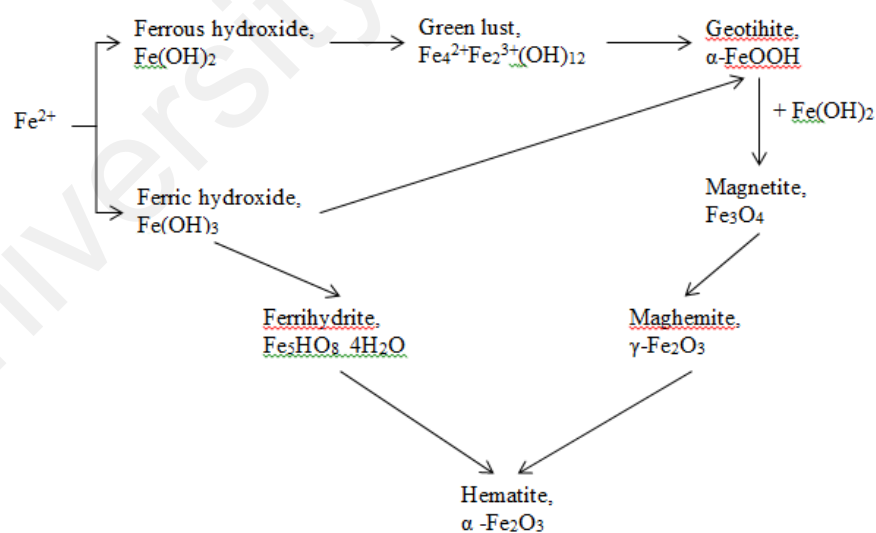


Figure 4.3: Formation path way of magnetite via precipitation method

### 4.1.3 FTIR analysis

FTIR peaks of IONP with different synthesis parameters summarized in Table 4.3 with the spectra are presented in Figure 4.4. Theoretical value of magnetite, maghemite and goethite peaks is illustrated. According to Slavov et al. (2010), magnetite existed at the following wavelength  $580\text{ cm}^{-1}$  [ $\nu$  (F-O) stretching vibration in tetrahedral site],  $895 - 770\text{ cm}^{-1}$  (Fe-O-H bending vibration in goethite) and  $630\text{ cm}^{-1}$  (maghemite).

It can be seen that magnetite, maghemite and goethite co-existed in both IONP synthesized by reverse and normal precipitation approaches.  $\text{FeSO}_4 \cdot 7\text{H}_2\text{O}$  and  $\text{FeCl}_2 \cdot 4\text{H}_2\text{O}$  have the same situation as synthesis approach. This observations in FTIR is in good agreement with XRD and Raman characterization.

For the addition method parameter, it was noticed that IONP synthesized by pour once method had two significant peaks at  $809.76$  and  $894.38\text{ cm}^{-1}$  (goethite). Meanwhile, only a single peak at  $807.28\text{ cm}^{-1}$  was observed in IONP synthesized by drop wise method. It shows the weak detection of goethite in IONP synthesized by drop wise method. Another peak ( $1124.76\text{ cm}^{-1}$ ) identified in IONP synthesized by drop wise method due to OH bending of Feroxyhyte ( $\delta\text{-FeOOH}$ ). However, this IONP phase does not contribute to magnetic properties.

For aging time parameter, magnetite and maghemite are co-existed in IONP synthesized at 1, 1.25, 1.5, 1.75 and 2 hrs aging time. However, goethite peaks can be observed only on IONP synthesized at 1 and 1.25 hrs aging time which is  $809.76$  as well as  $894.38\text{ cm}^{-1}$  and  $885.11\text{ cm}^{-1}$  due to Fe-O-H bending vibration in goethite. It clearly indicated that goethite was almost eliminated once the aging time was increased to 1.5 hrs and above. It further confirmed that decreasing of goethite as increasing of aging time can be attributed to further reaction of unreacted ferrous hydroxide and goethite to form magnetite as shown in Figure 4.4.

Table 4.3: FTIR peaks of IONP with different synthesis parameter (Slavov et al., 2010)

	Magnetite (cm <sup>-1</sup> )	Maghemite (cm <sup>-1</sup> )	Geothite (cm <sup>-1</sup> )
Theory	580	630	895 – 770
<b><i>Synthesis approach</i></b>			
Reverse precipitation	584.31	633.11	809.76, 894.38
Normal precipitation	584.31	627.53	794.00, 895.92
<b><i>Precursor selection</i></b>			
FeSO <sub>4</sub> 7H <sub>2</sub> O	584.31	633.11	809.76, 894.38
FeCl <sub>2</sub> 4H <sub>2</sub> O	576.59	627.55	806.98, 906.73
<b><i>Addition method</i></b>			
Pour once	584.31	633.11	809.76, 894.38
Dropwise	576.90	633.11	807.28
<b><i>Aging time</i></b>			
1.0 hr	584.31	633.11	809.76, 894.38
1.25 hrs	581.84	631.56	885.11
1.5 hrs	579.37	626.93	NA
1.75 hrs	580.29	631.87	NA
2.0 hrs	583.38	629.40	NA

\* NA = Not available

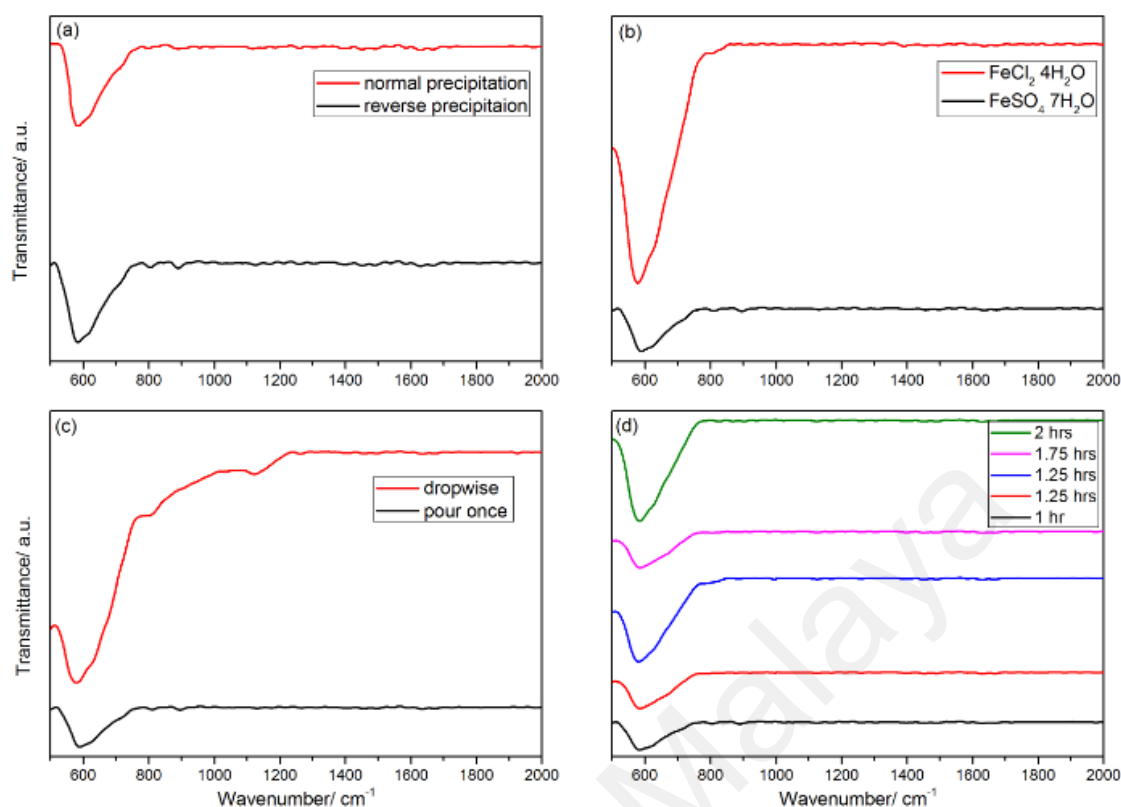


Figure 4.4: FTIR spectra of IONP via (a) synthesis approach, (b) precursor selection, (c) addition method and (d) aging time

#### 4.1.4 Zeta size analysis

Average hydrodynamic size, polydispersity index (PDI) and zeta potential as well as hydrodynamic size distribution of IONP synthesized with different parameters were shown as in Table 4.4 and Figure 4.5, respectively. All IONP synthesized show monomodal normal distribution and asymmetric (skewed to right). This indicates small size IONPs (< 100 nm) is higher than bigger size of IONP (> 100 nm). All IONP were recorded to have greater zeta potential than -35 mV were metastable. This is due to the preparation medium which is water at pH 10. According to Sun et al. (2006), iso-electric point (IEP) of IONP was near pH 8.3 whereby the net surface charge was zero.

IONP synthesized by reverse precipitation has smaller hydrodynamic size compare to IONP synthesized by normal precipitation. Aono et al. (2005) reported that normal precipitation would cause an increase in the mean crystallite and particle size. Kim et al. (2001) on the other hand suggested at pH 1-4 of  $\text{Fe}^{3+}$ ,  $\text{FeOOH}$  would be formed and

$\text{Fe}_3\text{O}_4$  would be precipitated at pH 9 to 14. In this case, titration of iron salt into basic pH could reduce the formation of  $\text{FeOOH}$ . Besides that, distribution of IONP synthesized by reverse precipitation is tend to right with the peak at 60 nm while distribution of IONP synthesised by normal precipitation is skewed to right with the peak at 70 nm as shown in Figure 4.5(a)(iii). However, IONP synthesized by normal precipitation has privilege on PDI. It gives smaller PDI (0.389) than IONP synthesized by reverse precipitation (0.463). Distribution of IONP synthesized by normal precipitation is narrower than IONP synthesized by reverse precipitation, leading to uniform particle size. Both synthesized approach considered as polydispersity as their PDI were higher than 0.2 (Serna et al., 2001). Zeta potential has been used to determine the surface charge of IONP. It recorded that, the zeta potential of IONP synthesized by reverse and normal precipitation were -60.4 and -54.3 mV, respectively which covered by negative surface charge on their surface.

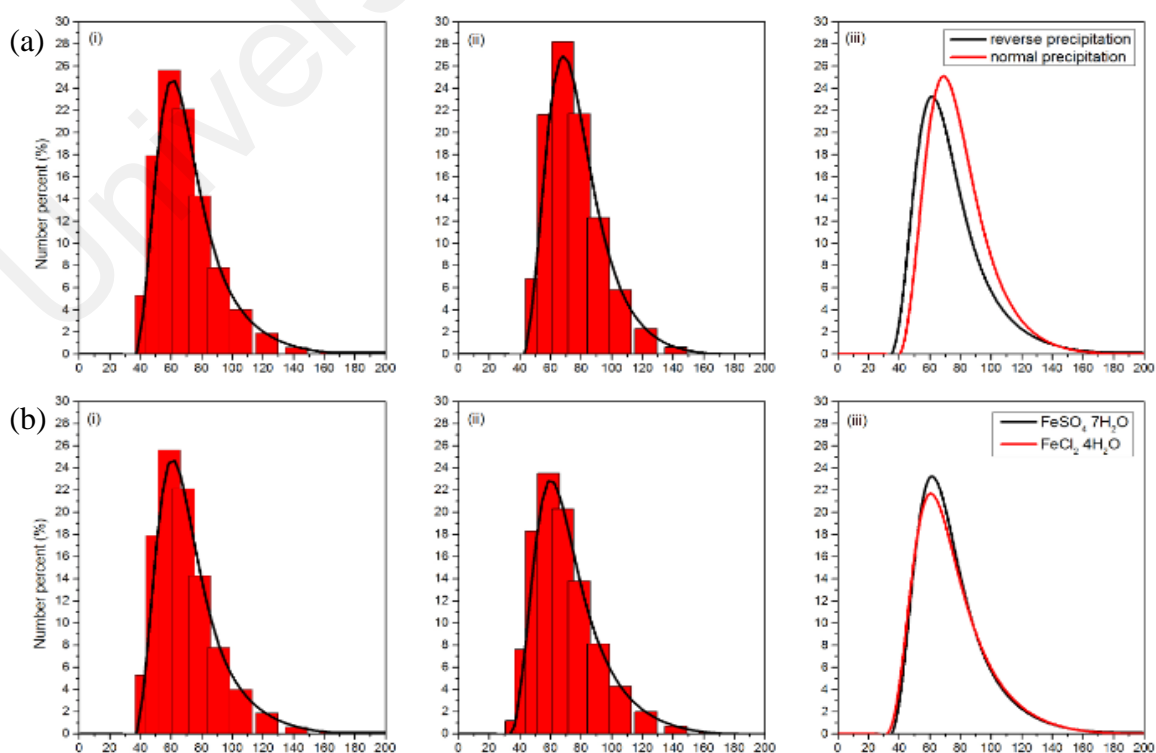
Hydrodynamic size of  $\text{FeSO}_4 \cdot 7\text{H}_2\text{O}$  sample (68.6 nm) was slightly higher than  $\text{FeCl}_2 \cdot 4\text{H}_2\text{O}$  sample (67.3 nm). However, PDI of  $\text{FeCl}_2 \cdot 4\text{H}_2\text{O}$  sample was slightly higher than  $\text{FeSO}_4 \cdot 7\text{H}_2\text{O}$  sample which has the same agreement with Figure 4.5(b)(iii). This phenomenon explained by more homogenous size uniformity and distribution of  $\text{FeSO}_4 \cdot 7\text{H}_2\text{O}$  sample.

Hydrodynamic sizes of IONP synthesized by pour once method was larger than IONP synthesized by drop wise method. Besides the smaller hydrodynamic size of IONP synthesized by drop wise method, it also gives a lower PDI as presented in Figure 4.5(c)(iii). It is observed that narrower hydrodynamic size distribution of IONP synthesized by drop wise method is due to better size uniformity. Furthermore, the peak of IONP synthesized by drop wise method is lower as compared to the peak synthesized by pour once methods. This consequently indicated that the drop wise method synthesizes smaller IONP.

For aging time parameter, average hydrodynamic size of IONP synthesized at 1.5 hrs aging time have the smallest particle size as compared to IONP synthesized at 1, 1.25, 1.75 and 2 hrs aging time. Increasing of the aging time from 1 hr to 1.5 hrs tended to decrease the hydrodynamic size of IONP. However, the hydrodynamic size increased once aging time was increased from aging time 1.5 to 2 hrs. Between 1 to 1.5 hrs of aging time, small nanoparticles on the surface of IONP dissolved due to Oswald ripening, leading to reducing hydrodynamic size of IONP (Jiang, Wang, Fu, & Liu, 2010). After 1.5 hrs aging time, re-deposition and accretion of small nanoparticles on IONP contributed to larger hydrodynamic size (Baumgartner et al., 2013). Particle size of IONP was further analysed by HRTEM analysis to attain realisable results. In this parameter, PDI was found to have the same trend as hydrodynamic size as the aging time was increased from 1 to 2 hrs. IONP synthesized at 1.5 hrs has the smallest PDI as indicated in Table 4.4. Thus, it has better size uniformity than IONP synthesized at 1, 1.25, 1.75 and 2 hrs aging time.

Table 4.4: Average hydrodynamic size, polydispersity index and zeta potential of IONP

	Average hydrodynamic size (nm)	Polydispersity index, PDI	Zeta Potential (mV)
<b><i>Synthesis approach</i></b>			
Reverse precipitation	68.6	0.463	-60.4
Normal precipitation	74.2	0.389	-54.3
<b><i>Precursor selection</i></b>			
FeSO <sub>4</sub> 7H <sub>2</sub> O	68.6	0.463	-60.4
FeCl <sub>2</sub> 4H <sub>2</sub> O	67.3	0.481	-46.9
<b><i>Addition method</i></b>			
Pour once	68.6	0.463	-60.4
Dropwise	59.5	0.201	-56.6
<b><i>Aging time</i></b>			
1.0 hr	68.6	0.463	-60.4
1.25 hrs	69.7	0.353	-43.4
1.5 hrs	65.4	0.237	-49.0
1.75 hrs	71.3	0.245	-47.0
2.0 hrs	78.9	0.252	-43.1



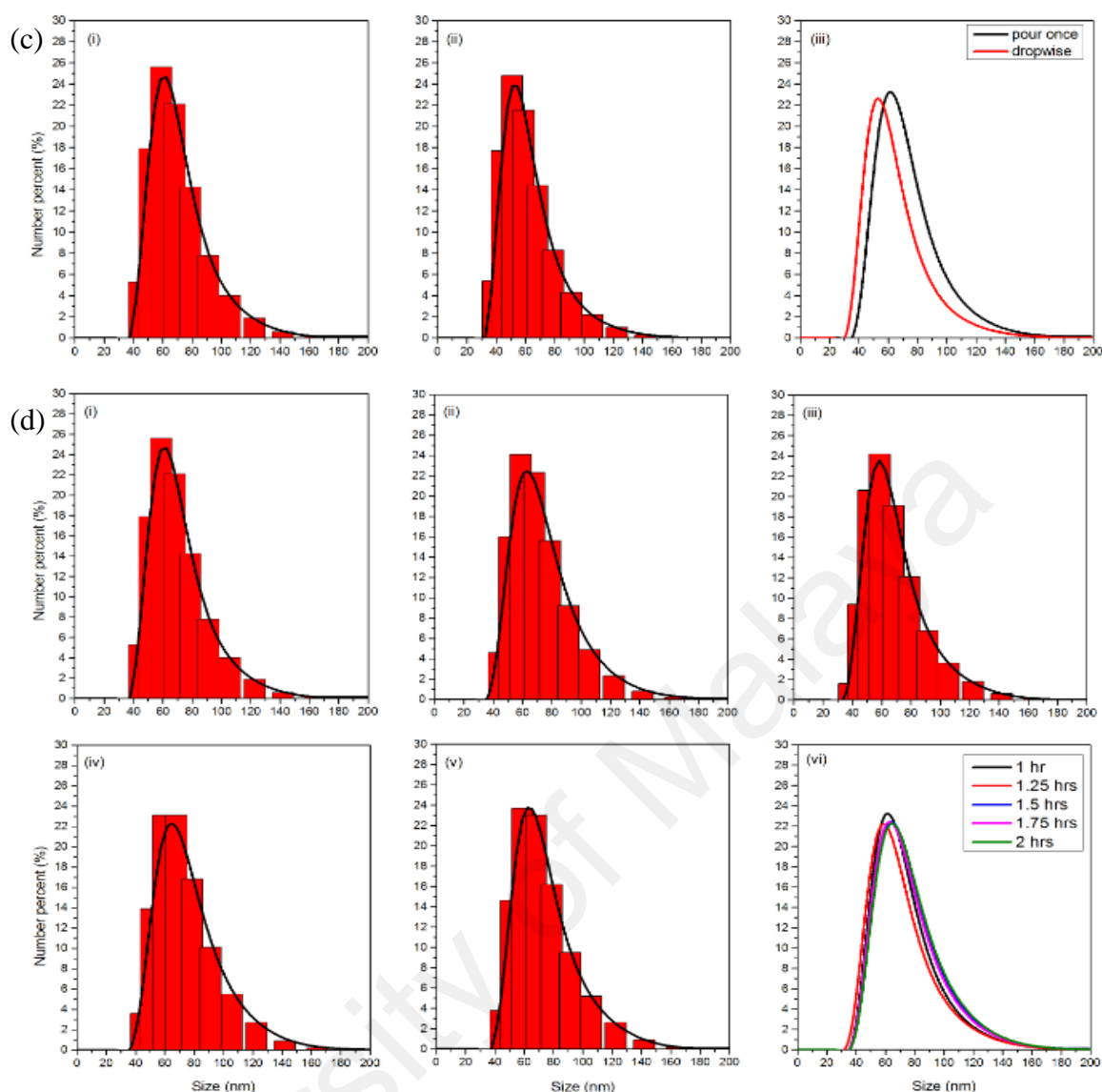


Figure 4.5: Hydrodynamic size distribution of IONP for the:  
 (a) Synthesis approach (i) reverse precipitation (ii) normal precipitation  
 (b) Precursor selection (i)  $\text{FeSO}_4 \cdot 7\text{H}_2\text{O}$  (ii)  $\text{FeCl}_2 \cdot 4\text{H}_2\text{O}$   
 (c) Addition method (i) pour once (ii) dropwise  
 (d) Aging time (i) 1 hr (ii) 1.25 hrs (iii) 1.5 hrs (iv) 1.75 hrs (v) 2 hrs

#### 4.1.5 HRTEM analysis

Morphological properties including particle size, features and shape of IONP with various synthesis parameters are tabulated in Table 4.5, and HRTEM analyses of IONP are illustrated in Figure 4.6. In general, the IONP achieved the particle size less than 50 nm having morphology of semi-spherical, cubic and needle shape. Needle shape of IONP was demonstrated as goethite (Powell et al. (2011)). Meanwhile semi-spherical and cubic shape of IONP indicated magnetite and maghemite (PETERNELE et al., 2014).



Agglomeration of IONP can be observed due to the nature of IONP which consist of van der Waals forces and magnetic dipolar forces among the particles.

In Figure 4.6(a)(i), it can be seen that IONP were slightly agglomerated with few needle shape IONP whilst Figure 4.6(a)(iii) illustrated higher agglomeration and needle shape of IONP. The images were clearer when it was zoomed to 120000 times magnification (Figure 4.6(a)(ii) and (iv)). Therefore, it can be concluded that IONP synthesized by normal precipitation obtained higher goethite than IONP synthesized by reverse precipitation. According to Strangway et al. (1968), goethite does not have magnetization, thus it does not contribute to magnetic properties in IONP. IONP synthesized by normal precipitation [Figure 4.6(a)(iii)] tended to form an agglomerated structure. This is attributed to the existence of goethite which has high tendency to form aggregated nanograins (Brok et al., 2014). Two normal distribution curves were observed in Figure 4.6(a)(ii) while only single normal distribution curve can be seen in Figure 4.6(a)(iv). From previous discussion, PDI of IONP synthesized by reverse precipitation was higher than IONP synthesized by normal distribution. Hence, Figure 4.5(a)(ii) was well agreement with the PDI due to non-uniformity factor of IONP.. However, average particle size of IONP synthesized by reverse precipitation ( $38.166 \pm 13.61$  nm) was smaller as compared to IONP synthesized by normal precipitation ( $48.235 \pm 9.64$  nm). It is anticipated that IONP with smaller particle size has an advantage in term of high surface area to volume ratio, leading to high surface interaction of IONP to NBR latex.

$\text{FeSO}_4 \cdot 7\text{H}_2\text{O}$  and  $\text{FeCl}_2 \cdot 4\text{H}_2\text{O}$  samples were analysed by HRTEM and compared as well. In Figure 4.6(b)(i), it can be seen that IONP were slightly agglomerated with a few needle shape IONP. Meanwhile, Figure 4.6(b)(iii) illustrated higher agglomeration and needle shape of IONP. Hence, it is proven that higher goethite leads to higher agglomeration. High agglomeration of IONP has the disadvantage of dispersing in NBR

latex, leading to bigger particle size and uneven distribution in NBR latex. In order to reduce formation of agglomerated particle,  $\text{FeSO}_4 \cdot 7\text{H}_2\text{O}$  sample ( $38.166 \pm 13.61 \text{ nm}$ ) was chosen despite its particle size was slightly greater than  $\text{FeCl}_2 \cdot 4\text{H}_2\text{O}$  sample ( $36.819 \pm 12.82 \text{ nm}$ ). Nucleation and growth of IONP were influenced by the release and usage rate of  $\text{SO}_4^{2-}$ ,  $\text{Cl}^-$  and  $\text{NH}_4^+$  as well as other intermediate products such as ferrous hydroxide ( $\text{Fe}(\text{OH})_2$ ) and goethite (Tajabadi & Khosroshahi, 2012).  $\text{FeSO}_4 \cdot 7\text{H}_2\text{O}$  particle with greater size was attributed to the contribution of anion  $\text{SO}_4^{2-}$  in growing particle size (Iwasaki et al., 2010). Ferrous hydroxide ( $\text{Fe}(\text{OH})_2$ ) was formed attributed to  $\text{FeSO}_4 \cdot 7\text{H}_2\text{O}$  and some of  $\text{Fe}(\text{OH})_2$  oxidized to goethite. Subsequently, combination of  $\text{Fe}(\text{OH})_2$  and goethite leading to magnetite formation and further growing the particle size.

Figure 4.6(c)(i) consisted of semi-spherical, cubic and needle shape of IONP meanwhile Figure 4.6(c)(iii) consisted of smaller semi-spherical and cubic structure of IONP. Through Figure 4.6(c)(iii), it can be confirmed that no goethite appeared in the IONP via HRTEM analysis. IONPs synthesized by pour once and dropwise with greater magnification are presented in Figure 4.6(c)(ii) and (iv), respectively. IONP synthesized by pour once method was bigger than IONP synthesized by drop wise method. In drop wise method, magnetite nucleus started to form when iron salt solution was added into ammonium hydroxide ( $\text{NH}_4\text{OH}$ ) but the growth of magnetite nucleus was confined by  $\text{NH}_4\text{OH}$  (Yu et al., 2007). Hence, growth rate of magnetite formation was slower than nucleation rate, leading to smaller size of IONP synthesized by drop wise method. Higher agglomeration of IONP synthesized by drop wise method can be seen in Figure 4.6(c)(iii). IONPs with small particle size and greater surface area to volume have better tendency to attract each other due to Van der Waals force and magnetic dipolar forces. In Figure 4.6(c)(ii) two peaks was observed but only one peak shifted to the left can be observed in Figure 4.6(c)(iv). Most of the IONP synthesized by drop wise size were in

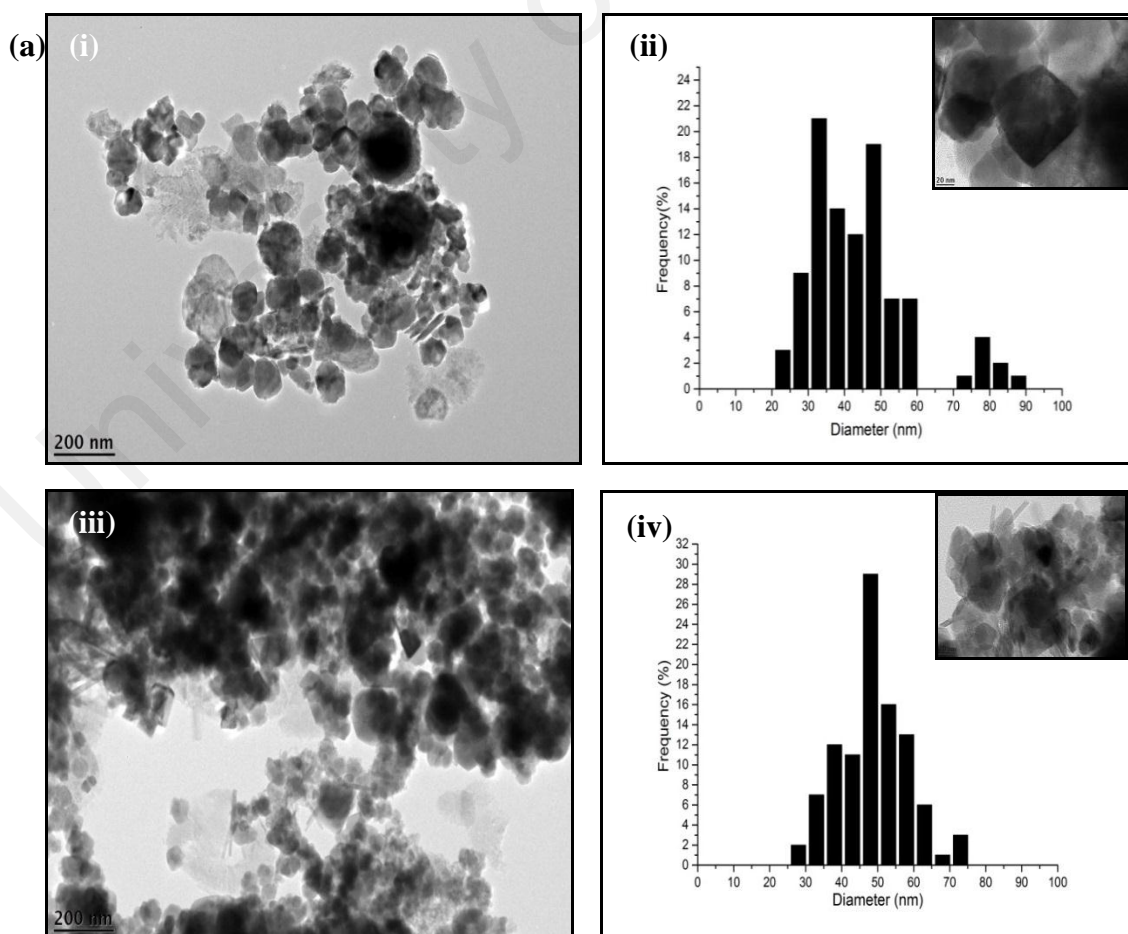
the range of 15 to 20 nm. The normal distributions as shown in these two figures are well in agreement with the PDI in Table 4.4

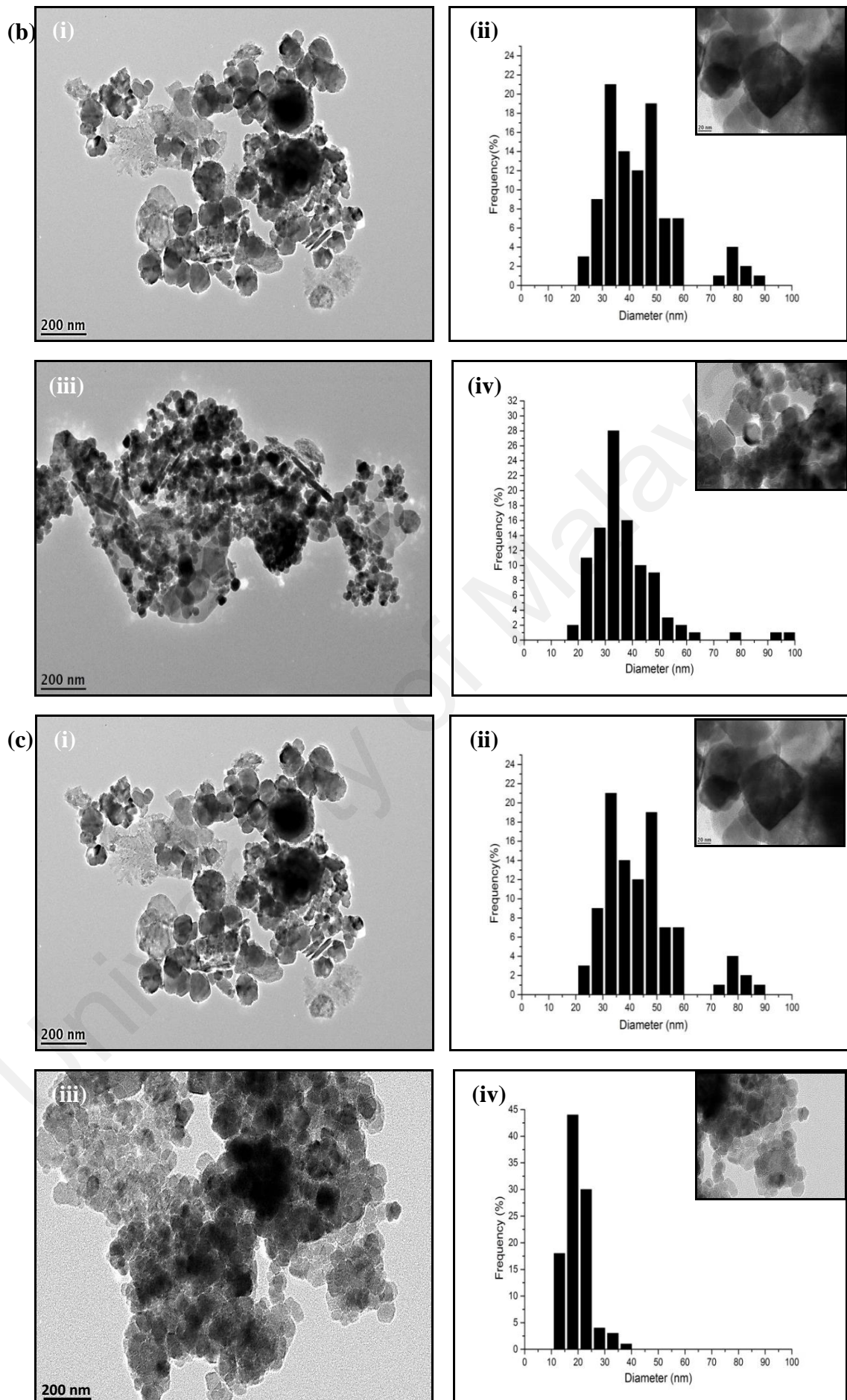
Figure 4.6(d)(i) shows lower degree of agglomeration with a few needle shape of IONP. Figure 4.6(d)(iii) consists of better dispersed of IONP without needle shape. Figure 4.6(d)(v) on the other hand shows highly agglomerated IONP with needle shape was observed. It proved that IONP with 1.5 hrs aging time has lower amount of goethite, and less agglomeration has occurred. High agglomeration of IONP synthesized at 1 hr aging time was attributed to existence of goethite which has high tendency to form aggregated nanograins (Brok et al., 2014). Series of IONP micrograph with 12000 magnification are shown in Figure 4.6(d)(i), (iii) and (v) . It could be seen that cubic shape of IONP in inset of Figure 4.6(d)(ii) was changing to semi spherical shape in inset of Figure 4.6(d)(iv) and (vi) due to prolonged aging effect. By increasing the aging time, the particle shape of IONP turns to spherical, showing a surface reorganization instead of nucleation event (Sciancalepore et al., 2015). Besides, the particle size of IONP (Figure 4.6(d)(iii) and (v)) were vividly smaller than the ones show in Figure 4.6(d)(i). Average particle size of IONP synthesized at 1, 1.5 and 2 hrs were identified at 38.166, 22.619 and 33.202 nm, respectively. Particle size of IONP is aligned with hydrodynamic size of IONP. In Figure 4.6(d)(ii) and (vi), bimodal normal distribution of average particle size of IONP was plotted while only Figure 4.6(d)(iv) shows monomodal normal distribution. This phenomenon can be explained by less agglomeration and monodispersed of IONP synthesized especially at 1.5 hrs of aging time.

Table 4.5: Particle size and shape of IONP with different synthesis parameter

	Size (nm)	Shape		
<i>Synthesis approach</i>		Cubic	Semi-sphere	Needle
Reverse precipitation	38.166 ± 13.61	A	A	A
Normal precipitation	48.235 ± 9.64	A	A	A
<i>Precursor selection</i>				
FeSO <sub>4</sub> 7H <sub>2</sub> O	38.166 ± 13.61	A	A	A
FeCl <sub>2</sub> 4H <sub>2</sub> O	36.819 ± 12.82	A	A	A
<i>Addition method</i>				
Pour once	38.166 ± 13.61	A	A	A
Dropwise	19.109 ± 4.57	A	A	NA
<i>Aging time</i>				
1.0 hr	38.166 ± 13.61	A	A	A
1.5 hrs	22.619 ± 7.94	A	A	NA
2.0 hrs	33.202 ± 12.36	A	A	NA

\*NA = not available, A = available







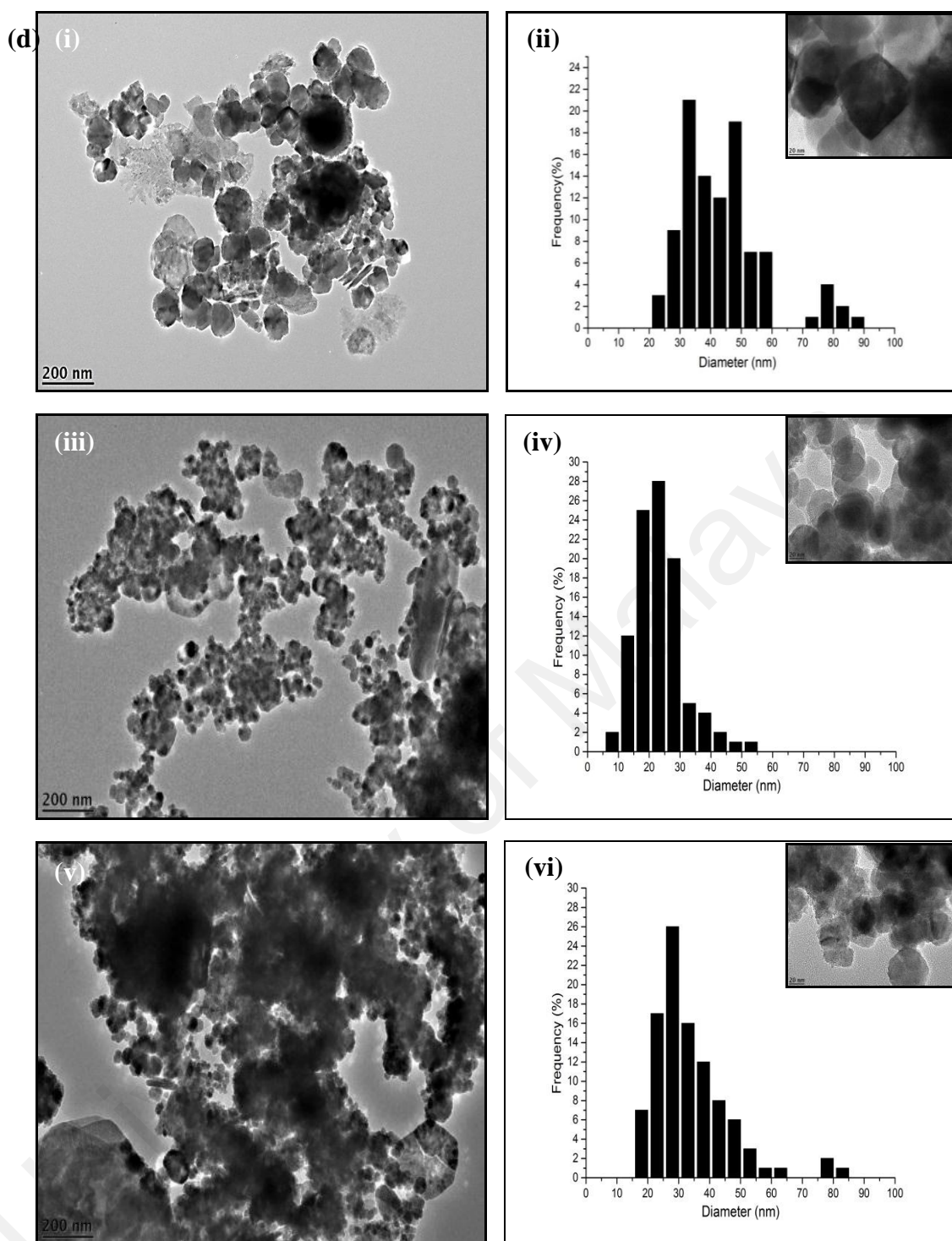


Figure 4.6: HRTEM image of IONP

- e) Synthesis approach (i) reverse precipitation at 15000 $\times$  magnification (ii) PSD of reverse precipitation with inset at 120000 $\times$  magnification (iii) normal precipitation at 15000 $\times$  magnification (iv) PSD of normal precipitation with inset at 120000 $\times$  magnification
- f) Precursor selection (i)  $\text{FeSO}_4 \cdot 7\text{H}_2\text{O}$  at 15000 $\times$  magnification (ii) PSD of  $\text{FeSO}_4 \cdot 7\text{H}_2\text{O}$  with inset at 120000 $\times$  magnification (iii)  $\text{FeCl}_2 \cdot 4\text{H}_2\text{O}$  at 15000 $\times$  magnification (iv) PSD of  $\text{FeCl}_2 \cdot 4\text{H}_2\text{O}$  with inset at 120000 $\times$  magnification
- g) Addition method (i) pour once at 15000 $\times$  magnification (ii) PSD of pour once with inset at 120000 $\times$  magnification (iii) dropwise at 15000 $\times$  magnification (iv) PSD of drop wise with inset at 120000 $\times$  magnification

- h) Aging time (i) 1 hr at 15000× magnification (ii) PSD of 1hr with inset at 120000× magnification (iii) 1.5 hrs at 15000× magnification (iv) PSD of 1.5 hrs with inset at 120000× magnification (v) 2 hrs at 15000× magnification (vi) PSD of 2 hrs with inset at 120000× magnification

#### 4.1.6 VSM analysis

Table 4.6 illustrates magnetization saturation ( $M_s$ ), coercivity ( $H_c$ ) and remanence ( $M_r$ ) of IONP in various synthesis parameters. The magnetization curve demonstrated accordingly and presented in Figure 4.7. In general,  $M_s$  of bulk magnetite is recorded at 92 emu/g (Men et al., 2012). However,  $M_s$  of IONP is smaller than bulk magnetite attributed to its nano-particle size. Overall  $H_c$  and  $M_r$  of IONP are lower than 110 G and 11 emu/g, respectively. Due to these advantages, IONP is chosen to incorporate with NBR latex. In Figure 4.7, it can be seen that magnetization curves did not intersected at zero point and it proved that IONP were not superparamagnetic material. It is obviously observed as well the present of hysteresis loop where by the domains of IONP do not return to their original orientation once applied field was reduced. For the literature, it generally found that the superparamagnetic IONP are usually smaller than 20 nm (Carvalho et al., 2013).

In synthesis approach parameter,  $M_s$  of produced IONP synthesized by reverse and normal precipitation is 68.11 and 64.07 emu/g at 10000 G.  $M_s$  of IONP synthesized by reverse precipitation was relatively strong compare to IONP synthesized by normal precipitation due to higher percentage of magnetite exist in IONP. Coercivity ( $H_c$ ) and remanence ( $M_r$ ) of IONP synthesized by reverse precipitation was relatively larger which are 93.61 emu/g and 9.74 G, respectively, compared to IONP synthesized by normal precipitation (70.03 emu/g and 6.23 G, respectively).  $H_c$  and  $M_r$  of IONP synthesized by normal precipitation were smaller attributed to low  $M_s$ .

Figure 4.7(b)(i) illustrates ferromagnetic hysteresis loop of  $\text{FeSO}_4 \cdot 7\text{H}_2\text{O}$  and  $\text{FeCl}_2 \cdot 4\text{H}_2\text{O}$  sample.  $M_s$  of  $\text{FeSO}_4 \cdot 7\text{H}_2\text{O}$  and  $\text{FeCl}_2 \cdot 4\text{H}_2\text{O}$  sample were 68.11 and 69.55 emu/g

at 10000 G, respectively. Furthermore,  $H_c$  and  $M_r$  of  $\text{FeSO}_4 \cdot 7\text{H}_2\text{O}$  sample were 93.61 G and 9.74 emu/g, respectively. However,  $H_c$  and  $M_r$  of  $\text{FeCl}_2 \cdot 4\text{H}_2\text{O}$  sample were slightly larger which were 109.66 G and 10.53 emu/g, respectively, as depicted in the Figure 4.7(b)(ii). From the result, it confirmed that no significant difference of  $M_s$ ,  $H_c$  and  $M_r$  in between  $\text{FeSO}_4 \cdot 7\text{H}_2\text{O}$  and  $\text{FeCl}_2 \cdot 4\text{H}_2\text{O}$  sample. Hence, it can be concluded that different precursor selection has no substantial impact on magnetic properties.

Figure 4.7(c)(i) and (ii) show that ferromagnetic hysteresis loop of IONP synthesized by pour once and drop wise method.  $M_s$ ,  $H_c$  and  $M_r$  of IONP synthesized by pour once and drop wise method were summarized in Table 4.6. It is shown,  $M_s$ ,  $H_c$  and  $M_r$  of IONP synthesized by pour once method was relatively larger than IONP synthesized by drop wise method attributed to higher percentage of magnetite and large crystallite size of IONP.  $M_s$  of IONP synthesized by pour once method was in good agreement with XRD, FTIR, Raman spectroscopy and HRTEM result. Dar and Shivashankar (2014) reported that magnetic properties of IONP were highly dependent on the size, morphology, content and methodology of the synthesis.

Figure 4.7(d)(i) illustrates magnetization curves of IONP synthesized at 1, 1.25, 1.5, 1.75 and 2 hrs aging time.  $M_s$  of IONP synthesized at 1, 1.25, 1.5, 1.75 and 2 hrs aging time were 68.11, 73.54, 77.17, 75.22 and 73.73 emu/g, respectively as shown in Table 4.6. Despite obtaining the smallest particle size of IONP synthesized at 1.5 hrs aging time, it also recorded the highest  $M_s$  attributed to contribution of high percentage of magnetite and maghemite presence. IONP with lower  $M_s$  recorded for the sample obtained at 1 and 1.25 hrs aging time despite the larger size was due to surface of IONP synthesized at 1 and 1.25 hrs composed of disordered spins. This could prevent the core spins from aligning in the same direction and thus reduce  $M_s$  of smaller crystallite size of IONP (El et al., 2012). In addition, present of unreacted goethite phase also reduce the  $M_s$ . After 1.5 hrs aging time,  $M_s$  of IONP synthesized at 1.75 and 2 hrs decreased as



indicated in Table 4.6. It was due to phase transformation of magnetite to maghemite and hematite whereby hematite was prominently increased after 1.5 hrs aging time (Table 4.1). Both coercivity and remanence have the same trend which increased from 1 to 1.5 hrs aging time, subsequently decreased once the aging time increased up to 2 hrs. In this condition,  $M_r$  and  $H_c$  can be related to spin-glass transition. Prior to 1.5 hrs aging time, static magnetic moments on the surface of IONP that consist of anisotropy surface were contributed to increase of  $H_c$ . After 1.5 hrs aging time, lessening of superficial anisotropy surface due to spin-glass broken, results in coercivity dropping abruptly.

Table 4.6: Magnetic properties of IONP with different synthesis parameter

	Coercivity, $H_c$ (G)	Remanence, $M_r$ (emu/g)	Magnetization saturation, $M_s$ (emu/g)
<b><i>Synthesis approach</i></b>			
Reverse precipitation	93.61	9.74	68.11
Normal precipitation	70.03	6.23	64.07
<b><i>Precursor selection</i></b>			
FeSO <sub>4</sub> 7H <sub>2</sub> O	93.61	9.74	68.11
FeCl <sub>2</sub> 4H <sub>2</sub> O	109.66	10.53	69.55
<b><i>Addition method</i></b>			
Pour once	93.61	9.74	68.11
Dropwise	72.91	5.00	44.69
<b><i>Aging time</i></b>			
1.0 hr	93.61	9.74	68.11
1.25 hrs	94.71	9.13	73.54
1.5 hrs	99.97	9.58	77.17
1.75 hrs	72.73	7.56	75.22
2.0 hrs	50.14	7.26	73.73

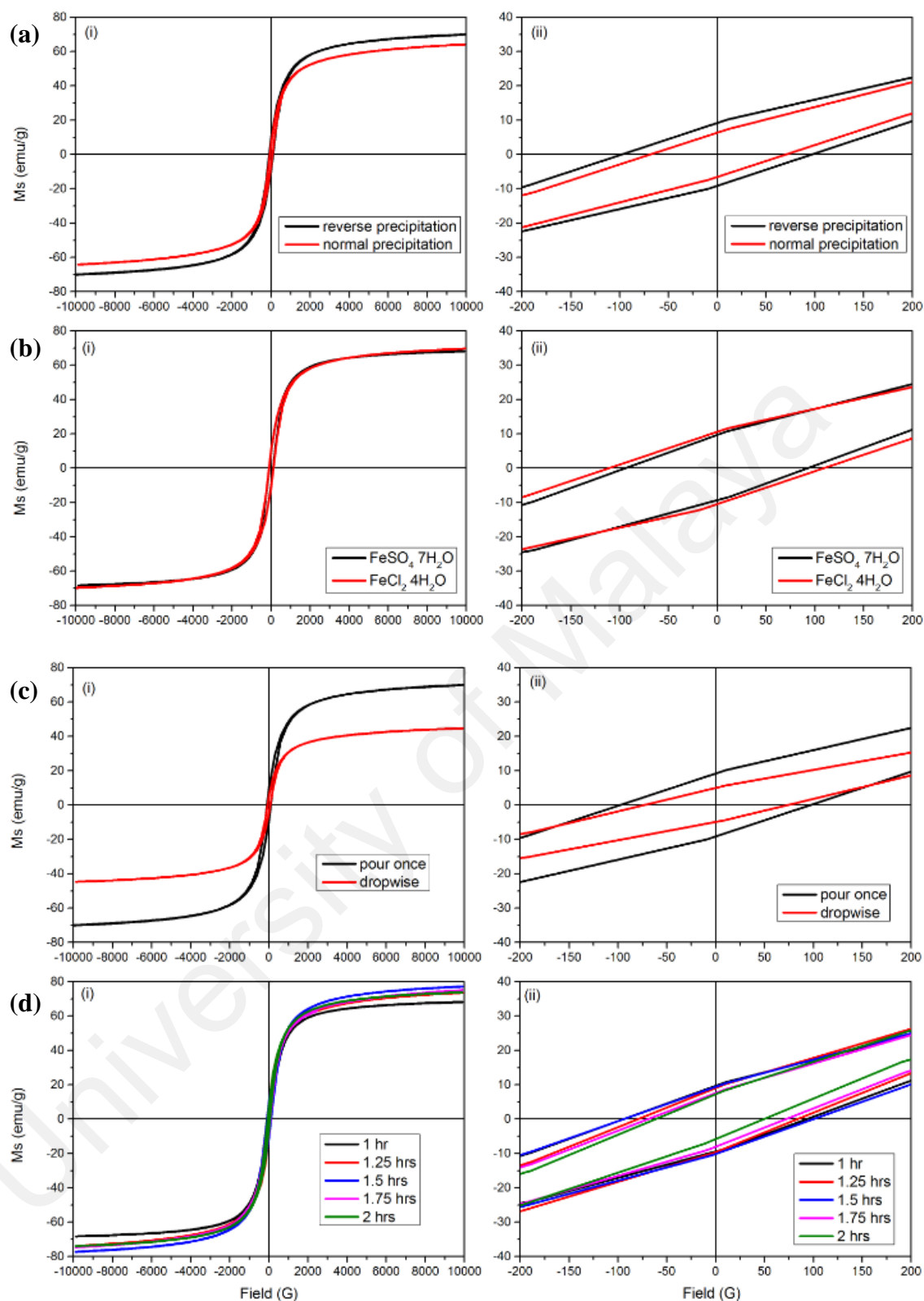


Figure 4.7: Magnetization curve of IONP via (a) synthesis approach, (b) precursor selection, (c) addition method and (d) aging time

It can be concluded that optimized aging time was 1.5 hrs to synthesize IONP. It is because it consisted of low agglomeration IONP, smallest particle size and highest magnetization saturation. These properties of IONP are very important to compound

and form NBR/IONP composite. Throughout all the parameters,  $\text{FeSO}_4 \cdot 7\text{H}_2\text{O}$  as precursor with pour once addition method and 1.5 hrs aging in reverse precipitation were determined as optimized IONP synthesized in the study.

## **4.2 Synthesis of coated IONP (C-IONP)**

From the optimum synthesis parameters of IONP, the surface properties of IONP will be further modified through thin coating layer. An optimization of C-IONP will be based on different type of coating agent, concentration of coating agents and ultrasonication time of C-IONP.

### **4.2.1 Particle size and zeta potential analysis**

The particle size and surface charge all series of C-IONP is studied through the particle size and zeta potential analysis. Table 4.7 illustrates hydrodynamic size, PDI and zeta potential of C-IONP and its corresponding hydrodynamic size distribution is shown in Figure 4.8. In general, all C-IONP consist of monomodal normal distribution and asymmetric which is similar to IONP. C-IONP formed has average hydrodynamic size with less than 100 nm. This indicated that, with coating layer, the particle size of C-IONP is still within nano range.

In various coating agent parameters, capric acid C-IONP has the lowest hydrodynamic size and, the hydrodynamic size ascend from oleic acid, palmitic acid, myristic acid to stearic acid as shown in Table 4.7. Oleic acid C-IONP on the other hand has the smallest PDI (0.154) and the ascending order was capric acid, palmitic acid, stearic acid and myristic acid. Capric acid C-IONP obtained the smallest hydrodynamic size but its PDI is larger than oleic acid C-IONP. Besides, it was observed that zeta potential of capric acid C-IONP (-38.3 mV) is lower than uncoated IONP (-49.0 mV). Generally, C-IONP has higher zeta potential than IONP (Shete et al., 2015). Lower zeta potential of capric acid C-IONP might be due to inhomogeneity coating of capric acid on IONP.

Besides, it was noticed that two peaks can be observed in Figure 4.8(a)(ii), (iii) and (v). It brought by the inhomogeneity coating layer of capric acid, myristic acid, and stearic acid on IONP, which consequently resulted in uneven hydrodynamic size of C-IONP. In comparison with single peak in Figure 4.8(a)(i), small PDI and average hydrodynamic size of oleic acid C-IONP contributed from the its homogenous layer coating agent among the others.

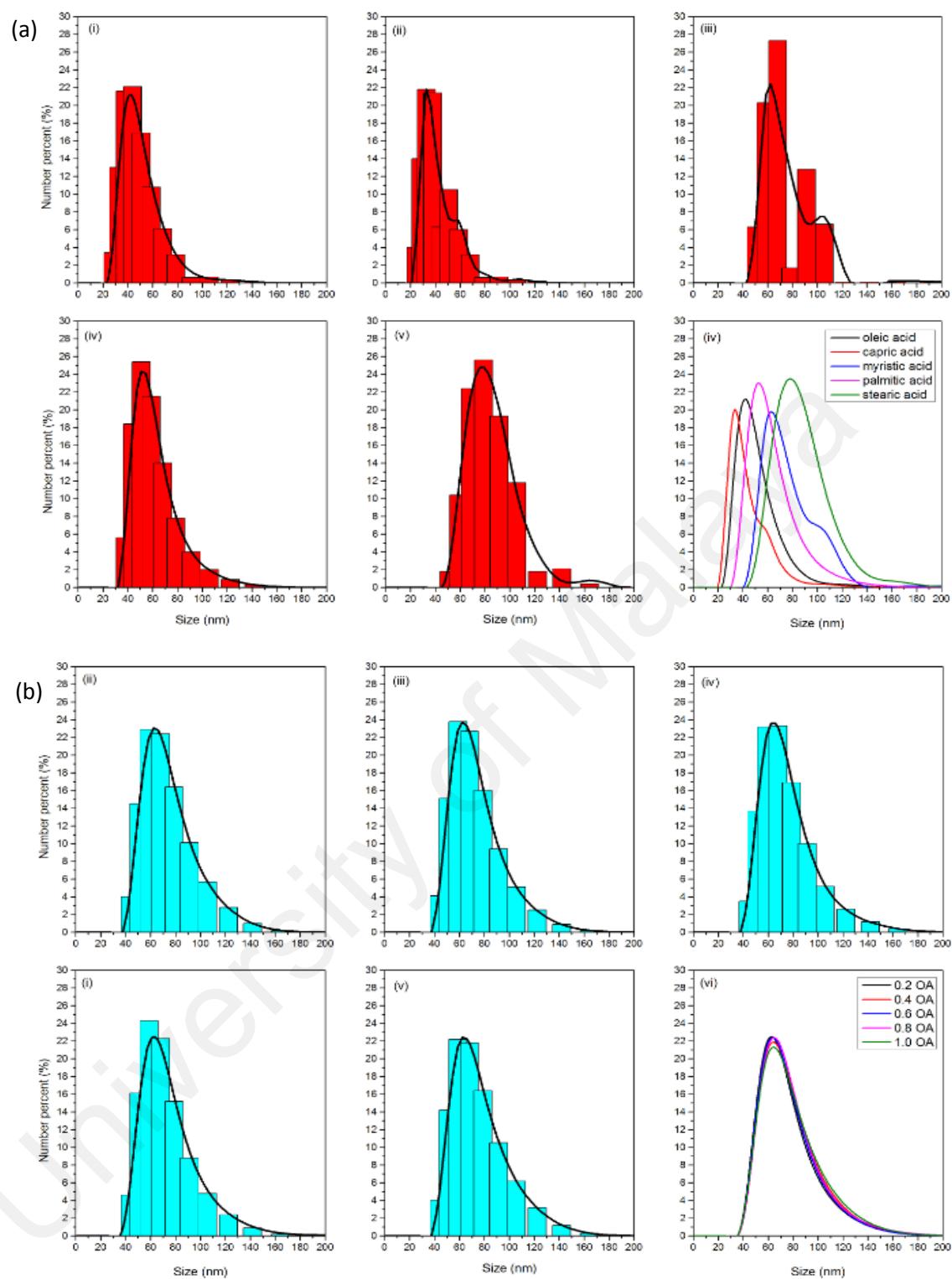
Subsequently, oleic acid C-IONP was optimized with different loading ratio of 0.2, 0.4, 0.6, 0.8 and 1.0 oleic acid to IONP. It was observed that hydrodynamic size of oleic acid C-IONP was decreased from 70.33 to 57.58 nm as the oleic acid loading was increased from 0.2 to 0.6 OA. Furthermore, the particle size, increased back to 72.25 nm once oleic acid loading reached to 1.0 OA. It can be said that, size of IONP was dependent on the loading of oleic acid. Larger hydrodynamic size of 0.2 and 0.4 OA was due to insufficient amount of oleic acid to encapsulate IONP, leading to difficulty of IONP to separate during ultra-sonication. Thus, IONPs with larger hydrodynamic size of 0.2 (70.33 nm) and 0.4 OA (71.35 nm) as compared to 0.6 OA (57.58 nm) is subsequently produced. Once the concentration of oleic acid was increased to 0.8 and 1.0 OA, hydrodynamic size were getting larger owing to long chain of oleic acid clinging on each other as indicated in Figure 4.9. PDI of oleic C-IONP has similar trend as hydrodynamic size from 0.2 to 1.0 OA. The 0.6 OA has the lowest PDI (0.183), thus supporting that it is possible to obtain uniform size with 0.6 loading ratio. It is postulated that the saturation covalent bonding forming in between oleic acid and IONP is as indicated in Figure 4.10.

Other than that, optimization of oleic acid with various ultra-sonication times have shown that hydrodynamic size and PDI increases (Table 4.7) with increase in the sonication time from 15 to 30 mins. These values were slightly dropped to 62.28 nm and 0.127 at 60 mins, respectively. Once ultra-sonication time was increased to 120

mins hydrodynamic size was increased tremendously to 75.92 nm and PDI was 0.262. From the result, it is predicted that saturation covalent bonding between IONP and oleic acid was formed at 60 mins sonication time.

Table 4.7.: Hydrodynamic size, polydispersity index and zeta potential of C-IONP

	Average hydrodynamic size (nm)	Polydispersity index (PDI)	Zeta Potential (mV)
<b><i>Various coating agent</i></b>			
Oleic acid	47.50	0.154	-57.5
Capric acid	40.84	0.242	-38.3
Myristic acid	77.11	0.427	-53.5
Palmitic acid	58.91	0.320	-53.1
Stearic acid	83.96	0.331	-52.9
<b><i>Oleic acid loading</i></b>			
0.2 OA	70.33	0.367	-48.6
0.4 OA	71.35	0.250	-52.2
0.6 OA	57.58	0.183	-58.7
0.8OA	70.45	0.224	-55.1
1.0 OA	72.25	0.213	-75.6
<b><i>Ultra-sonication time</i></b>			
15 mins	57.58	0.172	-53.7
30 mins	62.61	0.328	-51.5
60 mins	62.28	0.127	-79.2
90 mins	69.63	0.310	-89.0
120 mins	75.92	0.262	-95.4



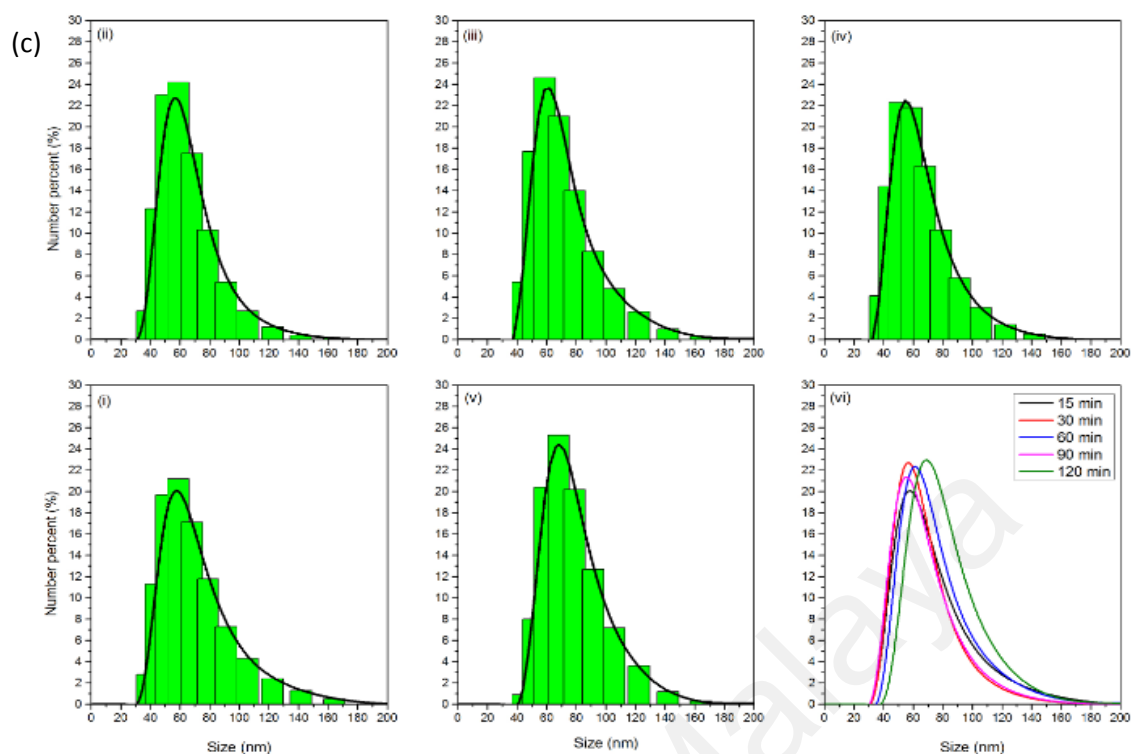


Figure 4.8: Hydrodynamic size distribution of C-IONP for the:

(a) Various coating agent (i) oleic acid (ii) capric acid (iii) myristic acid (iv) palmitic acid (v) stearic acid

(b) Oleic acid loading (i) 0.2 OA (ii) 0.4 OA (iii) 0.6 OA (iv) 0.8 OA (v) 1.0 OA

(c) Ultra-sonication time (i) 15 mins (ii) 30 mins (iii) 60 mins (iv) 90 mins (v) 120 mins

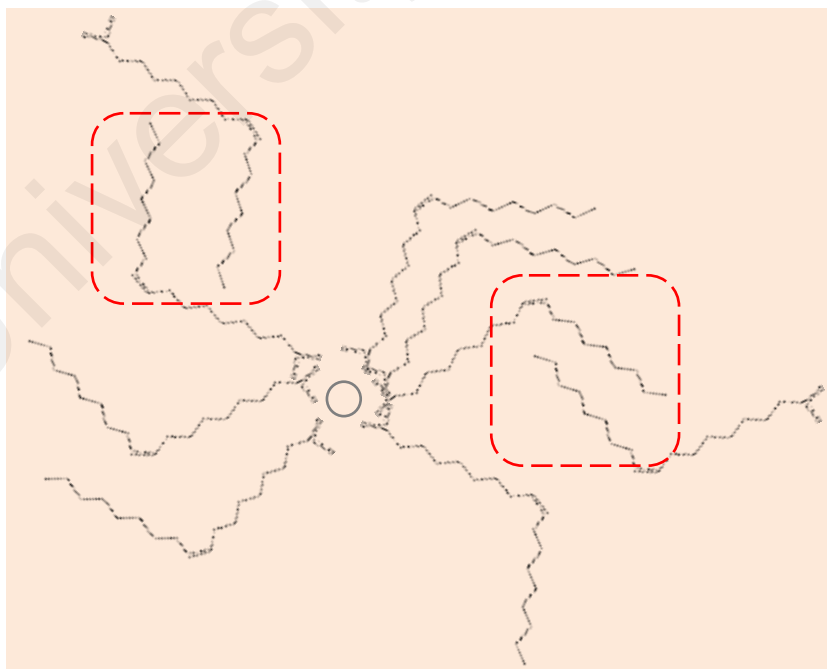


Figure 4.9: Interaction in between oleic acid chain

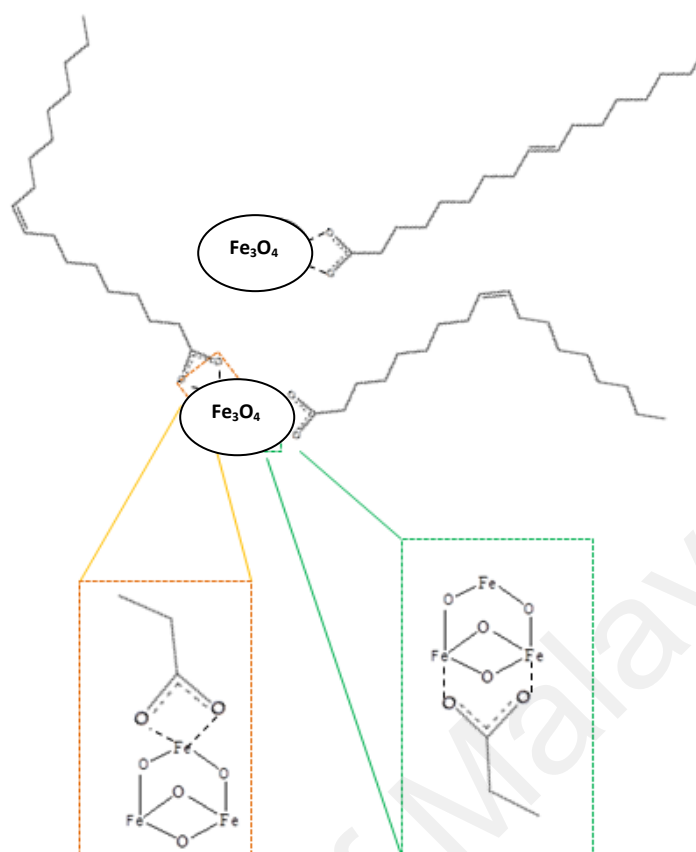


Figure 4.10: Interaction between IONP and oleic acid

#### 4.2.2 TGA analysis

The compositions of coating layers on C-IONP were recorded based on its thermal degradation behaviour. The analysed results of TGA of C-IONP were summarized in Table 4.8. Mass loss of C-IONP on the other hand was illustrated in Figure 4.11. TGA curves show that a slight mass loss ranging from 0.93 to 2.02 % in the temperature range of 80 - 150 °C attributed to moisture content in C-IONP samples. Further heating led to decomposition of coating agent up to 34.85 % in the temperature range of 160 – 450 °C. Concurrently, phase transformation of magnetite to maghemite occurred within the same temperature range. However the associated mass loss was not observed as it was camouflaged by dominated mass loss of coating agent (García-Jimeno & Estelrich, 2013). Insignificant mass loss on the respective temperature range was lesser than 8.00 % can be observed in between 450 and 800 °C owing to phase transformation of



maghemite to hematite. Coating agent to IONP ratio was calculated with assumption of negligible mass loss of magnetite to maghemite phase transformation as shown in Equation 4.1.

$$\text{Coating agent to IONP ratio} = \frac{\text{coating agent}}{\text{phase transformation} + \text{residue}} \quad \text{Equation 4.1}$$

Oleic acid C-IONP appears to have the lowest coating agent to IONP ratio, which is 0.08. Comparatively, other coating agents have higher coating agent to IONP ratio as indicated in Table 4.8. Low coating agent to IONP ratio of oleic acid sample was attributed to presence of double bond in fatty acid chain. Double bond of oleic acid allowed it to bend and subsequently encapsulate the IONP as shown in Figure 4.9. It allowed small amount of oleic acid to penetrate and bind with IONP. Furthermore, interaction of double bond between oleic acids could assist in the formation of densely packed layer on IONP surface (Faraji, Yamini, & Rezaee, 2010). However, capric acid, myristic acid, palmitic acid and stearic acid that is linear with unbendable backbone had higher coating agent to IONP ratio. They have a tendency to bind with IONP with no obstacles as indicated in Figure 4.12. Therefore, ultra-sonication was carried out to improve the interaction of oleic acid with IONP.

In oleic acid parameters, the amount of coating agent to IONP ratio increases dramatically from 0.2 to 0.6 OA (from 0.14 to 0.492), and increases slowly to 0.516 (0.8 OA) and 0.552 (1.0 OA). It can be said that 0.492 of oleic acid to IONP ratio was the saturation of single layer oleic acid. It expected that, the secondary layer will tend to form with greater concentration of oleic acid.

Besides that, in ultra-sonication time parameter, coating agent to IONP ratio was found to increase fast from 15 to 60 mins and increase slowly (increment of approximately 0.2) from 60 to 120 mins as depicted in Table 5.8. The 0.6 OA and 60 mins of ultra-

sonication time were the equilibrium state of single layer oleic acid. Ultra-sonication on the other hand was able to improve the reaction in between IONP and oleic acid. It was suggested that 60 mins ultra-sonication was able to achieve 0.451 ratio that limits the coating process oleic acid on IONP in rapid rate instead of 24 hours. This would definitely shorten the overall time of C-IONP synthesis.

Table 4.8: Residue, percentage of coating agent and coating agent to IONP ratio of C-IONP

	Residue (%)	Moisture (%)	Coating agent (%)	Phase transforma tion (%)	Coating agent to IONP ratio
<b><i>Various coating agent</i></b>					
Oleic acid	83.75	0.93	7.32	8.00	0.080
Capric acid	71.12	2.63	23.44	2.81	0.317
Myristic acid	64.69	1.40	30.61	3.30	0.450
Palmitic acid	84.39	0.57	13.17	1.87	0.153
Stearic acid	67.49	1.17	26.58	4.76	0.368
<b><i>Oleic acid loading</i></b>					
0.2 OA	78.95	0.99	12.14	7.92	0.140
0.4 OA	74.02	1.60	21.61	2.77	0.281
0.6 OA	59.10	1.84	32.37	6.69	0.492
0.8OA	58.90	1.79	33.41	5.90	0.516
1.0 OA	58.10	2.02	34.85	5.03	0.552
<b><i>Ultra-sonication time</i></b>					
15 mins	69.69	1.90	26.13	2.28	0.363
30 mins	66.43	1.53	28.72	3.32	0.412
60 mins	59.40	1.63	30.57	8.40	0.451
90 mins	63.73	1.37	31.68	3.22	0.473
120 mins	59.67	1.43	32.58	6.32	0.493

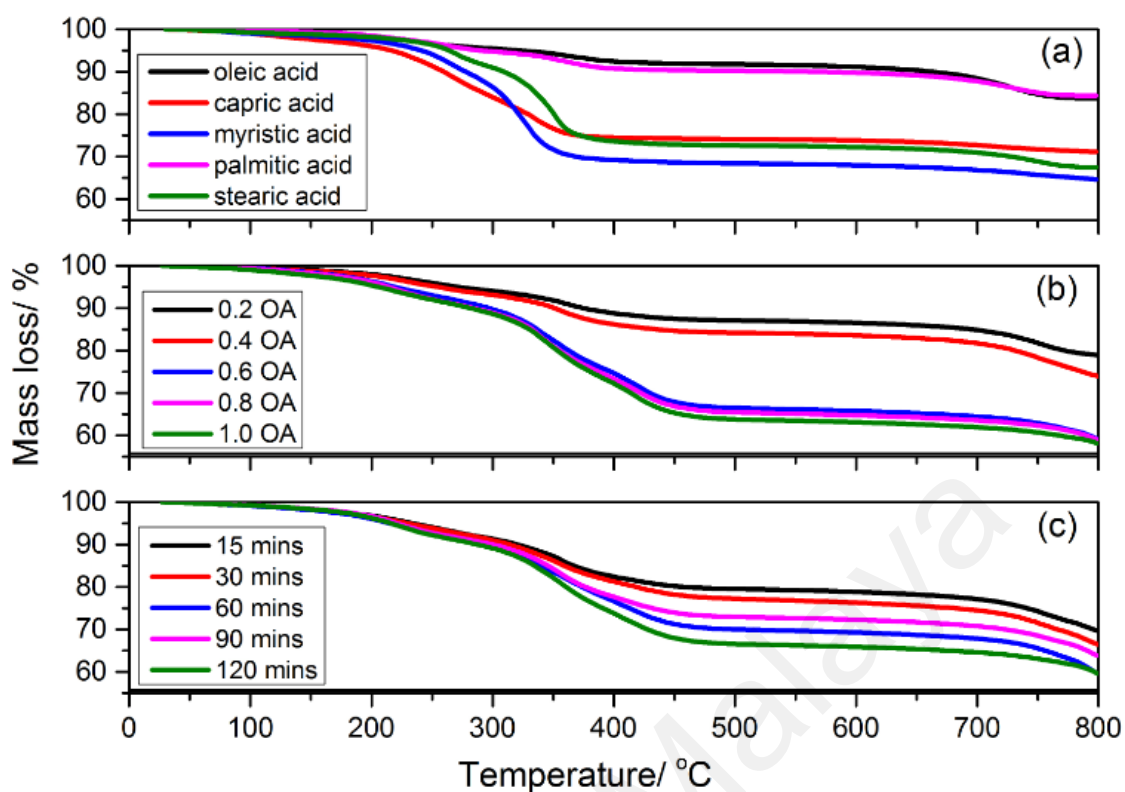


Figure 4.11: TGA analysis of C-IONP

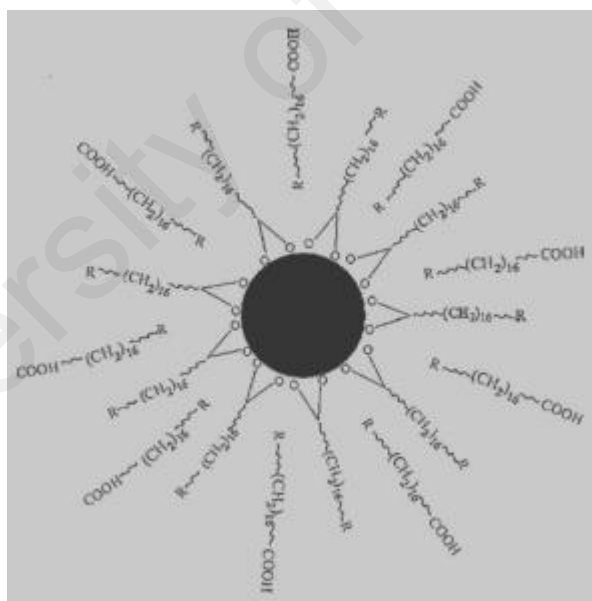


Figure 4.12: Interaction in between saturated fatty acid chain (Gogoi et al., 2012)

### 4.2.3 FTIR analysis

The interaction and interface between coating layers and IONP is analysed by the formation of functional groups derived from FTIR analysis. The wavenumber of IONP, fatty acid and interaction in between IONP and fatty acid band were illustrated in Table

4.9. Meanwhile, COOH groups and IONP sites interaction as well as the presence of C=O bands were indicated in Table 4.10. Figure 4.13 shows the spectra of C-IONP samples. All FTIR spectra shows 1521 and 1405  $\text{cm}^{-1}$ , indicating interaction of IONP and fatty acid existed.  $\Delta \nu_{\text{as}} - \nu_{\text{s}}$  in Table 4.10 shows in the range of 100-120  $\text{cm}^{-1}$  which corresponds to chelating bidentate interaction (Liang et al., 2014). It indicates that two O atoms of carboxylate group were equivalently bonded to Fe as shown in Figure 4.10 and 4.12.

In Table 4.10, none of the samples in various coating agent parameter consists of C=O band, and it proves that single layer coated structures on the surface of IONP. In oleic acid parameter, 0.8 OA and 1.0 OA of consist of C=O bands at 1708.38 and 1708.32  $\text{cm}^{-1}$ , respectively. Similarly, 90 and 120 mins ultra-sonication time indicates at 1707.69 and 1710.98  $\text{cm}^{-1}$ , respectively. Existence of C=O band in FTIR suggested the characteristic of fatty acid which is physically attached to the primary layer of fatty acid. In fact, it was suggested in Figure 5.9 whereby the primary fatty acid layer was absorbed on IONP surface via covalent bonding while secondary fatty acid layer was physically attached due to hydrophobic interaction of fatty acid. This statement was supported by some researchers who had carried out the similar synthesis approach (Gyergyek, Makovec, & Drofenik, 2011; Ramimoghdam, Bagheri, & Hamid, 2015; Sahoo et al., 2001).

Table 4.9: FTIR major peaks assignment of C-IONP (Liang et al., 2014)

Band Assignments	Wavenumber (cm <sup>-1</sup> )
<i>Characteristic of IONP band</i>	
O-H vibration	1632
Fe-O lattice vibration	634, 565
<i>Characteristic of fatty acid band</i>	
Asymmetric and symmetric C-H stretching vibration	2923, 2854
C-C stretching vibration	1115
C-O stretching vibration	1048
C=O stretching vibration	1710
<i>Interaction of IONP and fatty acid</i>	
Asymmetric $\nu_{as}(\text{COO}^-)$ stretching vibration	1521
Symmetric $\nu_s(\text{COO}^-)$ stretching vibration	1405

Table 4.10: Interaction of carboxylate groups and IONP sites as well as presence of C=O band in C-IONP

	$\nu_{as}(\text{COO}^-)$ (cm <sup>-1</sup> )	$\nu_s(\text{COO}^-)$ (cm <sup>-1</sup> )	$\Delta \nu_{as} - \nu_s$ (cm <sup>-1</sup> )	C=O band (cm <sup>-1</sup> )
<i>Various coating agent</i>				
Oleic acid	1522.47	1421.82	100.65	NA
Capric acid	1532.32	1441.30	91.02	NA
Myristic acid	1536.70	1453.89	82.81	NA
Palmitic acid	1532.88	1453.52	79.36	NA
Stearic acid	1535.85	1455.27	80.58	NA
<i>Oleic acid loading</i>				
0.2 OA	1543.91	1425.77	118.14	NA
0.4 OA	1532.04	1426.32	105.72	NA
0.6 OA	1533.99	1425.89	108.10	NA
0.8OA	1544.35	1428.29	116.06	1708.38
1.0 OA	1534.76	1426.11	108.65	1708.32
<i>Ultra-sonication time</i>				
15 mins	1540.65	1433.51	107.14	NA
30 mins	1536.55	1428.64	107.91	NA
60 mins	1535.44	1429.66	105.78	NA
90 mins	1531.93	1430.92	101.01	1707.69
120 mins	1537.07	1428.84	108.23	1710.98

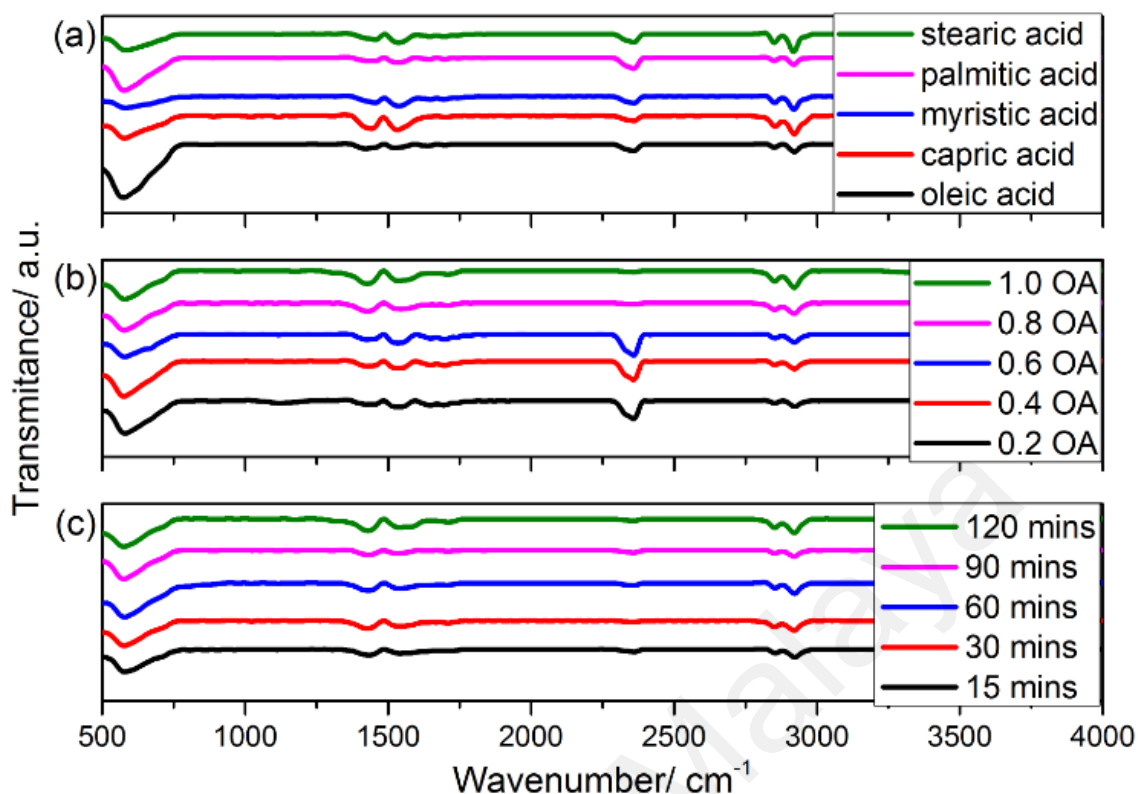


Figure 4.13: FTIR spectra of C-IONP

#### 4.2.4 Sedimentation test

Sedimentation test was carried out to determine the colloidal stability of C-IONP in water (pH= 6.5) and NBR latex (pH= 11). Observation was taken at 1 hour and 24 hours. Results were accumulated and organized in Table 4.11. In various coating agent parameter, capric, myristic and stearic acid C-IONP sedimented in both water and NBR latex medium. Palmitic acid C-IONP was stable in water medium with little of sediment at 24 hours but it is unstable in NBR latex medium. Oleic acid C-IONP on the other hand was superior without sedimentation in both water and NBR latex.

In general, it shown that the oleic acid loading parameter, 0.2 and 0.4 OA are not stable in both water and NBR latex medium. It was due to insufficient coating layers of oleic acid on IONP. 0.6, 0.8 and 1.0 OA had better colloidal stability in water than 0.2 and 0.4 OA. However, slightly sedimentation can be observed on 0.8 and 1.0 OA in NBR latex medium attributed to secondary layer of oleic acid formed. Carboxylate groups of secondary oleic acid are outward (Figure 4.14), resulting in hydrophilic surface of C-

IONP. Since acrylonitrile group of NBR latex is less than 30 %, the medium is inclined to be more hydrophobic. Therefore, a single layer oleic acid C-IONP with long hydrocarbon chain faced outside allowed them to stabilize in hydrophobic medium of NBR latex. Schematic diagram in Figure 4.15 illustrates clearly the interaction in between single and double layer C-IONP with NBR latex.

In ultra-sonication parameter, sedimentation occurred in 15 and 30 mins whereby oleic acid was not bonded completely to IONP and it reduced the efficiency of colloidal stabilization. In fact, no clear sedimentation was observed and recorded when ultra-sonication time was increased to 60 mins and above. Thus, it is concluded that 60 mins ultra-sonication time is sufficient to stabilize C-IONP in both water and NBR latex.

Table 4.11: Sedimentation test observation on C-IONP in different medium














































































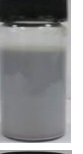












<i>Various coating agent</i>	Water (hours)			NBR latex (hours)		
	0	1	24	0	1	24
Oleic acid						
Capric acid						
Myristic acid						
Palmitic acid						
Stearic acid						

Table 4.11 (continued): Sedimentation test observation on C-IONP in different medium

	Water (hours)			NBR latex (hours)		
<i>Oleic acid loading</i>	0	1	24	0	1	24
0.2 OA						
0.4 OA						
0.6 OA						
0.8OA						
1.0 OA						
<i>Ultra-sonication time</i>	0	1	24	0	1	24
15 mins						
30 mins						
60 mins						
90 mins						
120 mins						



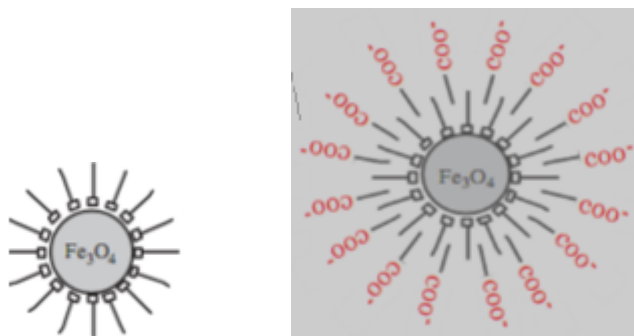


Figure 4.14: Single and double layer of oleic acid C-IONP

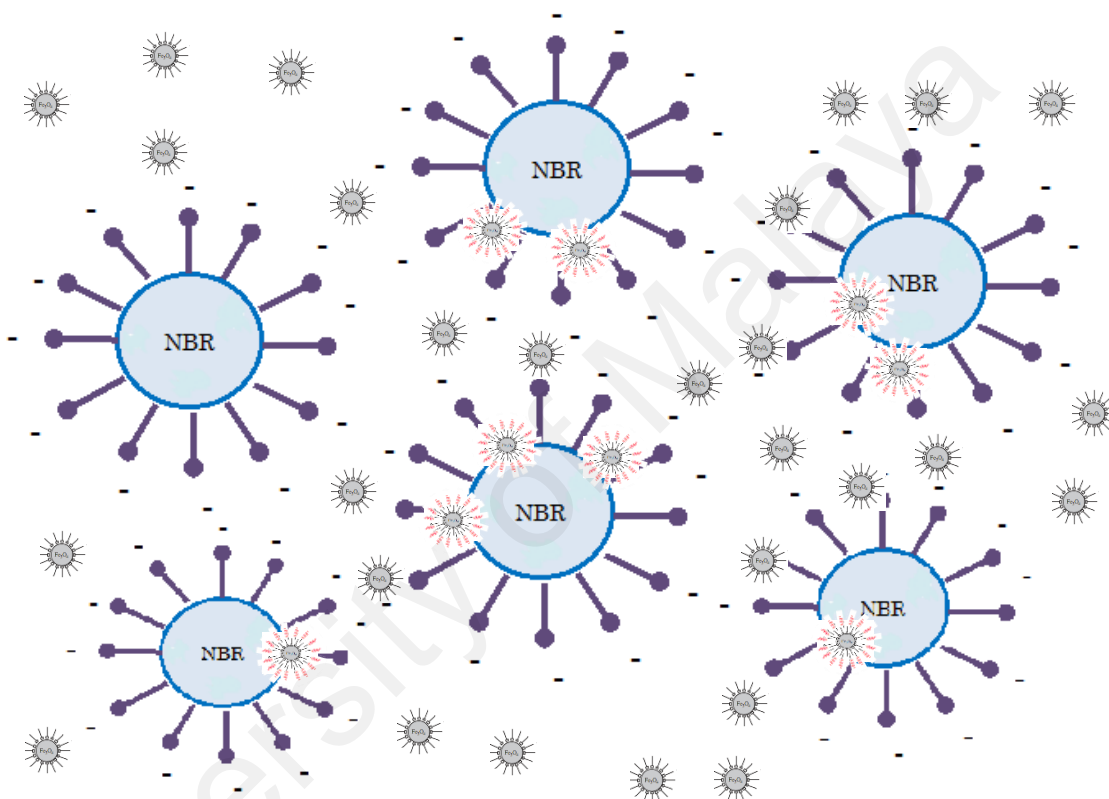


Figure 4.15: Schematic diagram of single and double layer C-IONP in NBR latex

#### 4.2.5 VSM analysis

Magnetic properties of C-IONP and its magnetization curves were shown in Table 4.12 and Figure 4.16. It was noticed that  $M_s$  of C-IONP were smaller than IONP (77.17 emu/g) attributed to the existence of coating agent. Coating agent without magnetic property shields away some magnetic properties of IONP, leading to reduction of  $M_s$ .

It was found that capric acid C-IONP has the lowest  $M_s$ , followed by oleic acid, stearic acid, palmitic acid and myristic acid C-IONP as depicted in Table 4.12. The main

reason of higher  $M_s$  of myristic acid, palmitic acid and stearic acid C-IONP was due to uneven distribution of coating agent on IONP surface. Besides that, increment values observed from the hydrophobic chain of fatty acid which is derived from capric acid, myristic acid, palmitic acid to stearic acid was reducing the  $M_s$  of C-IONP accordingly. Oleic acid C-IONP obtained the smallest  $M_s$  because presence of double bond in hydrophobic chain. The double bond allowed the long chain to bend easily, resulting in IONP encapsulation and thus shielding some magnetic properties of IONP.

In oleic acid parameter,  $M_s$  of C-IONP reduced gradually from 0.2 to 1.0 OA (from 51.60 to 38.60 emu/g). A huge drop (9.34 emu/g) of  $M_s$  from 0.2 (51.60 emu/g) to 0.4 OA (42.26 emu/g) can be accounted to increase in oleic acid bonded to IONP, proving that the shielding effect dramatically increased with increasing amount of oleic acid. The big drop was reduced to 2.23 emu/g and further reduced to less than 1.5 emu/g when oleic acid was increased from 0.4 to 1.0 OA, respectively. Slow reduction of  $M_s$  from 0.4 to 0.6 OA was owing to saturation of primary layer oleic acid coating on IONP surface. However, small reduction of  $M_s$  (<1.5 emu/g) was observed when oleic acid was increased from 0.6 to 1.0 OA. It shows that secondary layer oleic acid did not have significant impact on shielding effect.

Once the ultra-sonication time was increased from 15 to 60 mins, marginal different of  $M_s$  can be observed. The minimal reduction can be attributed to small amount difference of oleic acid added to IONP ratio as shown in Table 4.8. The  $M_s$  started to reduce to 47.24 and 45.03 at 90 and 120 min ultra-sonication time, respectively. It was due to secondary layer oleic acid formed on IONP. Insignificant changes of  $H_c$  and  $M_r$  of oleic acid C-IONP was also observed despite increasing of oleic acid loading and ultra-sonication time. This is because the nature of coating agent with IONP has only quantitative influence on the  $M_s$  mostly due to shielding effect, but the intrinsic value of IONP remained the same as reported by (Barbeta et al., 2010).

Table 4.12: Magnetic properties of C-IONP

	Coercivity, $H_c$ (G)	Remanence, $M_r$ (emu/g)	Magnetization saturation, $M_s$ (emu/g)
<b><i>Various coating agent</i></b>			
Oleic acid	55.00	4.22	54.53
Capric acid	92.01	4.22	39.82
Myristic acid	92.01	5.67	73.01
Palmitic acid	92.01	5.67	71.19
Stearic acid	64.23	8.32	66.59
<b><i>Oleic acid loading</i></b>			
0.2 OA	55.90	4.18	51.60
0.4 OA	31.15	3.49	42.26
0.6 OA	55.90	2.80	40.03
0.8OA	45.59	2.38	39.82
1.0 OA	38.02	2.38	38.60
<b><i>Ultra-sonication time</i></b>			
15 mins	43.78	3.32	49.69
30 mins	50.65	3.32	47.07
60 mins	67.84	3.32	50.90
90 mins	43.78	3.32	56.65
120 mins	30.72	3.32	45.03

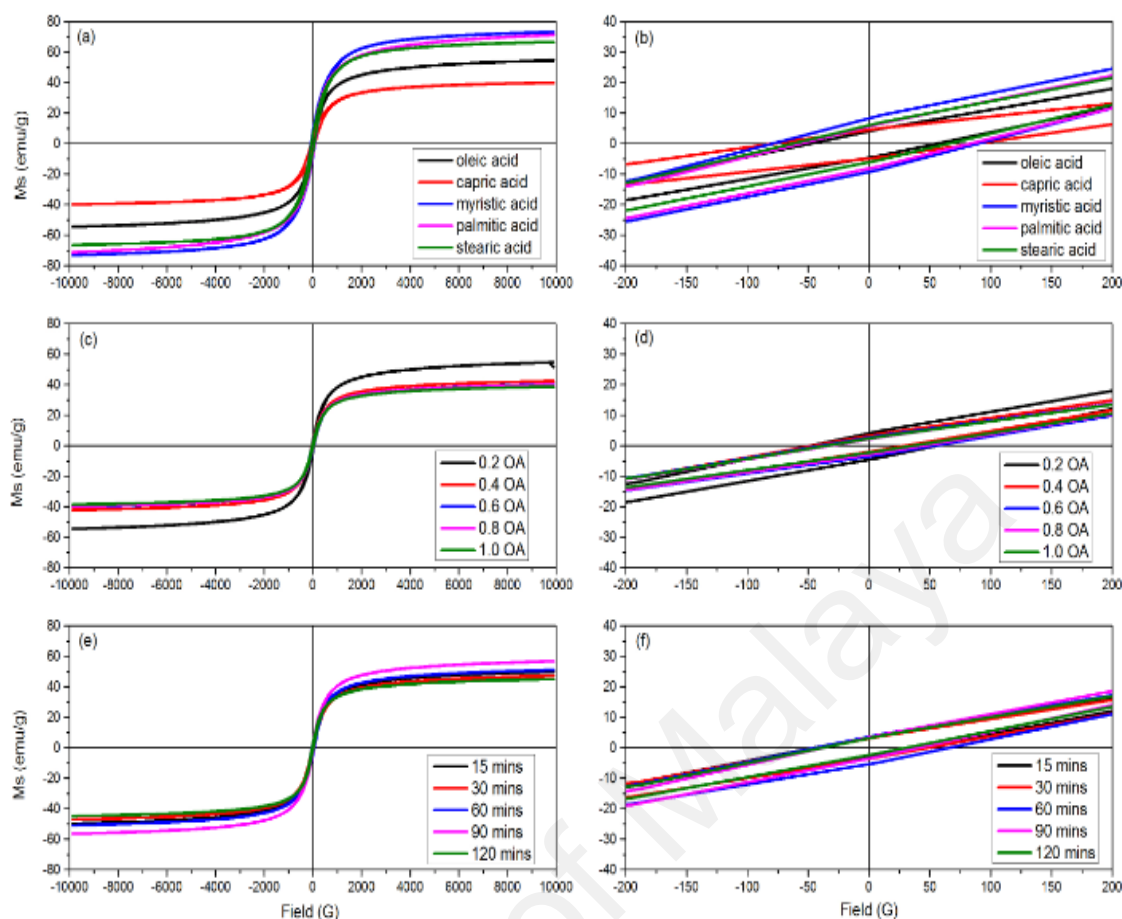


Figure 4.16: Magnetization curve of C-IONP

Throughout all the characterization, it found that oleic acid C-IONP with 0.6 OA and 60 mins is the optimized parameter in this study. Furthermore, another advantage derived from the selection of oleic acid instead of capric acid, myristic acid, palmitic acid and stearic acid was its low melting point existed in liquid state at room temperature. It would facilitate the process of coating without heating where prevailing heat might accelerate phase transition of magnetite to maghemite during coating process. Optimized oleic acid loading on the other hand was able to reduce the cost and achieve better colloidal stability in latex. Finally, optimized ultra-sonication time reduced the production of C-IONP that might be interested by industry scale.

### **4.3 C-IONP/NBR film composite**

Optimized C-IONP which acts as an additive was compounded with NBR latex at the composition of 5 to 20 phr to produce NBR/IONP composites. The produced composites were abbreviated as NBR 0, NBR 5, NBR 10, NBR 15 and NBR 20 in accordance to the composition of C-IONP with additives dosage added. The magnetic and mechanical performances of NBR/IONP composites were then analysed for VSM and Tensile test.

#### **4.3.1 Compounding analysis**

##### **4.3.1.1 Composition analysis of NBR/C-IONP compounding (TGA analysis)**

TGA analysis was done with consideration that each composites component performed a different thermal degradation temperature. In general, all the composites sample with different C-IONP loading demonstrated two distinct degradation zone exist in temperature between 180 °C and 320 °C as well as 360 °C and 500 °C. Besides, the degradation rate from 180 mins to 320 mins and 360 mins to 500 mins and residue of NBR and NBR/C-IONP are tabulated in Table 4.13. Consequently, result on temperature at different mass loss of NBR and NBR/C-IONP are summarized in Table 4.14. Figure 4.18 illustrates on effect of C-IONP loading (0 to 20 phr) towards the thermal stability of NBR. In general, all produced sample recorded the mass loss within the range of 8.12 – 10.22 % for the heating temperature of 180 °C to 320 °C. This is attributed to evaporation of the surfactant, oleic acid and wax content which strongly supported by other previous studies (Sagar et al., 2013; Li et al., 2013). As the temperature went up to 500 °C, second degradation is occurred which attributed to polymer matrix pyrolysis (Sagar et al., 2013).

However, mass losses of NBR/C-IONP composites were decreased from 84.91 % to 64.87% with increasing C-IONP loading from 0 to 20 phr. Similarly NBR/C-IONP

composites were shown to withstand a higher temperature (Table 4.14) than NBR at 10, 30 and 50 % mass loss. It can be concluded that thermal stability of NBR/C-IONP composite improved with the addition of C-IONP, contributed by high thermal stability of IONP that credit on the restriction of NBR chain mobility (Al - Juaid et al., 2011). However, the temperature of weight loss at 30 and 50 % mass loss of NBR 15 and temperature at 50 % mass loss of NBR 20 are lower than NBR. Yan and Xu (2009) reported the composites with greater IONP loading tends to agglomerate before the composite was formed, contributing to heat concentration in these composites. Hence, heat concentration would lead to lower thermal stability of the composites.

In fact, at the heating temperature of 10, 30 and 50 % mass loss of NBR 5 was higher compare to other C-IONP/NBR composites. It can be concluded that 5 phr loading of C-IONP into NBR latex gave an optimum thermal stability of the composites system. Nevertheless, presence of residue at 1000 °C as shown in Table 4.14 was due to presence of C-IONP. Percentage of residue increased when the loading of incorporation of C-IONP into NBR was increased. IONP have higher degradation temperature, contributing to higher residue percentage compare to compounded NBR. Indeed, NBR 5 was optimized C-IONP loading as it provided good thermal stability of product as well as lower cost of C-IONP/NBR composites. It also claimed that NBR 5 has better C-IONP distribution in NBR latex which it enables heat to distribute evenly within the whole composite composition.

Table 4.13: Mass loss, degradation rate and residue of NBR and C-IONP/NBR film composites

Sample	Mass loss at temperature (%)		Residue (%)
	180 °C to 320 °C	360 °C to 500 °C	
<b>NBR</b>	10.22	84.91	4.23
<b>NBR 5</b>	8.12	82.29	8.79
<b>NBR 10</b>	10.21	75.23	14.15
<b>NBR 15</b>	9.11	71.59	18.63
<b>NBR 20</b>	9.10	64.87	25.74

Table 4.14: Temperature at different mass loss of NBR and C-IONP/NBR film composites

Sample	Temperature at 10% mass loss (°C)	Temperature at 30% mass loss (°C)	Temperature at 50% mass loss (°C)
<b>NBR</b>	395	440	458
<b>NBR 5</b>	414	444	461
<b>NBR 10</b>	399	439	460
<b>NBR 15</b>	405	438	457
<b>NBR 20</b>	405	438	459

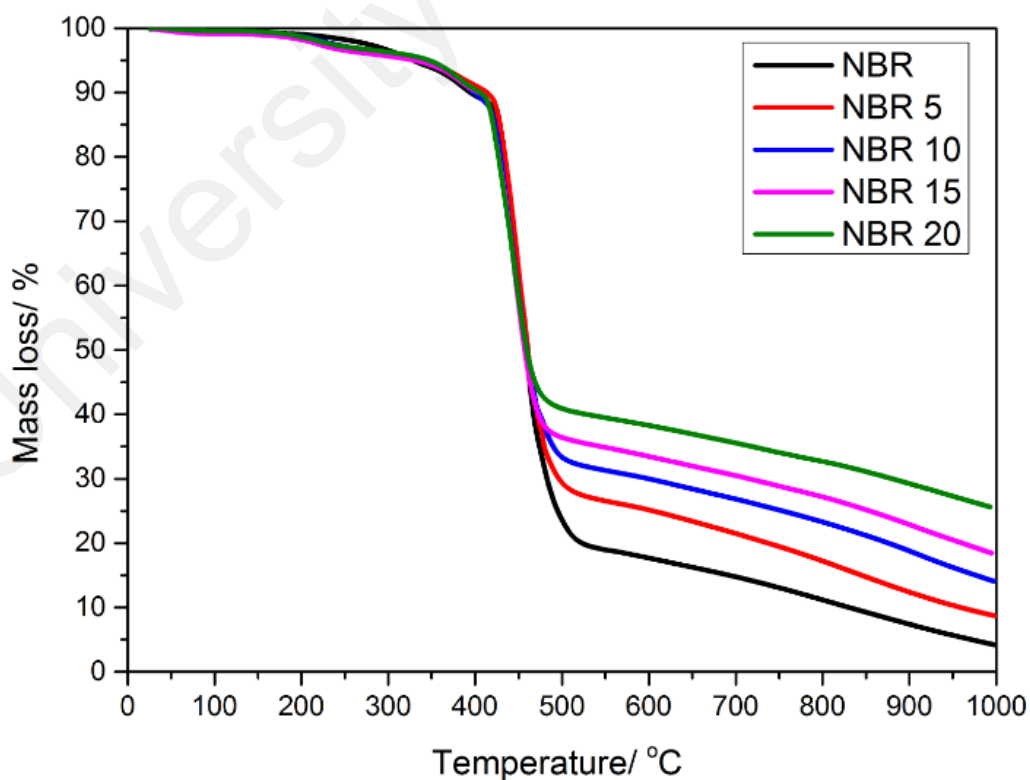


Figure 4.18: TGA curves of NBR and C-IONP/NBR film composites

#### 4.3.1.2 NBR/C-IONP interaction analysis (FTIR)

The surface interactions of C-IONP within the NBR matrix was analysed through the formation of the functional groups visualized through the FTIR analysis. FTIR spectra of NBR and NBR 5 are given in Figure 4.18. Major peaks of FTIR are illustrated in Table 4.15. Major FTIR peaks of IONP and fatty acid band was discussed in section 4.2.3. NBR 5 was selected as representative to all C-IONP/NBR film composite. C≡N bond stretching and C-H wagging motion presented at 2230 and 960 cm<sup>-1</sup>, respectively, indicating NBR copolymer which consisted of acrylonitrile functional group and butadiene chain. The 1076 cm<sup>-1</sup> was identified as symmetric C-S-C group stretching vibration to crosslinking of NBR rubber occurring between butadiene chain. Two peaks at 1710 and 565 cm<sup>-1</sup> were found only in NBR 5 which presented as C=O and Fe-O band, respectively. Hence, Fe-O band proved that IONP existed in NBR 5. The existence of C=O on the other hand shows that unreacted oleic acid, i.e. chemically in tact is presence in NBR 5, 10, 15 and 20.

Table 4.15: FTIR major peaks assignment of NBR and C-IONP/NBR film composite (Gunasekaran, Natarajan, & Kala, 2007; Liang et al., 2014)

Band Assignments	Wavenumber (cm <sup>-1</sup> )
<i>Characteristic of IONP band</i>	
O-H vibration	1632
Fe-O lattice vibration	634, 565
<i>Characteristic of fatty acid band</i>	
Asymmetric and symmetric C-H stretching vibration	2923, 2854
C-C stretching vibration	1115
C-O stretching vibration	1048
C=O stretching vibration	1710
<i>Characterization of NBR film</i>	
Alkyl C≡N stretching vibration	2230
O-H stretching vibration	3470
Symmetric C-S-C group stretching vibration	1076
C-H wagging motion of butadiene	960
Asymmetric and symmetric C-H stretching vibration	2950, 2853



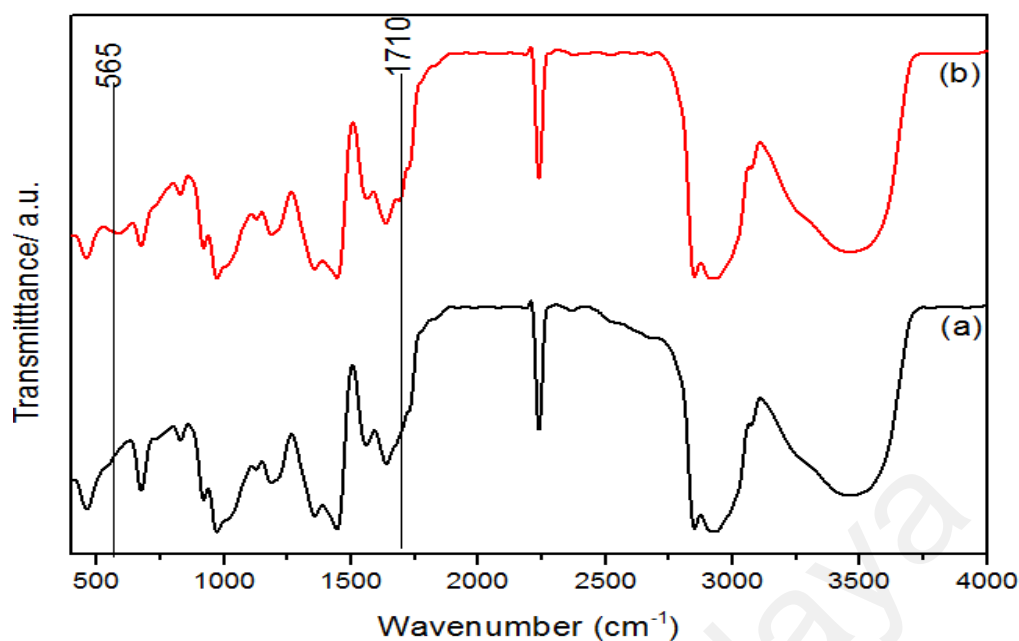


Figure 4.18: FTIR spectra of (a) NBR and (b) NBR 5

### 4.3.2 Magnetic properties of NBR/IONP composites

#### 4.3.2.1 VSM analysis of NBR/C-IONP composites

Magnetic properties of NBR and C-IONP/NBR composites are illustrated in Table 4.16 and Figure 4.19. Small reverse magnetization curves of NBR were observed in Figure 4.19(a)(i) and (b)(i), indicating diamagnetic susceptibility of NBR chains against magnetic field (Reinholds, Kalkis, & Maksimovs, 2012). It was noticed that  $H_c$  and  $M_r$  of all NBR and C-IONP/NBR were relatively small whereby  $H_c$  and  $M_r$  were smaller than 50 G and 1 emu/g, respectively. Huge drop of  $H_c$  and  $M_r$  of IONP (99.97 G and 9.58 emu/g, respectively) were attributed to shielding effect of oleic acid as well as NBR film. In fact, these properties would reduce the probability of C-IONP/NBR film sticking to each other. Hence, the marginal  $H_c$  and  $M_r$  merits the magnetic-composite to be classified as soft magnetic composite materials (Taghvaei et al., 2010). Magnetic properties of C-IONP/NBR composite films were investigated in two different orientations: 1) parallel, and 2) perpendicular to magnetic field. From the results, the differences of  $M_s$  between parallel and perpendicular magnetic field are 0.25 [NBR 5

and NBR 5(P)], 0.15 [NBR 10 and NBR 10(P)], 0.52 [NBR 15 and NBR 15(P)] as well as 0.46 [NBR 20 and NBR 20(P)].  $M_s$  values of C-IONP/NBR for parallel to magnetic field was smaller than  $M_s$  perpendicular to magnetic field. Hence, it was important to identify the lowest  $M_s$  at smallest C-IONP loading to ensure the magnetic susceptibility towards magnetic detector.

Apart from that,  $M_s$  values of C-IONP/NBR composite increase consistently from NBR 0 to 20 for both parallel and perpendicular directions to magnetic field. High loading of C-IONP improved magnetic properties of C-IONP/NBR composite, thus improving detectability of the composite.  $M_s$  of IONP (77.17 emu/g) was reduced to less than 6 emu/g attributed to shielding effect of NBR film towards IONP and at lower concentration of IONP in the composite. According to Zaborski and Masłowski (2011), IONP are well aligned in NBR matrix, and thus it has larger magnetic susceptibility. Therefore, it is suitable to incorporate C-IONP into NBR latex as proven by the lowest  $M_s$  of NBR 5 (1.24 emu/g). In our study, a Safeline model S35 metal-particle detector can detect magnetic moment as low as 0.80 emu/g and NBR 5 already exceeded the minimum magnetic moment sensor of the detector (De Ricci & Phalip, 1999).

Table 4.16: Magnetic properties of NBR and C-IONP/NBR composites

	Coercivity, $H_c$ (G)	Remanence, $M_r$ (emu/g)	Magnetization saturation, $M_s$ (emu/g)
<i>Parallel to magnetic field</i>			
NBR (P)	36.51	$0.54 \times 10^{-3}$	-0.16
NBR 5(P)	9.32	$0.44 \times 10^{-3}$	1.24
NBR 10(P)	10.67	$0.26 \times 10^{-3}$	2.10
NBR 15(P)	16.97	$1.65 \times 10^{-3}$	4.04
NBR 20(P)	21.84	$1.30 \times 10^{-3}$	5.13
<i>Perpendicular to magnetic field</i>			
NBR	NA	$0.55 \times 10^{-3}$	-0.18
NBR 5	8.97	$0.36 \times 10^{-3}$	1.49
NBR 10	8.00	$0.39 \times 10^{-3}$	2.25
NBR 15	14.84	$0.50 \times 10^{-3}$	4.56
NBR 20	18.42	$0.95 \times 10^{-3}$	5.59

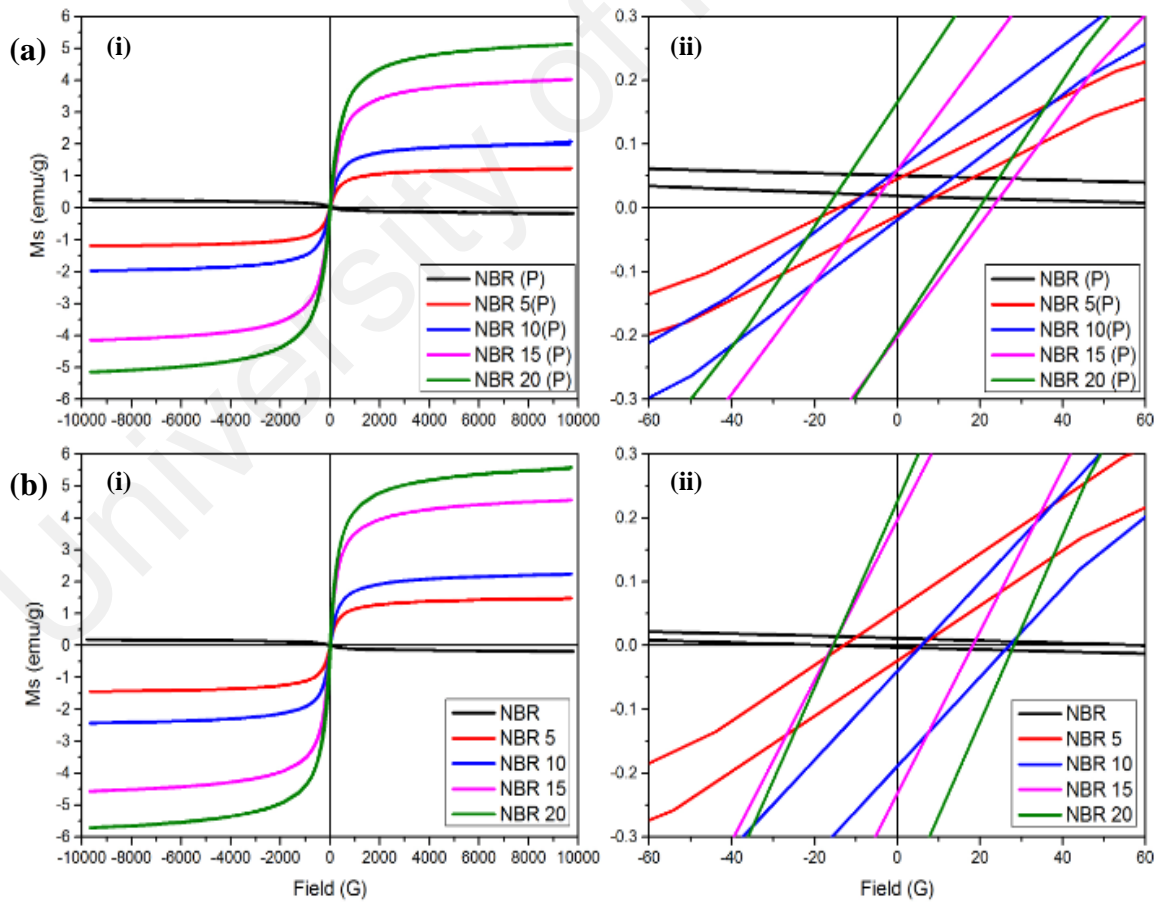


Figure 4.19: Magnetization curves of NBR and C-IONP/NBR composites

### **4.3.3 Mechanical properties of NBR/C-IONP composites**

#### **4.3.3.1 Tensile properties of NBR/C-IONP composites**

The mechanical properties of NBR and C-IONP/NBR film composite were summarized in Table 4.17 and Figure 4.20. The stress-strain curves of these composites were shown in Figure 4.20(a). It was noticed that they behave similarly at low strain (below 150 % strain). At high strain region, tensile stress of NBR 15 and 20 increased dramatically as compared to neat NBR attributed to filler-filler interaction in C-IONP. Meanwhile, lower tensile strength increment rate of NBR 5 and 10 than neat NBR was due to present of C-IONP which increased the strain more than 700 %. It is expected that, due to the high visco-elasticity and macromolecules structure of oleic acid, the C-IONP tended to plasticise NBR latex due to presence of unreacted oleic acid in C-IONP, thus leading to higher strain. In Figure 4.20(b), tensile strength of NBR 5 was higher than neat NBR but tensile strength was reduced tremendously as C-IONP increased to 10 phr and above. Here, it can be said that C-IONP at 5 phr acted as reinforcing agent to improve the tensile strength of NBR film. However, at higher loading of C-IONP in NBR latex, the C-IONP is prone to agglomerate, consequently become an obstacle for rubber matrix to attract on each other by formation on dipole-dipole interactions (El-Nemr et al., 2014).

Furthermore, elastic modulus of NBR composite was decreased consistently from 15.06 to 9.18 MPa for NBR to NBR 20, respectively as indicated in Figure 4.20(c). The resistance of deformation by applied force was reduced as presence of unreacted oleic acid in C-IONP as discussed. Besides that, tensile stress at 500 % elongation (engineering modulus, M500) was decreased from 8.11 to 6.70 MPa when C-IONP was increased from 0 to 10 phr but increased to 10.40 MPa at 20 phr loading of C-IONP as shown in Figure 4.17(d). M500 is an indicator of rubber compound stiffness (Hwang, Wei, & Wu, 2004). Unreacted oleic acid would tend to reduce the stiffness of NBR film

at low loading of C-IONP (5 to 10 phr). When C-IONP was increased to 15 and 20 phr, agglomerated C-IONP tended to hinder molecular chain motion of NBR, resulting higher stiffness in NBR 15 and 20. In fact, high stiffness would reduce the flexibility effect of NBR film which is disadvantage for glove donning.

Table 4.17: Mechanical properties of NBR and C-IONP/NBR film composites

	Stress (MPa)	Modulus (MPa)	Strain (%)	M500 (MPa)
NBR	28.56	15.06	733.34	8.11
NBR 5	28.93	13.40	810.68	6.57
NBR 10	26.82	12.09	797.50	6.70
NBR 15	26.15	10.81	759.02	9.22
NBR 20	25.17	9.18	718.32	10.40

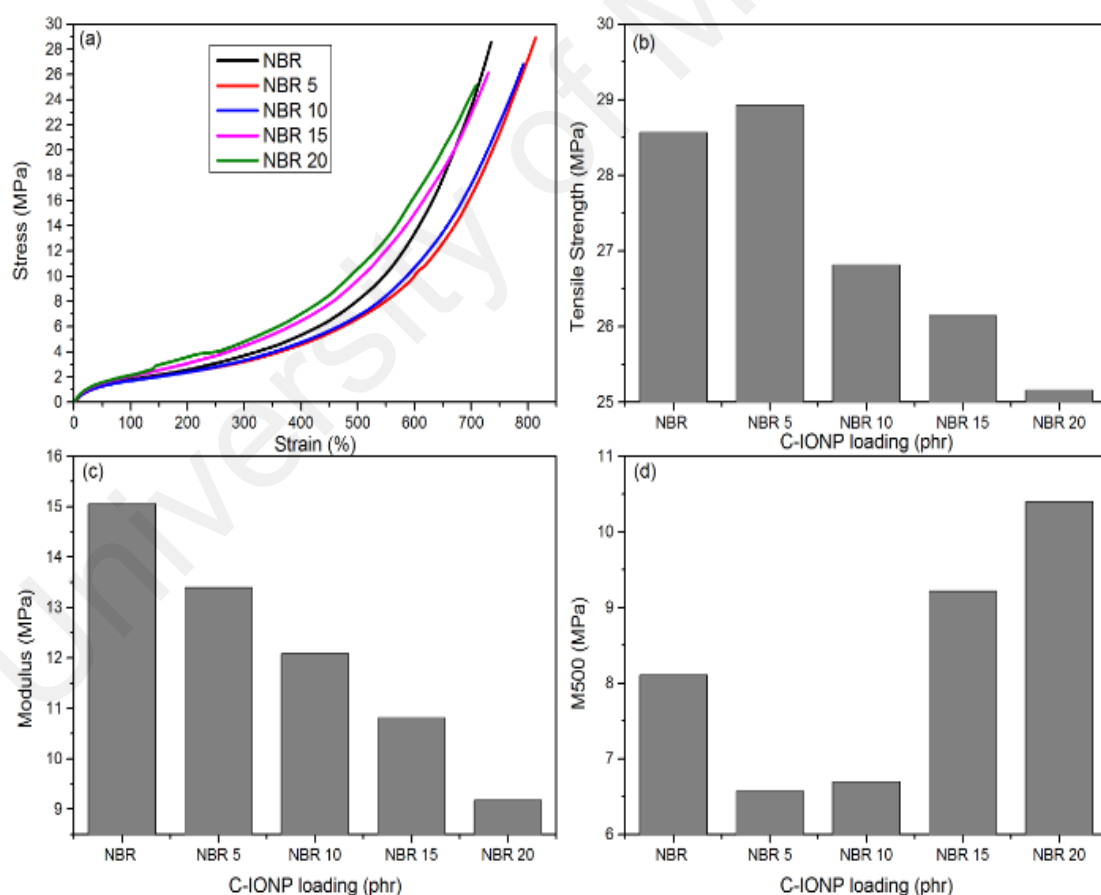


Figure 4.20: (a) Stress-strain behavior of NBR and C-IONP/NBR film composite  
(b) Tensile strength of different C-IONP loading  
(c) Elastic modulus of different C-IONP loading  
(d) Tensile stress at 500 % elongation of different C-IONP loading

#### 4.3.3.2 Fracture surface analysis of NBR/C-IONP composites

Fracture surface morphology of NBR and C-IONP/NBR film composites were investigated by FESEM and the micrographs are shown in Figure 4.21. NBR and C-IONP/NBR film composites show roughness fracture surface due to ductile property of NBR matrix. C-IONP particles are presented by brighter area, and they are well distributed in the NBR 5, 10 15 and 20. Agglomeration of C-IONPs in NBR matrix are prominently observed when C-IONP as C-IONP loading increased up to 10 phr. The agglomerated area was increased from NBR 5 to 20 due to magnetic dipole moment of C-IONP as shown in Table 4.18. Through this analysis, tensile strength reduction of NBR 10, 15 and 20 can be explained by highly agglomerated C-IONP and bad interfacial zone in between C-IONP and NBR matrix. High agglomeration of C-IONP would lead to low rubber-rubber interaction of NBR matrix while bad interaction zone in between NBR matrix and C-IONP would reduce the rubber-filler interaction. In fact, rubber-rubber and rubber-filler interaction are one of the contributor to the tensile properties (Gent, 2012). Nevertheless, higher tensile strength of NBR 5 was contributed by salt crosslinking of zinc oleate (Ibarra et al., 2002) . Zinc oleate was formed in the process of compounding due to unreact oleic acid in C-IONP slurry interacted with zinc oxide. Subsequently, zinc oleate would react with NBR latex and crosslinked as shown in Figure 4.22. High tensile strength while retaining strain percentage of NBR 5 given in Figure 4.17(a) is in good agreement with Yuan et al. (2000). Small agglomeration of C-IONP in NBR 5 as indicated in Table 4.17 and well distribution of C-IONP [Figure 4.21(a)(i)] have minimum effect on tensile strength reduction. Thus, the highest tensile strength of NBR 5 in Figure 4.20(b) was explained.

Table 4.18: Agglomerated C-IONP in NBR and C-IONP/NBR film composites

	Biggest Area ( $\mu\text{m}^2$ )	Smallest Area ( $\mu\text{m}^2$ )	Average ( $\mu\text{m}^2$ )
NBR	NA	NA	NA
NBR 5	17.45	2.34	8.084
NBR 10	31.82	11.24	17.617
NBR 15	36.87	11.98	23.206
NBR 20	54.01	13.71	23.017

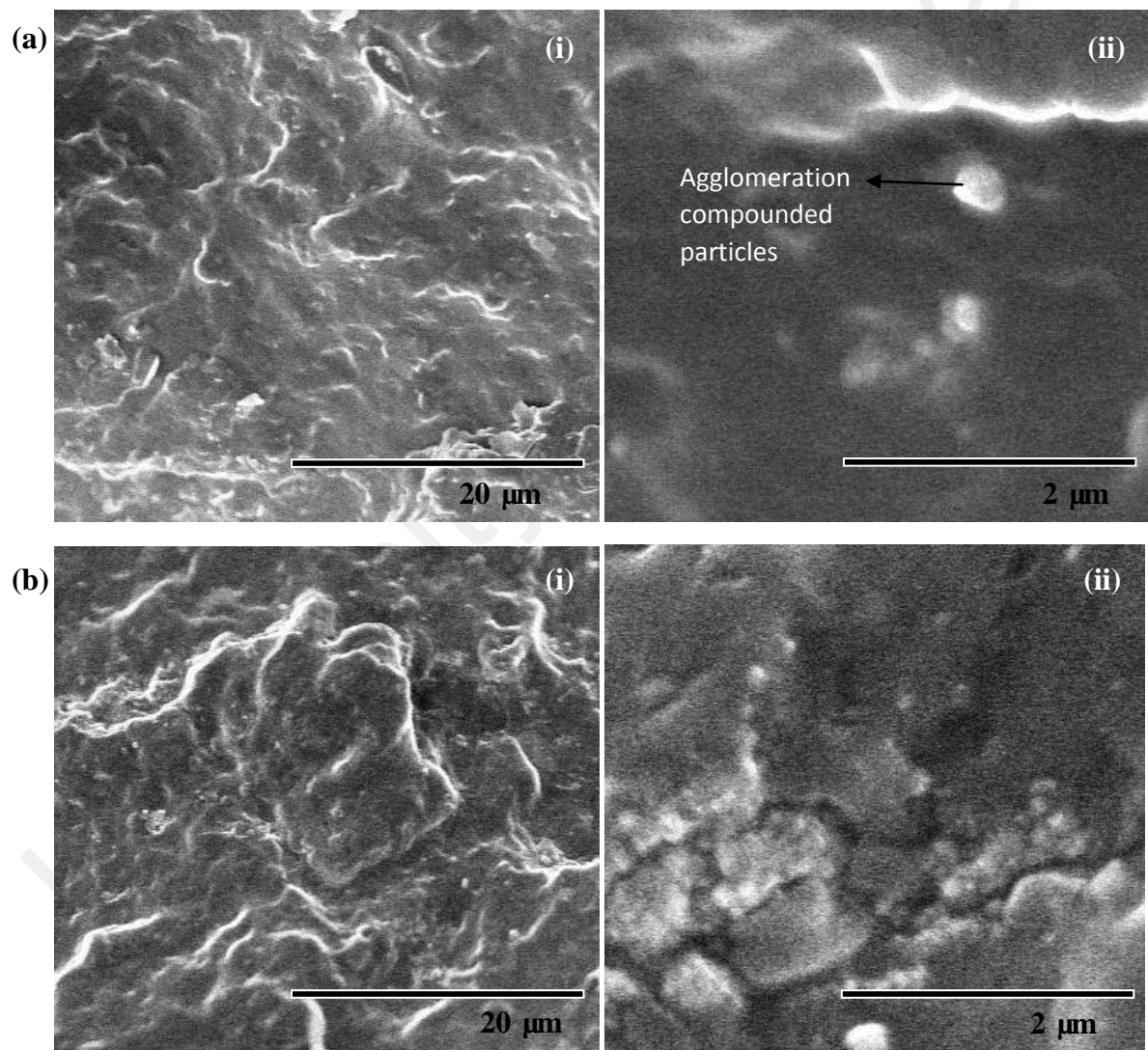


Figure 4.21: FESEM micrographs (a)NBR (b)NBR 5 at (i) 2000 $\times$  magnification and (ii) 20000 $\times$  magnification.

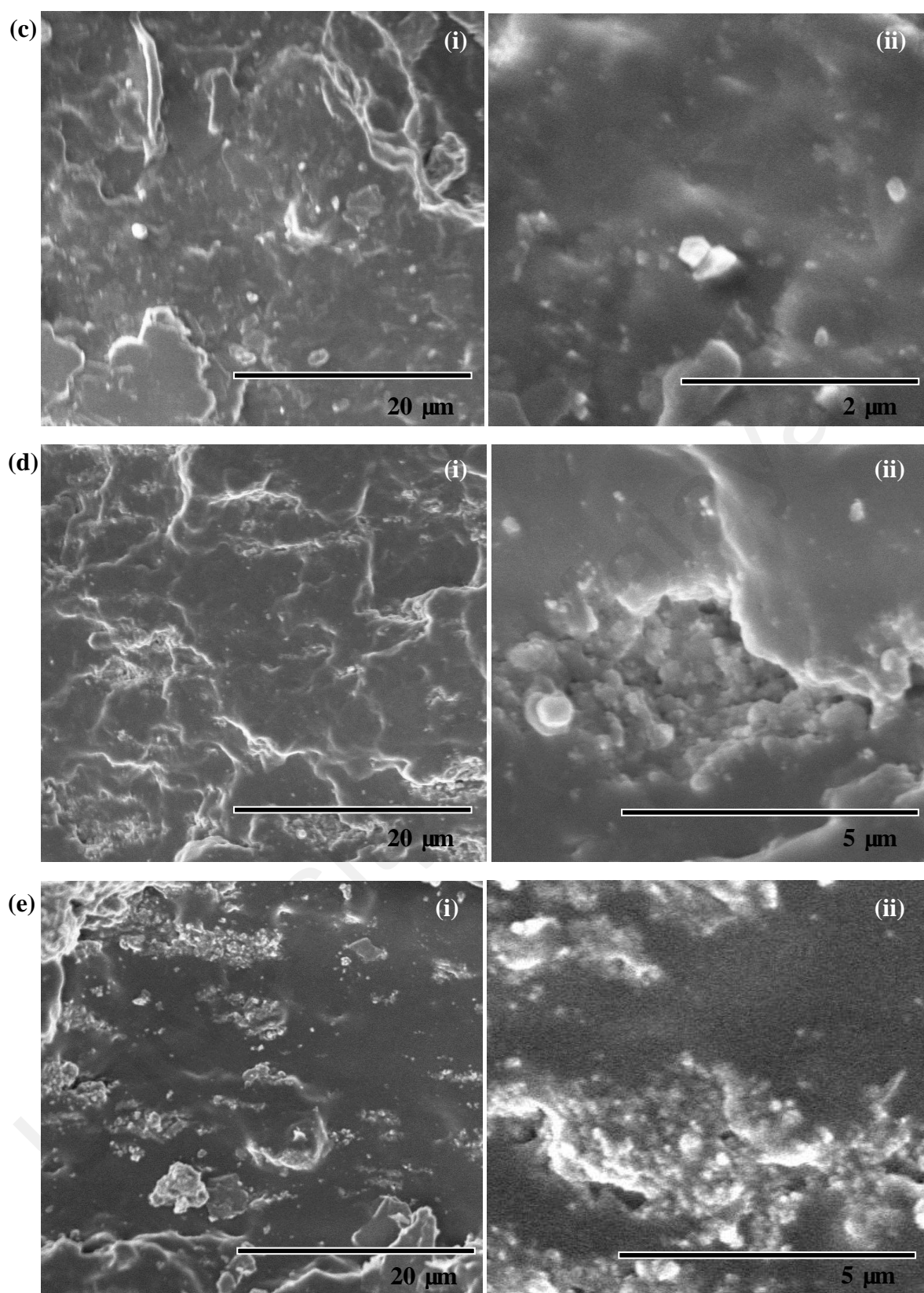


Figure 4.21 (Continued): FESEM micrographs (c)NBR 10 (d)NBR 15 (e)NBR 20 at (i) 2000 $\times$  magnification and (ii) 20000 $\times$  magnification



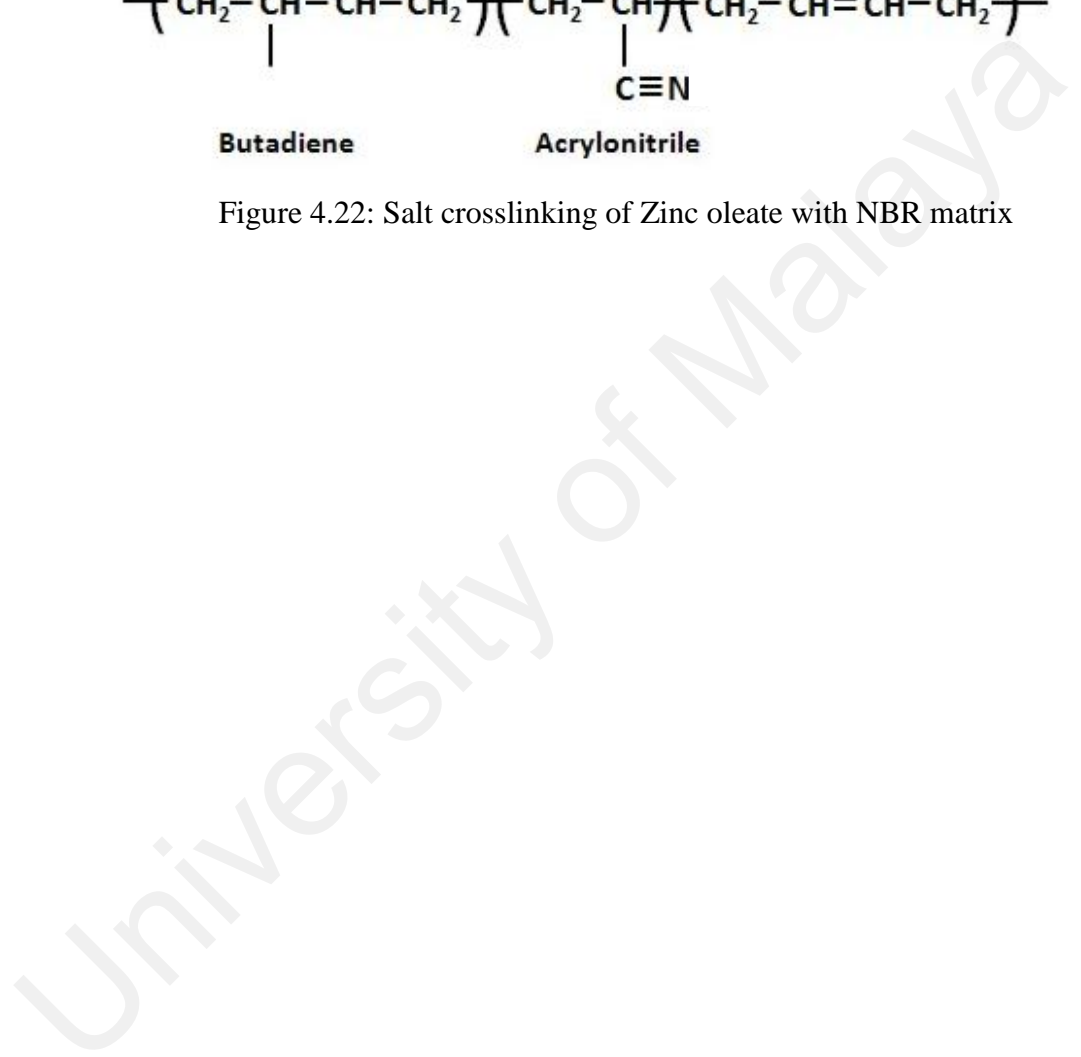


Figure 4.22: Salt crosslinking of Zinc oleate with NBR matrix

## CHAPTER 5

### CONCLUSION AND SCOPE OF FUTURE WORK

#### 5.1 Conclusions

It was found that reverse precipitation,  $\text{FeSO}_4 \cdot 7\text{H}_2\text{O}$  as precursor and pour once method with 1.5 hr of aging time were the optimum condition to obtain IONP with the considerable properties as nano magnetic additive for NBR film. It shows the highest percentage of magnetite phase with low percentage of hematite and goethite phase has been analysed under XRD and Raman Spectroscopy analysis. It was proven by the HRTEM image that no needle shape can be identified and less agglomeration of IONP. Thus, high magnetization was promoted attributed to high content of magnetite phase.  $M_s$  of optimized IONP was the highest (77.17 emu/g) which make it excellent magnetic nanoadditives to be incorporated with NBR latex. The particle size of IONPs was analysed under Zeta Potential and HRTEM analysis and it found that IONPs are in nanosize with the smallest size 65.4 nm and 22.6 nm, respectively. The formation of nanosized with high saturated magnetic properties increases the possibility for IONPs to be promising nano magnetic additive for NBR film. This consequently reduces the total usage of IONPs, production cost as well as the energy consumption on the production of magnetic metal detectable NBR gloves. Meanwhile, better and homogenous distribution within the NBR matrix is expected due to the large surface of IONPs.

In order to better interaction, stability, dispersion and homogeneity of IONP with the NBR matrix, IONPs was further coated and form C-IONPs. C-IONP on the other hand was found optimized with oleic acid at 0.6 OA and 60 mins ultra-sonication time. Oleic acid C-IONP was small in hydrodynamic size and PDI, leading it outperformed than other fatty acids. Apart from that, oleic acid consisted of double bond within the long

hydrocarbon chain and thus, it encapsulated IONP well. Two layer of oleic acid could be determined in C-IONP by FTIR and TGA analysis. Single layer of C-IONP was identified at 0.6 OA and 60 mins ultra-sonication time and it consequently stabilized well in both water and NBR latex. It is due to the nature of low acrylonitrile group existed in NBR latex. Therefore, single layer of C-IONP was preferably to stabilize well in NBR latex. Similarly, low oleic acid ratio would contribute to lower cost of NBR composite.  $M_s$  of C-IONP was lower than IONP because of shielding effect of non-magnetic oleic acid coating.

Finally, 5 phr of C-IONP loading (NBR 5) was greatly found as the optimum parameter incorporating with NBR latex as the magnetism and mechanical properties of the composites was concerned. The tensile property was improved slightly with NBR 5 but reduced when further increased to NBR 10, 15 and 20. It was due to presence of un-react oleic acid that would plasticise NBR latex. Furthermore, the heating temperature of 10, 30 and 50 % mass loss of NBR 5 was higher compare to other C-IONP/NBR composites. Hence, NBR 5 gave an optimum thermal stability of the composites system. Even though its  $M_s$  was the lowest among the C-IONP/NBR composites, it exceeded the minimum magnetic detectability (0.80 emu/g) of a Safeline model S35 metal-particle detector.

In a nut shell, the optimization of IONP, C-IONP and loading of C-IONP that is suitable to incorporate with NBR latex has been clearly reported to produce a metal detectable NBR gloves as the main objective of this study

## 5.2 Suggestion of future work

Many possibilities for extensions to this research in terms of the practical applications of nanomaterials or nanocomposites in latex industries, which includes:

- Feasible study on incorporation of IONP with other type of rubber latex such as natural rubber and styrene-butadiene rubber.
- Hybridization of IONP with titanium dioxide or graphene oxide to improve the tensile, dispersibility and antimicrobial properties
- In-situ synthesis of C-IONP to incorporate with NBR latex in order to reduce agglomeration of C-IONP in NBR latex.
- Other type of mechanical characterization such as tearing test, puncture test and so on can be carried out to check out the performance of the composite.

## REFERENCES

- Abragam, A., & Bleaney, B. (2012). *Electron paramagnetic resonance of transition ions*. Oxford University Press.
- Adachi, H., & Ino, H. (1999). *A ferromagnet having no net magnetic moment*. *Nature*, 401(6749), 148-150.
- Al - Ghamdi, A., Al - Hartomy, O. A., Al - Salamy, F., Al - Ghamdi, A. A., El - Mossalamy, E., Abdel Daiem, A., & El - Tantawy, F. (2012). *Novel electromagnetic interference shielding effectiveness in the microwave band of magnetic nitrile butadiene rubber/magnetite nanocomposites*. *Journal of Applied Polymer Science*, 125(4), 2604-2613.
- Al - Juaid, S. S., El - Mossalamy, E., M Arafa, H., Al - Ghamdi, A., Daiem, A., & El - Tantawy, F. (2011). *Novel functional nitrile butadiene rubber/magnetite nano composites for NTCR thermistors application*. *Journal of Applied Polymer Science*, 121(6), 3604-3612.
- Aono, H., Hirazawa, H., Naohara, T., Maehara, T., Kikkawa, H., & Watanabe, Y. (2005). *Synthesis of fine magnetite powder using reverse coprecipitation method and its heating properties by applying AC magnetic field*. *Materials research bulletin*, 40(7), 1126-1135.
- Avdeev, M., Bica, D., Vekas, L., Aksenov, V., Feoktystov, A., Marinica, O., . . . Willumeit, R. (2009). *Comparative structure analysis of non-polar organic ferrofluids stabilized by saturated mono-carboxylic acids*. *Journal of colloid and interface science*, 334(1), 37-41.
- Barbeta, V., Jardim, R., Kiyohara, P., Effenberger, F., & Rossi, L. (2010). *Magnetic properties of Fe<sub>3</sub>O<sub>4</sub> nanoparticles coated with oleic and dodecanoic acids*. *Journal of Applied Physics*, 107(7), 073913-073913-073917.
- Barrera, C., Herrera, A. P., Bezares, N., Fachini, E., Olayo-Valles, R., Hinestroza, J. P., & Rinaldi, C. (2012). *Effect of poly (ethylene oxide)-silane graft molecular weight on the colloidal properties of iron oxide nanoparticles for biomedical applications*. *Journal of colloid and interface science*, 377(1), 40-50.
- Baumgartner, J., Bertinetti, L., Widdrat, M., Hirt, A. M., & Faivre, D. (2013). *Formation of magnetite nanoparticles at low temperature: from superparamagnetic to stable single domain particles*. *PLoS ONE*, 8(3), e57070.
- Behl, M., Razzaq, M. Y., & Lendlein, A. (2010). *Multifunctional Shape - Memory Polymers*. *Advanced materials*, 22(31), 3388-3410.

- Beydoun, D., Amal, R., Low, G., & McEvoy, S. (2002). Occurrence and prevention of photodissolution at the phase junction of magnetite and titanium dioxide. *Journal of Molecular Catalysis A: Chemical*, 180(1), 193-200.
- Bindu, P., & Thomas, S. (2013). Viscoelastic Behavior and Reinforcement Mechanism in Rubber Nanocomposites in the Vicinity of Spherical Nanoparticles. *The Journal of Physical Chemistry B*, 117(41), 12632-12648.
- Brok, E., Frandsen, C., Madsen, D. E., Jacobsen, H., Birk, J. O., Lefmann, K., . . . Berhe, A. (2014). Magnetic properties of ultra-small goethite nanoparticles. *Journal of Physics D: Applied Physics*, 47(36), 365003.
- Chourpa, I., Douziech-Eyrolles, L., Ngaboni-Okassa, L., Fouquenot, J.-F., Cohen-Jonathan, S., Soucé, M., . . . Dubois, P. (2005). Molecular composition of iron oxide nanoparticles, precursors for magnetic drug targeting, as characterized by confocal Raman microspectroscopy. *Analyst*, 130(10), 1395-1403.
- Cornell, R. M., & Schwertmann, U. (2006). *The iron oxides: structure, properties, reactions, occurrences and uses*: John Wiley & Sons.
- Dao, N. N., Dai Luu, M., Nguyen, Q. K., & Kim, B. S. (2011). UV absorption by cerium oxide nanoparticles/epoxy composite thin films. *Advances in Natural Sciences: Nanoscience and Nanotechnology*, 2(4), 045013.
- Daou, T., Pourroy, G., Begin-Colin, S., Greneche, J., Ulhaq-Bouillet, C., Legaré, P., . . . Rogez, G. (2006). Hydrothermal synthesis of monodisperse magnetite nanoparticles. *Chemistry of Materials*, 18(18), 4399-4404.
- Dar, M. I., & Shivashankar, S. (2014). Single crystalline magnetite, maghemite, and hematite nanoparticles with rich coercivity. *RSC Advances*, 4(8), 4105-4113.
- de Carvalho, J., de Medeiros, S., Morales, M., Dantas, A., & Carriço, A. (2013). Synthesis of magnetite nanoparticles by high energy ball milling. *Applied Surface Science*, 275, 84-87.
- De Matteis, L., Custardoy, L., Fernández-Pacheco, R., Magén, C. s., de la Fuente, J. s. M., Marquina, C., & Ibarra, M. R. (2012). Ultrathin MgO Coating of Superparamagnetic Magnetite Nanoparticles by Combined Coprecipitation and Sol–Gel Synthesis. *Chemistry of Materials*, 24(3), 451-456.
- De Matteis, L., Fernández-Pacheco, R., Custardoy, L., García-Martín, M. L., de la Fuente, J. s. M., Marquina, C., & Ibarra, M. R. (2014). Influence of a Silica Interlayer on the Structural and Magnetic Properties of Sol–Gel TiO<sub>2</sub>-Coated Magnetic Nanoparticles. *Langmuir*, 30(18), 5238-5247.

- De Ricci, S., & Phalip, P. (1999). Detectable polymeric protective gloves: Google Patents.
- Demortiere, A., Panissod, P., Pichon, B., Pourroy, G., Guillon, D., Donnio, B., & Begin-Colin, S. (2011). Size-dependent properties of magnetic iron oxide nanocrystals. *Nanoscale*, 3(1), 225-232.
- Deng, Y.-H., Wang, C.-C., Hu, J.-H., Yang, W.-L., & Fu, S.-K. (2005). Investigation of formation of silica-coated magnetite nanoparticles via sol-gel approach. *Colloids and Surfaces A: Physicochemical and Engineering Aspects*, 262(1), 87-93.
- Dorniani, D., Kura, A. U., Hussein-Al-Ali, S. H., Bin Hussein, M. Z., Fakurazi, S., Shaari, A. H., & Ahmad, Z. (2014). In vitro sustained release study of gallic acid coated with magnetite-PEG and magnetite-PVA for drug delivery system. *The Scientific World Journal*, 2014.
- Drabek, T., Boucek, C. D., & Buffington, C. W. (2013). Wearing ambidextrous vinyl gloves does not impair manual dexterity. *Journal of occupational and environmental hygiene*, 10(6), 307-311.
- Eivari, H. A., & Rahdar, A. (2013). Some Properties of Iron Oxide Nanoparticles Synthesized in Different Conditions. *World Applied Programming*, 3(2).
- El-Nemr, K., Balboul, M., & Ali, M. (2014a). Electrical and mechanical properties of manganese dioxide-magnetite-filled acrylonitrile butadiene rubber blends. *Journal of Thermoplastic Composite Materials*, 0892705714533372.
- El-Nemr, K., Balboul, M., & Ali, M. (2014b). Electrical and Mechanical Properties of Manganese Dioxide (Magnetite) Filled NBR Rubber Blends.
- El Ghandoor, H., Zidan, H., Khalil, M. M., & Ismail, M. (2012). Synthesis and some physical properties of magnetite (Fe<sub>3</sub>O<sub>4</sub>) nanoparticles. *Int. J. Electrochem. Sci*, 7, 5734-5745.
- Faraji, M., Yamini, Y., & Rezaee, M. (2010). Magnetic nanoparticles: synthesis, stabilization, functionalization, characterization, and applications. *Journal of the Iranian Chemical Society*, 7(1), 1-37.
- García-Jimeno, S., & Estelrich, J. (2013). Ferrofluid based on polyethylene glycol-coated iron oxide nanoparticles: Characterization and properties. *Colloids and Surfaces A: Physicochemical and Engineering Aspects*, 420, 74-81.
- Ge, S., Shi, X., Sun, K., Li, C., Uher, C., Baker Jr, J. R., . . . Orr, B. G. (2009). Facile hydrothermal synthesis of iron oxide nanoparticles with tunable magnetic properties. *The Journal of Physical Chemistry C*, 113(31), 13593-13599.

- Gent, A. N. (2012). *Engineering with rubber: how to design rubber components*: Carl Hanser Verlag GmbH Co KG.
- German, S., Inozemtseva, O., Navolokin, N., Pudovkina, E., Zuev, V., Volkova, E., . . . Gorin, D. (2013). Synthesis of magnetite hydrosols and assessment of their impact on living systems at the cellular and tissue levels using MRI and morphological investigation. *Nanotechnologies in Russia*, 8(7-8), 573-580.
- Gogoi, M., Deb, P., Vasan, G., Keil, P., Kostka, A., & Erbe, A. (2012). Direct monophasic replacement of fatty acid by DMSA on SPION surface. *Applied Surface Science*, 258(24), 9685-9691.
- Greene, D., Serrano-Garcia, R., Govan, J., & Gun'ko, Y. K. (2014). Synthesis Characterization and Photocatalytic Studies of Cobalt Ferrite-Silica-Titania Nanocomposites. *Nanomaterials*, 4(2), 331-343.
- Gunasekaran, S., Natarajan, R., & Kala, A. (2007). FTIR spectra and mechanical strength analysis of some selected rubber derivatives. *Spectrochimica Acta Part A: Molecular and Biomolecular Spectroscopy*, 68(2), 323-330.
- Gyergyek, S., Makovec, D., & Drofenik, M. (2011). Colloidal stability of oleic-and ricinoleic-acid-coated magnetic nanoparticles in organic solvents. *Journal of colloid and interface science*, 354(2), 498-505.
- Harris, L. A. (2002). *Polymer stabilized magnetite nanoparticles and poly (propylene oxide) modified styrene-dimethacrylate networks*. Virginia Polytechnic Institute and State University.
- Hee Kim, E., Sook Lee, H., Kook Kwak, B., & Kim, B.-K. (2005). Synthesis of ferrofluid with magnetic nanoparticles by sonochemical method for MRI contrast agent. *Journal of Magnetism and Magnetic Materials*, 289, 328-330.
- Hwang, W.-G., Wei, K.-H., & Wu, C.-M. (2004). Preparation and mechanical properties of nitrile butadiene rubber/silicate nanocomposites. *Polymer*, 45(16), 5729-5734.
- Hyeon, T., Lee, S. S., Park, J., Chung, Y., & Na, H. B. (2001). Synthesis of highly crystalline and monodisperse maghemite nanocrystallites without a size-selection process. *Journal of the American Chemical Society*, 123(51), 12798-12801.
- Ibarra-Sánchez, J. J., Fuentes-Ramírez, R., Roca, A. G., del Puerto Morales, M., & Cabrera-Lara, L. I. (2013). Key Parameters for Scaling up the Synthesis of Magnetite Nanoparticles in Organic Media: Stirring Rate and Growth Kinetic. *Industrial & Engineering Chemistry Research*, 52(50), 17841-17847.



- Ibarra, L., Marcos-Fernandez, A., & Alzorriz, M. (2002). Mechanistic approach to the curing of carboxylated nitrile rubber (XNBR) by zinc peroxide/zinc oxide. *Polymer*, 43(5), 1649-1655.
- Iwasaki, T., Mizutani, N., Watano, S., Yanagida, T., & Kawai, T. (2010). Size control of magnetite nanoparticles by organic solvent-free chemical coprecipitation at room temperature. *Journal of Experimental Nanoscience*, 5(3), 251-262.
- Jana, N. R., Chen, Y., & Peng, X. (2004). Size-and shape-controlled magnetic (Cr, Mn, Fe, Co, Ni) oxide nanocrystals via a simple and general approach. *Chemistry of materials*, 16(20), 3931-3935.
- Jha, D. K., Shameem, M., Patel, A. B., Kostka, A., Schneider, P., Erbe, A., & Deb, P. (2013). Simple synthesis of superparamagnetic magnetite nanoparticles as highly efficient contrast agent. *Materials Letters*, 95, 186-189.
- Jiang, F., Wang, C. M., Fu, Y., & Liu, R. (2010). Synthesis of iron oxide nanocubes via microwave-assisted solvothermal method. *Journal of Alloys and Compounds*, 503(2), L31-L33.
- Kalkan, N. A., Aksoy, S., Aksoy, E. A., & Hasirci, N. (2012). Preparation of chitosan - coated magnetite nanoparticles and application for immobilization of laccase. *Journal of Applied Polymer Science*, 123(2), 707-716.
- Kang, S., Hong, S. I., Choe, C. R., Park, M., Rim, S., & Kim, J. (2001). Preparation and characterization of epoxy composites filled with functionalized nanosilica particles obtained via sol-gel process. *Polymer*, 42(3), 879-887.
- Karaagac, O., Kockar, H., & Tanrisever, T. (2011). Properties of Iron Oxide Nanoparticles Synthesized at Different Temperatures. *Journal of superconductivity and novel magnetism*, 24(1-2), 675-678.
- Kazemzadeh, H., Ataie, A., & Rashchi, F. (2012). *Synthesis of Magnetite Nano-Particles by Reverse Co-Precipitation*. Paper presented at the International Journal of Modern Physics: Conference Series.
- Kechrakos, D., & Trohidou, K. (1998). Magnetic properties of dipolar interacting single-domain particles. *Physical Review B*, 58(18), 12169.
- Khalafalla, S., & Reimers, G. (1980). Preparation of dilution-stable aqueous magnetic fluids. *Magnetics, IEEE Transactions on*, 16(2), 178-183.

- Khan, A. A., & Khalid, M. (2010). Synthesis of nano - sized ZnO and polyaniline - zinc oxide composite: Characterization, stability in terms of DC electrical conductivity retention and application in ammonia vapor detection. *Journal of applied polymer science*, 117(3), 1601-1607.
- Kim, D., Zhang, Y., Voit, W., Rao, K., & Muhammed, M. (2001). Synthesis and characterization of surfactant-coated superparamagnetic monodispersed iron oxide nanoparticles. *Journal of Magnetism and Magnetic Materials*, 225(1), 30-36.
- Kittel, C., & McEuen, P. (1976). *Introduction to solid state physics* (Vol. 8): Wiley New York.
- Kong, I., Hj Ahmad, S., Hj Abdullah, M., Hui, D., Nazlim Yusoff, A., & Puryanti, D. (2010). Magnetic and microwave absorbing properties of magnetite–thermoplastic natural rubber nanocomposites. *Journal of Magnetism and magnetic Materials*, 322(21), 3401-3409.
- Kroenke, W. J. (1969). PROCESSING AIDS IN PREPARATION OF NBR FLEXIBLE MAGNETS: Google Patents.
- Laurent, S., Forge, D., Port, M., Roch, A., Robic, C., Vander Elst, L., & Muller, R. N. (2008). Magnetic iron oxide nanoparticles: synthesis, stabilization, vectorization, physicochemical characterizations, and biological applications. *Chemical reviews*, 108(6), 2064-2110.
- Laurenzi, M. A. (2008). *Transformation kinetics & magnetism of magnetite nanoparticles*: ProQuest.
- Lee, J., Isobe, T., & Senna, M. (1996). Preparation of Ultrafine  $\text{Fe}_3\text{O}_4$  Particles by Precipitation in the Presence of PVA at High pH. *Journal of Colloid and Interface Science*, 177(2), 490-494.
- Li, Y.-S., Church, J. S., & Woodhead, A. L. (2012). Infrared and Raman spectroscopic studies on iron oxide magnetic nano-particles and their surface modifications. *Journal of Magnetism and Magnetic Materials*, 324(8), 1543-1550.
- Li, Y., Pan, G., Wang, Q., Jiao, H., Hu, K., & Wang, T. (2013). Preparation and Properties of Organically Modified Montmorillonite/Nitrile Rubber Nanocomposites. *Journal of Macromolecular Science, Part B*, 52(4), 561-573.
- Liang, J., Li, H., Yan, J., & Hou, W. G. (2014). Demulsification of oleic acid-coated magnetite nanoparticles for cyclohexane-in-water nanoemulsions. *Energy & Fuels*.

- Lien, Y.-H., & Wu, T.-M. (2008). Preparation and characterization of thermosensitive polymers grafted onto silica-coated iron oxide nanoparticles. *Journal of colloid and interface science*, 326(2), 517-521.
- Lipinski, T. M., & Tang, C. K. (2011). Thin, smooth nitrile rubber gloves: Google Patents.
- Liu, Z., Wang, X., Yao, K., Du, G., Lu, Q., Ding, Z., . . . Tian, D. (2004). Synthesis of magnetite nanoparticles in W/O microemulsion. *Journal of materials science*, 39(7), 2633-2636.
- Lopez-Quintela, M. A. (2003). Synthesis of nanomaterials in microemulsions: formation mechanisms and growth control. *Current opinion in Colloid & interface science*, 8(2), 137-144.
- Lowrie, W. (1990). Identification of ferromagnetic minerals in a rock by coercivity and unblocking temperature properties. *Geophysical Research Letters*, 17(2), 159-162.
- Lucas, D. M., Loo, L. Y., Lai, H. M., Barclay, J., & Wong, S. W. (2009). Magnetically detectable latex articles: Google Patents.
- Lv, L., Wan, S., Pan, B., Zhang, W., & An, D. (2011). Deep purification method for removing trace thallium in water by using polymer-based nanosized manganese oxide: Google Patents.
- Mahmed, N. (2013). Development of Multifunctional Magnetic Core Nanoparticles.
- Mahmoudi, M., Simchi, A., Imani, M., Milani, A. S., & Stroeve, P. (2008). Optimal Design and Characterization of Superparamagnetic Iron Oxide Nanoparticles Coated with Polyvinyl Alcohol for Targeted Delivery and Imaging†. *The Journal of Physical Chemistry B*, 112(46), 14470-14481.
- Makled, M., Matsui, T., Tsuda, H., Mabuchi, H., El-Mansy, M., & Morii, K. (2005). Magnetic and dynamic mechanical properties of barium ferrite–natural rubber composites. *Journal of Materials Processing Technology*, 160(2), 229-233.
- Malaysian Rubber Board. (2014). Natural Rubber Statistics Retrieved June 12, 2015, from <http://www.lgm.gov.my/nrstat/nrstats.pdf>
- Maldonado, K. L., de la Presa, P., de la Rubia, M., Crespo, P., de Frutos, J., Hernando, A., . . . Galindo, J. E. (2014). Effects of grain boundary width and crystallite size on conductivity and magnetic properties of magnetite nanoparticles. *Journal of nanoparticle research*, 16(7), 1-12.

- Mandel, K., Hutter, F., Gellermann, C., & SEXTL, G. (2011). Synthesis and stabilisation of superparamagnetic iron oxide nanoparticle dispersions. *Colloids and Surfaces A: Physicochemical and Engineering Aspects*, 390(1), 173-178.
- Mascolo, M. C., Pei, Y., & Ring, T. A. (2013). Room temperature co-precipitation synthesis of magnetite nanoparticles in a large pH window with different bases. *Materials*, 6(12), 5549-5567.
- Men, H.-F., Liu, H.-Q., Zhang, Z.-L., Huang, J., Zhang, J., Zhai, Y.-Y., & Li, L. (2012). Synthesis, properties and application research of atrazine Fe<sub>3</sub>O<sub>4</sub>@ SiO<sub>2</sub> magnetic molecularly imprinted polymer. *Environmental Science and Pollution Research*, 19(6), 2271-2280.
- Mizukoshi, Y., Shuto, T., Masahashi, N., & Tanabe, S. (2009). Preparation of superparamagnetic magnetite nanoparticles by reverse precipitation method: contribution of sonochemically generated oxidants. *Ultrasonics sonochemistry*, 16(4), 525-531.
- Mizutani, N., Iwasaki, T., Watano, S., Yanagida, T., Tanaka, H., & Kawai, T. (2008). Effect of ferrous/ferric ions molar ratio on reaction mechanism for hydrothermal synthesis of magnetite nanoparticles. *Bulletin of Materials Science*, 31(5), 713-717.
- Mo, T.-C., Wang, H.-W., Chen, S.-Y., & Yeh, Y.-C. (2008). Synthesis and dielectric properties of polyaniline/titanium dioxide nanocomposites. *Ceramics International*, 34(7), 1767-1771.
- Mohapatra, M., & Anand, S. (2010). Synthesis and applications of nano-structured iron oxides/hydroxides—a review. *International Journal of Engineering, Science and Technology*, 2(8).
- Moharir, R. G., Gogate, P. R., & Rathod, V. K. (2012). Process intensification of synthesis of magnetite using spinning disc reactor. *The Canadian Journal of Chemical Engineering*, 90(4), 996-1005.
- Musa, M., Arief, Y., Abdul-Malek, Z., Ahmad, M., & Jamil, A. (2013). *Influence of nano-titanium dioxide (TiO<sub>2</sub>) on electrical tree characteristics in silicone rubber based nanocomposite*. Paper presented at the Electrical Insulation and Dielectric Phenomena (CEIDP), 2013 IEEE Conference on.
- Palza, H., Vergara, R., & Zapata, P. (2011). Composites of polypropylene melt blended with synthesized silica nanoparticles. *Composites Science and Technology*, 71(4), 535-540.
- Park, J., An, K., Hwang, Y., Park, J.-G., Noh, H.-J., Kim, J.-Y., . . . Hyeon, T. (2004). Ultra-large-scale syntheses of monodisperse nanocrystals. *Nature materials*, 3(12), 891-895.

- Petcharoen, K., & Sirivat, A. (2012). Synthesis and characterization of magnetite nanoparticles via the chemical co-precipitation method. *Materials Science and Engineering: B*, 177(5), 421-427.
- Peternele, W. S., Monge Fuentes, V., Fascineli, M. L., Rodrigues da Silva, J., Silva, R. C., Lucci, C. M., & Bentes de Azevedo, R. (2014). Experimental Investigation of the Coprecipitation Method: An Approach to Obtain Magnetite and Maghemite Nanoparticles with Improved Properties. *Journal of Nanomaterials*, 2014.
- Powell, B. A., Dai, Z., Zavarin, M., Zhao, P., & Kersting, A. B. (2011). Stabilization of plutonium nano-colloids by epitaxial distortion on mineral surfaces. *Environmental science & technology*, 45(7), 2698-2703.
- Prasertsri, S., & Rattanasom, N. (2011). Mechanical and damping properties of silica/natural rubber composites prepared from latex system. *Polymer Testing*, 30(5), 515-526.
- Rafiee, E., Ataei, A., Nadri, S., Joshaghani, M., & Eavani, S. (2014). Combination of palladium and oleic acid coated-magnetite particles: Characterization and using in Heck coupling reaction with magnetic recyclability. *Inorganica Chimica Acta*, 409, 302-309.
- Ramajo, L., Cristóbal, A., Botta, P., Porto López, J., Reboredo, M., & Castro, M. (2009). Dielectric and magnetic response of Fe<sub>3</sub>O<sub>4</sub>/epoxy composites. *Composites Part A: Applied Science and Manufacturing*, 40(4), 388-393.
- Ramimoghadam, D., Bagheri, S., & Hamid, S. B. A. (2015). Stable Monodisperse Nanomagnetic Colloidal Suspensions: An overview. *Colloids and Surfaces B: Biointerfaces*.
- Razzaq, M. Y., Anhalt, M., Frommann, L., & Weidenfeller, B. (2007). Thermal, electrical and magnetic studies of magnetite filled polyurethane shape memory polymers. *Materials Science and Engineering: A*, 444(1), 227-235.
- Reinholds, I., Kalkis, V., & Maksimovs, R. D. (2012). The effect of ionizing radiation and magnetic field on deformation properties of high density polyethylene/acrylonitrile-butadiene composites. *Journal of Chemistry and Chemical Engineering*, 6(3), 242-249.
- Rong, Y., Chen, H.-Z., Wu, G., & Wang, M. (2005). Preparation and characterization of titanium dioxide nanoparticle/polystyrene composites via radical polymerization. *Materials Chemistry and Physics*, 91(2), 370-374.
- Ruiz, A., Salas, G., Calero, M., Hernandez, Y., Villanueva, A., Herranz, F., . . . Morales, M. (2013). Short-chain PEG molecules strongly bound to magnetic nanoparticle for MRI long circulating agents. *Acta biomaterialia*, 9(5), 6421-6430.

- Sagar, S., Iqbal, N., Maqsood, A., & Javaid, U. (2013). Thermogravimetric, differential scanning calorimetric and experimental thermal transport study of MWCNT/NBR nanocomposites. *Journal of thermal analysis and calorimetry*, 114(1), 161-167.
- Sahoo, Y., Pizem, H., Fried, T., Golodnitsky, D., Burstein, L., Sukenik, C. N., & Markovich, G. (2001). Alkyl phosphonate/phosphate coating on magnetite nanoparticles: a comparison with fatty acids. *Langmuir*, 17(25), 7907-7911.
- Salunkhe, A., Khot, V., Thorat, N., Phadatare, M., Sathish, C., Dhawale, D., & Pawar, S. (2013). Polyvinyl alcohol functionalized cobalt ferrite nanoparticles for biomedical applications. *Applied surface science*, 264, 598-604.
- Sarkar, S., Guibal, E., Quignard, F., & SenGupta, A. (2012). Polymer-supported metals and metal oxide nanoparticles: synthesis, characterization, and applications. *Journal of Nanoparticle Research*, 14(2), 1-24.
- Sciancalepore, C., Bondioli, F., Manfredini, T., & Gualtieri, A. (2015). Quantitative phase analysis and microstructure characterization of magnetite nanocrystals obtained by microwave assisted non-hydrolytic sol-gel synthesis. *Materials Characterization*, 100, 88-97.
- Serna, C., Bødker, F., Mørup, S., Morales, M., Sandiumenge, F., & Veintemillas-Verdaguer, S. (2001). Spin frustration in maghemite nanoparticles. *Solid state communications*, 118(9), 437-440.
- Shete, P., Patil, R., Tiwale, B., & Pawar, S. (2015). Water dispersible oleic acid-coated Fe<sub>3</sub>O<sub>4</sub> nanoparticles for biomedical applications. *Journal of Magnetism and Magnetic Materials*, 377, 406-410.
- Slavov, L., Abrashev, M., Merodiiska, T., Gelev, C., Vandenberghe, R., Markova-Deneva, I., & Nedkov, I. (2010). Raman spectroscopy investigation of magnetite nanoparticles in ferrofluids. *Journal of Magnetism and Magnetic Materials*, 322(14), 1904-1911.
- Sreeja, V., & Joy, P. (2011). Effect of inter-particle interactions on the magnetic properties of magnetite nanoparticles after coating with dextran. *International Journal of Nanotechnology*, 8(10), 907-915.
- Strangway, D., Honea, R., McMahon, B., & Larson, E. (1968). The magnetic properties of naturally occurring goethite. *Geophysical Journal International*, 15(4), 345-359.
- Sun, S., & Zeng, H. (2002). Size-controlled synthesis of magnetite nanoparticles. *Journal of the American Chemical Society*, 124(28), 8204-8205.

- Sun, Y.-P., Li, X.-q., Cao, J., Zhang, W.-x., & Wang, H. P. (2006). Characterization of zero-valent iron nanoparticles. *Advances in colloid and interface science*, 120(1), 47-56.
- Sun, Y.-P., Li, X.-Q., Zhang, W.-X., & Wang, H. P. (2007). A method for the preparation of stable dispersion of zero-valent iron nanoparticles. *Colloids and Surfaces A: Physicochemical and Engineering Aspects*, 308(1), 60-66.
- Suzuki, N., Ito, M., & Ono, S. (2005). Effects of rubber/filler interactions on the structural development and mechanical properties of NBR/silica composites. *Journal of applied polymer science*, 95(1), 74-81.
- Taghvaei, A., Ebrahimi, A., Ghaffari, M., & Janghorban, K. (2010). RETRACTED: Magnetic properties of iron-based soft magnetic composites with MgO coating obtained by sol-gel method. *Journal of Magnetism and Magnetic Materials*, 322(7), 808-813.
- Tajabadi, M., & Khosroshahi, M. (2012). Effect of alkaline media concentration and modification of temperature on magnetite synthesis method using  $\text{FeSO}_4/\text{NH}_4\text{OH}$ . *Int J Chem Eng Appl*, 3, 206-210.
- Tan, W., & Abu Bakar, M. (2013). Synthesis, characterization and impedance spectroscopy study of magnetite/epoxidized natural rubber nanocomposites. *Journal of Alloys and Compounds*, 561, 40-47.
- Tartaj, P., Morales, M. P., Veintemillas-Verdaguer, S., Gonzalez-Carreño, T., & Serna, C. J. (2006). Chapter 5 Synthesis, Properties and Biomedical Applications of Magnetic Nanoparticles. *Handbook of magnetic materials*, 16, 403-482.
- Teja, A. S., & Koh, P.-Y. (2009). Synthesis, properties, and applications of magnetic iron oxide nanoparticles. *Progress in Crystal Growth and Characterization of Materials*, 55(1), 22-45.
- Teng, X., & Yang, H. (2004). Effects of surfactants and synthetic conditions on the sizes and self-assembly of monodisperse iron oxide nanoparticles. *Journal of Materials Chemistry*, 14(4), 774-779.
- Thévenot, J., Oliveira, H., Sandre, O., & Lecommandoux, S. (2013). Magnetic responsive polymer composite materials. *Chemical Society Reviews*, 42(17), 7099-7116.
- Ünak, P. (2008). Imaging and therapy with radionuclide labeled magnetic nanoparticles. *Brazilian Archives of Biology and Technology*, 51(spe), 31-37.

- Utkan, G. G., Sayar, F., Batat, P., Ide, S., Kriechbaum, M., & Pişkin, E. (2011). Synthesis and characterization of nanomagnetite particles and their polymer coated forms. *Journal of colloid and interface science*, 353(2), 372-379.
- Valenzuela, R., Fuentes, M. C., Parra, C., Baeza, J., Duran, N., Sharma, S., . . . Freer, J. (2009). Influence of stirring velocity on the synthesis of magnetite nanoparticles ( $\text{Fe}_3\text{O}_4$ ) by the co-precipitation method. *Journal of Alloys and Compounds*, 488(1), 227-231.
- Vega-Baudrit, J., Navarro-Banon, V., Vázquez, P., & Martín-Martínez, J. M. (2006). Addition of nanosilicas with different silanol content to thermoplastic polyurethane adhesives. *International journal of adhesion and adhesives*, 26(5), 378-387.
- Vidal-Vidal, J., Rivas, J., & López-Quintela, M. (2006). Synthesis of monodisperse maghemite nanoparticles by the microemulsion method. *Colloids and Surfaces A: Physicochemical and Engineering Aspects*, 288(1), 44-51.
- Wang, B., Wei, Q., & Qu, S. (2013). Synthesis and characterization of uniform and crystalline magnetite nanoparticles via oxidation-precipitation and modified co-precipitation methods. *Int. J. Electrochem. Sci*, 8, 3786-3793.
- Wang, Y., Li, B., Zhou, Y., & Jia, D. (2009). In situ mineralization of magnetite nanoparticles in chitosan hydrogel. *Nanoscale research letters*, 4(9), 1041-1046.
- Wang, Z., Lu, Y., Liu, J., Dang, Z., Zhang, L., & Wang, W. (2011). Preparation of nano - zinc oxide/EPDM composites with both good thermal conductivity and mechanical properties. *Journal of Applied Polymer Science*, 119(2), 1144-1155.
- Woo, K., Hong, J., Choi, S., Lee, H.-W., Ahn, J.-P., Kim, C. S., & Lee, S. W. (2004). Easy synthesis and magnetic properties of iron oxide nanoparticles. *Chemistry of Materials*, 16(14), 2814-2818.
- Xu, C., & Teja, A. S. (2008). Continuous hydrothermal synthesis of iron oxide and PVA-protected iron oxide nanoparticles. *The Journal of Supercritical Fluids*, 44(1), 85-91.
- Yan, X., & Xu, G. (2009). Effect of sintering atmosphere on the electrical and optical properties of  $(\text{ZnO})_{1-x}(\text{MnO})_x$  NTCR ceramics. *Physica B: Condensed Matter*, 404(16), 2377-2381.
- Yang, T.-I., Brown, R. N., Kempel, L. C., & Kofinas, P. (2008). Magneto-dielectric properties of polymer- $\text{Fe}_3\text{O}_4$  nanocomposites. *Journal of Magnetism and Magnetic Materials*, 320(21), 2714-2720.



- Yu, W.-G., Zhang, T.-L., Qiao, X.-J., Zhang, J.-G., & Yang, L. (2007). Effects of synthetical conditions on octahedral magnetite nanoparticles. *Materials Science and Engineering: B*, 136(2), 101-105.
- Yuan, X., Peng, Z., Zhang, Y., & Zhang, Y. (2000). In situ preparation of zinc salts of unsaturated carboxylic acids to reinforce NBR. *Journal of Applied Polymer Science*, 77(12), 2740-2748.
- Zaborski, M., & Masłowski, M. (2011). Magnetorheological elastomer composites *Trends in Colloid and Interface Science XXIV* (pp. 21-25): Springer.
- Zgheib, N., Putaux, J.-L., Thill, A., D'Agosto, F., Lansalot, M., & Bourgeat-Lami, E. (2012). Stabilization of miniemulsion droplets by cerium oxide nanoparticles: a step toward the elaboration of armored composite latexes. *Langmuir*, 28(14), 6163-6174.
- Zhang, W., Jia, S., Wu, Q., Ran, J., Wu, S., & Liu, Y. (2011). Convenient synthesis of anisotropic Fe<sub>3</sub>O<sub>4</sub> nanorods by reverse co-precipitation method with magnetic field-assisted. *Materials Letters*, 65(12), 1973-1975.
- Zhang, X., Niu, H., Pan, Y., Shi, Y., & Cai, Y. (2010). Chitosan-coated octadecyl-functionalized magnetite nanoparticles: preparation and application in extraction of trace pollutants from environmental water samples. *Analytical chemistry*, 82(6), 2363-2371.
- Zhao, G., Shi, L., Feng, X., Yu, W., Zhang, D., & Fu, J. (2012). Palygorskite-cerium oxide filled rubber nanocomposites. *Applied Clay Science*, 67, 44-49.
- Zhi, J., Wang, Y., Lu, Y., Ma, J., & Luo, G. (2006). In situ preparation of magnetic chitosan/Fe<sub>3</sub>O<sub>4</sub> composite nanoparticles in tiny pools of water-in-oil microemulsion. *Reactive and Functional Polymers*, 66(12), 1552-1558.

## List of publications and papers presented

### 7.1 Journal publication

#### 7.1.1 Malaysian Journal of Chemistry

##### Properties of Iron Oxide Nanoparticles (IONs)

Hun Tiar Ong, Nurhidayatullaili Muhd Julkapli\*, O. Boondamnoen, Mun Foong Tai and Sharifah Bee Abd Hamid

Nanotechnology & Catalysis Research Centre (NANOCAT),  
3rd Floor, Block A, Institute of Postgraduate Studies (IPS),  
University of Malaya, 50603 Kuala Lumpur,  
MALAYSIA.

\* Corresponding author: [nurhidayatullaili@um.edu.my](mailto:nurhidayatullaili@um.edu.my)

##### Abstract

Due to hygiene concern in food, pharmaceutical processing and healthcare industries, gloves are required to wear. In fact, these gloves might tear off and contaminate the food and pharmaceutical or healthcare products during manufacturing and packaging process. The white or light flesh-colored gloves is not easy to detect by naked eyes, subsequently they lead to difficulty in removal before shipping. In this paper, iron oxide nanoparticles are selected as additive for nitrile butadiene rubber (NBR) in order to improve the detectability of gloves by mean of its magnetic properties. Iron oxide nanoparticles (IONs) are synthesized via precipitation method with monosalt iron (II) sulfate heptahydrate and ammonium hydroxide as precursors at 60 °C. The properties of IONs are investigated by Zetasizer, X-ray Diffractometry (XRD), Transmission Electron Microscope (TEM), Raman Spectroscopy and Vibrating Sample Magnetometer (VSM). Based on Zetasizer analysis, iron oxides are found in average hydrodynamic size 87.8 nm. By using Scherrer equation, XRD shows an average of 25.95 nm crystallite size. Semispherical shape with 15.4 nm of IONs was observed by TEM. Magnetite and maghemite phase are found in range of 670 cm<sup>-1</sup> and 700 cm<sup>-1</sup> respectively by through Raman spectroscopy. Finally, IONs with 70.1 emu/g of magnetization saturation was able to form NBR/IONs composite with 3.8 emu/g magnetization saturation.

**Keywords:** Iron oxide nanoparticles; precipitation; magnetic properties; magnetization

#### 7.1.2 Journal of Magnetism and Magnetic Materials

##### Phase Control of Iron Oxide Nanoparticles (IONP) via Aging during Precipitation Step

Hun Tiar Ong, Sharifah Bee Abd Hamid\*, Nurhidayatullaili Muhd Julkapli, and Mun Foong Tai.

Nanotechnology & Catalysis Research Centre (NANOCAT),  
3rd Floor, Block A, Institute of Postgraduate Studies (IPS),  
University of Malaya, 50603 Kuala Lumpur,

MALAYSIA.

\* Corresponding author: sharifahbee@um.edu.my

#### **Abstract**

It is crucial to develop and optimize method to obtain pure magnetite IONP as it may consist of different phases depending on synthesis method. Therefore, a facile precipitation method to synthesize high purity magnetite phase with superior magnetic properties at nano sized with good polydispersity of iron oxide nanoparticle (IONP) was addressed. Iron (II) sulphate heptahydrate and ammonium hydroxide were selected as precursors to synthesize IONP at 60 °C at 1, 1.25, 1.5, 1.75 and 2 hours aging time. The physical and magnetic properties of IONP were investigated by X-ray Diffractometry (XRD), Raman Spectroscopy, Fourier Transform Infrared spectroscopy (FTIR), Zetasizer, Transmission Electron Microscope (TEM) and Vibrating Sample Magnetometer (VSM). From the XRD result, IONP synthesized at 1.5 hrs aging time consists of high percentage of magnetite phase compared to IONP synthesized at 1, 1.25, 1.75 and 2 hrs aging time. This result is supported by Raman and FTIR spectra. Besides, IONP synthesized at 1.5 hrs aging time has the smallest particle size (22.619 nm) with narrow particle size distribution. Lastly, it has the highest magnetization saturation attributed to high percentage (82 %) of magnetite phase. Throughout the results, it affirmed that IONP synthesized at 1.5 hrs aging time has superior physical and magnetic properties and it is favoured in many applications especially in medical diagnosis and therapy.

**Keywords:** Iron oxide nanoparticles (IONP); precipitation; aging time; magnetization

### **7.1.3 Journal of Composite Science and Technology**

#### **Effect of Magnetic and Thermal Properties of Iron Oxide Nanoparticles (IONs) in Nitrile Butadiene Rubber (NBR) latex**

Hun Tiar Ong, Nurhidayatullaili Muhd Julkapli, Sharifah Bee Abd Hamid\*, O. Boondamnoen and Mun Foong Tai

Nanotechnology & Catalysis Research Centre (NANOCAT),  
3rd Floor, Block A, Institute of Postgraduate Studies (IPS),  
University of Malaya, 50603 Kuala Lumpur,  
MALAYSIA.

\* Corresponding author: sharifahbee@um.edu.my

#### **Abstract**

Nitrile butadiene rubber (NBR) gloves are one of the most important personal protective equipment but they are possible to tear off and contaminate food or pharmaceutical and healthcare products during manufacturing and packaging process. High tendency of torn glove remaining in food or products due to white or light flesh-coloured glove is not easy to be detected by naked eyes. In this paper, Iron oxide nanoparticles (IONs) selected as additive for NBR to improve its detectability by mean of magnetic properties. IONs synthesized via precipitation method and compounded with NBR latex before casting on petri dish. The properties of IONs were investigated by X-ray Diffractometry (XRD), Transmission Electron Microscope (TEM), Raman Spectroscopy and Vibrating

Sample Magnetometer (VSM). Meanwhile NBR/IONs composites were studied by Thermogravimetry Analysis (TGA), Differential Scanning Calorimetry (DSC) and Vibrating Sample Magnetometer (VSM). It observed that, synthesized IONs shows of 25.28 nm crystallite with 25.86 nm semispherical shape.. Meanwhile, Magnetite and maghemite phase are found in range of  $670\text{ cm}^{-1}$  and  $700\text{ cm}^{-1}$  respectively, which it contributes magnetization saturation of 73.96 emu/g at 10000 G by VSM. Thermal stability and magnetic properties were increased with incorporating IONs into NBR latex up to 20 phr. NBR/IONs 5 phr has the optimum thermal stability, lowest glass transition temperature ( $-14.83\text{ }^{\circ}\text{C}$ ) and acceptable range of magnetization saturation (3.83 emu/g at 10000 G) to form magnetic detectability NBR gloves.

**Keywords:** A. Nano composites; A. Polymer-matrix composites; B. Thermal properties; B. Magnetic properties; D. Thermogravimetric analysis (TGA)

## 7.2 Paper Presented

### 7.2.1 NANO-SciTech 2014 & IC-NET 2014

Location : UiTM Shah Alam  
Date : 28 Feb to 3 March 2014

#### **Properties Comparison Between Magnetite Iron Oxide Nanoparticles Synthesis via Reverse Co-Precipitation Method and Normal Co-precipitation Method**

Hun Tiar Ong, Nurhidayatullaili Muhd Julkapli\*, O. Boondamnoen, Mun Foong Tai and Sharifah Bee Abd Hamid

Nanotechnology & Catalysis Research Centre (NANOCAT),  
3rd Floor, Block A, Institute of Postgraduate Studies (IPS),  
University of Malaya, 50603 Kuala Lumpur,  
MALAYSIA.

\* Corresponding author: nurhidayatullaili@um.edu.my

#### **Abstract**

Nanoparticles had become well-known and attractive in terms of their sizes due to fast development in recent years. Several methods such as hydrothermal reaction, high thermal decomposition and microemulsion were carried out by researchers to synthesis nanoparticle size magnetite iron oxide as small as possible. However, these methods are complicated and high cost. Thus, co-precipitation is selected in this paper where reverse co-precipitation and normal co-precipitation had been carried out to determine the properties of nanoparticle iron oxides. Herein, we prepare electrolyte which consists of iron(II) chloride tetrahydrate and iron(III) chloride hexahydrate in deionized water with 3.0 M of ammonium hydroxide. For normal co-precipitation, ammonium hydroxide is titrated into the iron salt solution and vice versa for reverse co-precipitation. In the present study, the effect of different synthesis methods on the morphology, particle size, crystallinity and surface charge of the iron oxide particles were investigated in detail. Based on the Malvern Zetasizer analysis, the iron oxide particles with *variable size from* ~ 59 nm to ~ 67 nm could be achieved for normal co-precipitation whilst iron oxides

with variable sizes from ~ 21 nm to ~ 52 nm could be achieved for reverse co-precipitation. The crystal diameter for reverse co-precipitation sample is smaller than normal co-precipitation sample. The magnetite phase can be identified through Fourier transform infrared spectroscopy and Raman spectroscopy. Furthermore, FESEM micrographs further explain that our synthesized iron oxide were in nanoparticle scale with spherical shape. It was found that reverse co-precipitation able to synthesis smaller nanoparticle magnetite iron oxide.

**Keywords:** magnetite; nanoparticle iron oxides; normal co-precipitation; reverse co-precipitation; particle size; PEG 600

### 7.2.2 18<sup>th</sup> MICC 2014

Location : PWTC, KL

Date : 3 to 5 Nov 2014

#### Properties of Iron Oxide Nanoparticles (IONs)

Hun Tiar Ong, Nurhidayatullaili Muhd Julkapli\*, O. Boondamnoen, Mun Foong Tai and Sharifah Bee Abd Hamid

Nanotechnology & Catalysis Research Centre (NANOCAT),  
3rd Floor, Block A, Institute of Postgraduate Studies (IPS),  
University of Malaya, 50603 Kuala Lumpur,  
MALAYSIA.

\* Corresponding author: [nurhidayatullaili@um.edu.my](mailto:nurhidayatullaili@um.edu.my)

#### Abstract

Due to hygiene concern in food, pharmaceutical processing and healthcare industries, gloves are required to wear. In fact, these gloves might tear off and contaminate the food and pharmaceutical or healthcare products during manufacturing and packaging process. The white or light flesh-colored gloves is not easy to detect by naked eyes, subsequently they lead to difficulty in removal before shipping. In this paper, iron oxide nanoparticles are selected as additive for nitrile butadiene rubber (NBR) in order to improve the detectability of gloves by mean of its magnetic properties. Iron oxide nanoparticles (IONs) are synthesized via precipitation method with monosalt iron (II) sulfate heptahydrate and ammonium hydroxide as precursors at 60 °C. The properties of IONs are investigated by Zetasizer, X-ray Diffractometry (XRD), Transmission Electron Microscope (TEM), Raman Spectroscopy and Vibrating Sample Magnetometer (VSM). Based on Zetasizer analysis, iron oxides are found in average hydrodynamic size 87.8 nm. By using Scherrer equation, XRD shows an average of 25.95 nm crystallite size. Semispherical shape with 15.4 nm of IONs was observed by TEM. Magnetite and maghemite phase are found in range of 670 cm<sup>-1</sup> and 700 cm<sup>-1</sup> respectively by through Raman spectroscopy. Finally, IONs with 70.1 emu/g of magnetization saturation was able to form NBR/IONs composite with 3.8 emu/g magnetization saturation.

**Keywords:** Iron oxide nanoparticles; precipitation; magnetic properties; magnetization